Technical Design Report for the CBM

ADDENDUM
Transition Radiation Detector 2D (TRD-2D)

The CBM Collaboration

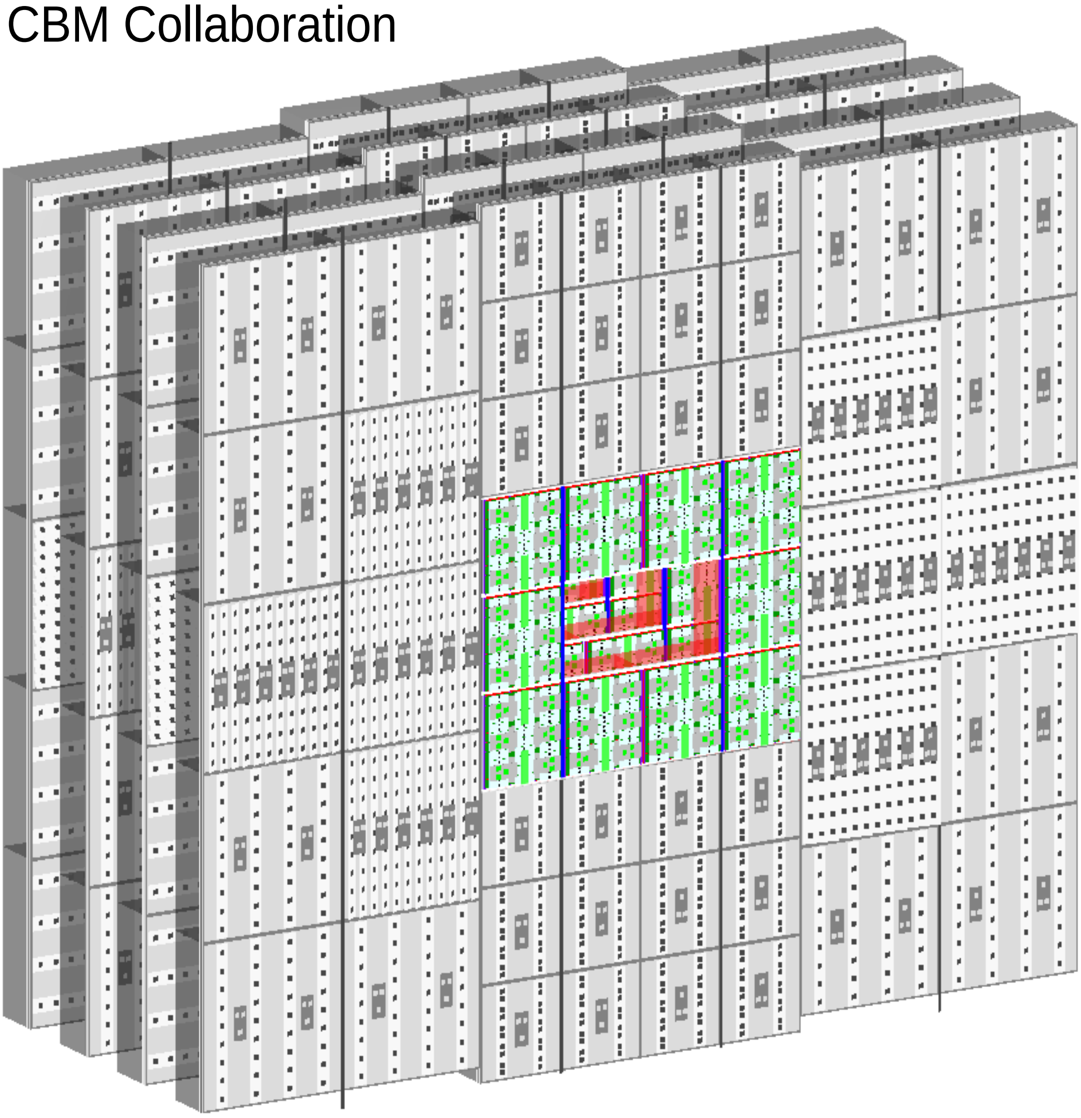

February 2021

Compressed Baryonic Matter Experiment

Addendum TRD TDR

An Enhanced Tracking Device For the Inner Region of the TRD wall

corresponding authors:
Alexandru Bercuci and Mihai Petrovici

V. Aprodu, D. Bartoş, G, Caragheorgheopol, V. Cătănescu,
M. Petriş, L. Prodan, A. Radu, L. Rădulescu, C. Şchiaua, M. Târzilă

for the CBM Collaboration

Submitted to the
CBM TRD Collaboration
February 28, 2021

CBM GIT revision v0

Executive summary

This documents describes an alternative design for the inner region of the Transition Radiation Detector (TRD) of the Compressed Baryonic Matter (CBM) experiment at FAIR. The new system, coined as the TRD Two Dimensional (TRD-2D), is optimized in terms of spatial discrimination for the areas of very high counting rates of 10^5 $particles/cm^2/s$. It adds to the baseline design, the possibility to reconstruct spatial position in two dimensions, thus enabling stand alone track reconstruction. This feature, coupled with a good coverage at small dispersion angles, enable us to extend reliable the measurement of p_T spectra towards low values thus rendering better estimates on physics of collective phenomena. The extension of $y - p_T$ space coverage for the electron sector is also achieved by stand alone track reconstruction and thus a better precision on mass resonances.

The main difference with respect to the TDR design is the replacement of the rectangular read-out inductive plane with read-out elements of a right triangular shape. This feature is coupled with a Front End Electronics (FEE) ASIC Fast Analog Signal Processor (FASP) which pairs such read-out elements to rectangles and parallelograms with the net outcome of bringing the resolution across pads int the hundreds of microns range. The improvement is beneficial for time and energy resolutions as well. A special care was devoted to the mechanical integration within the existing TRD frame. The aim of the mechanical design was to push heav supporting structures, main contributors to secondary production, to areas further away from the beam pipe.

In this addendum the design and performances of the TRD-2D are described in details. A special effort was to minimize the impact of the new design with respect to the general TRD system as already described in the TDR. The TRD-2D project will be realized exclusively by the Romanian institutes as part of the TRD collaboration. The detector system is foreseen to be constructed and installed into the CBM experiment for the Modularized Start Version (MSV) of FAIR.

Contents

1 Physics Motivation and Objectives

As it is well known, the region of the strogly interacting matter phase diagram predicted by QCD, which will be accessed using the CBM experiment at FAIR, is characterised by distinct features of many observables as a function of collision energy. Multi-differential studies of these trends require significantly larger statistics and better data quality relative to what was or is accessed in the former or present experiments, respectively.

1.1 Low p_T spectra exploration and rare probes *(M.Petrovici, A. Pop)*

One of the main processes in heavy ion collisions at energies higher than the Fermi energy, i.e. collective expansion of a compressed and hot baryonic fireball, was evidenced by the FOPI Collaboration at SIS-18 energies [1, 2]. These results were confirmed and extended at higher energies [3, 4, 5, 6]. At larger energies, at RHIC and LHC, it was evidenced that such a dynamics takes place even in a highly dense and hot deconfined fireball.

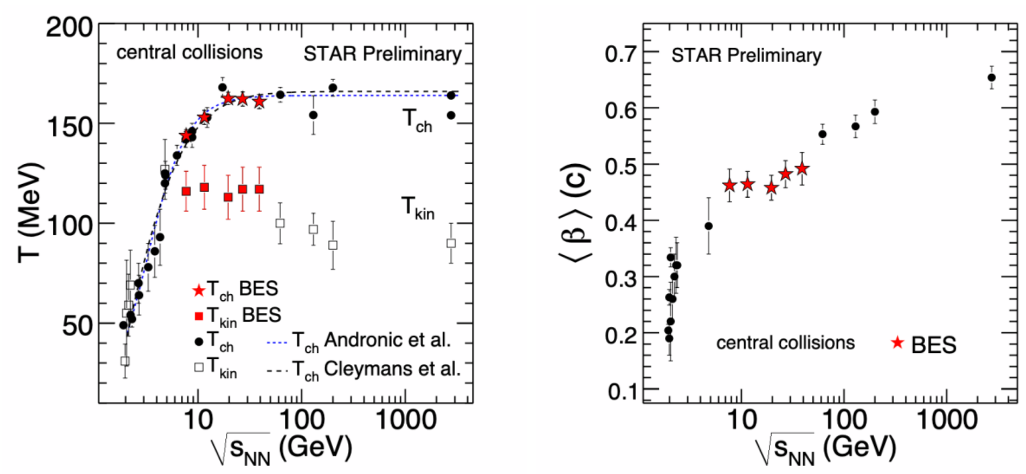

Figure 1.1.1: The chemical (T_{th}) and kinetic freeze-out temperature (T_{kin}) and the average transverse expansion velocity ($\langle\beta_T\rangle$) as a function of collision energy ([7] and references therein).

The compilations of these results in terms of the average value of the transverse expansion velocity ($\langle\beta_T\rangle$) and kinetic freeze-out temperature (T_{kin}^{fo}), obtained by fitting the transverse momentum spectra of different species using an expression inspired by hydrodynamical models (see Figure 1.1.1), evidences a clear change in the behaviour of $\langle\beta_T\rangle$ and T_{kin}^{fo} in the energy domain which will be covered by the CBM experiment at FAIR.

In the same energy range, another transition takes place, the azimuthal distribution of emitted particles is changing from a preferential out-of-plane emission of particles to an in-plane enhancement [8, 9] (Figure 1.1.2).

For a detailed understanding of the origin of these observations, the relative contribution of baryons, resonances or precursors of deconfined matter, a multi-differential analysis is mandatory. Previous experience has shown that the low p_T region of the transverse momentum distribution for π, K and p and their antiparticles plays a crucial role in obtaining precise information on the yield, average transverse momentum and fit parameters mentioned above.

In Figure 1.1.3 are presented results based on theoretical models, i.e. UrQMD [10] and JAM [11], in terms of the elliptic flow v_2 as a function of collision energy (E_{lab}) for Au-Au at $5.5fm < b < 7.5fm$ centrality and Z=1 particles. As can be observed, the collision energy at

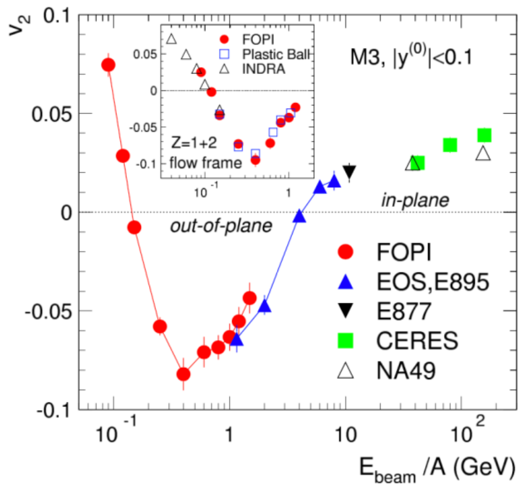

Figure 1.1.2: Excitation function of integral elliptic flow (v_2) for Z=1 particles compared with the experimental values obtained from all available fixed target experiments ([9] and references therein).

which the transition from out-of-plane to in-plane takes place is very sensitive to the EoS in the UrQMD model.

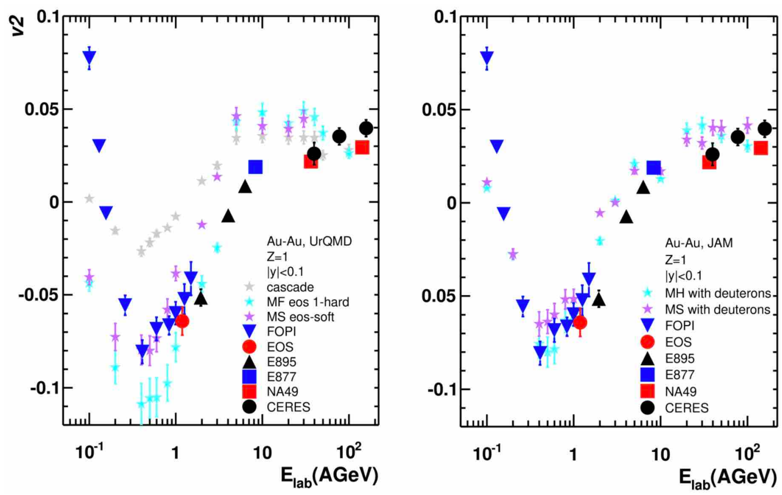

Figure 1.1.3: Elliptic flow v_2, for Z=1 particles as a function of collision energy, calculated using the UrQMD [10] (left) and JAM [11] (right) models for the Au-Au collision and comparison with experimental data.

In Figure 1.1.4 is presented a compilation of the average transverse expansion velocity, $\langle \beta_T \rangle$, as a function of the square root of the hadron multiplicity per unit of rapidity and unit of the colliding partners transverse overlapping area ($\sqrt{(dN/dy)/S_\perp}$) for all collision energies larger than $\sqrt{s_{NN}}$=7.7 GeV, measured up to now [12]. As can be observed, below $\sqrt{s_{NN}}$=39 GeV, antiparticles deviate from such a scaling, the estimated $\langle \beta_T \rangle$ being larger than the values corresponding to the particles. The study of these features below $\sqrt{s_{NN}}$=7.7 GeV, the lowest collision energy accessed in the Beam Energy Scan (BES) program at RHIC, is another example which requires a multi-differential analysis.

The beam energy dependence of the two-pion interferometry and freeze-out eccentricity of pions, studied within the BES program at RHIC by the STAR Collaboration [13], combined with

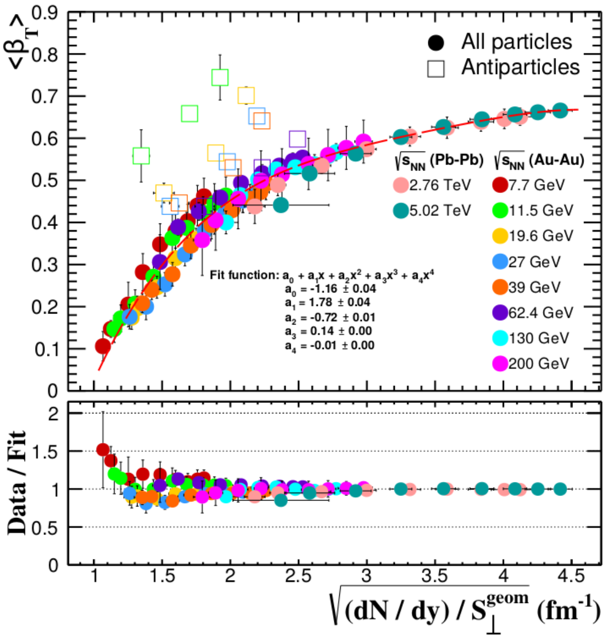

Figure 1.1.4: The BGBW fit parameter $\langle\beta_T\rangle$ as a function of $\sqrt{\frac{dN}{dy}/S_\perp^{geom}}$. The dashed red line is the result of the fit using a 4^{th} order polynomial function. Bottom: the Data/Fit ratio [12].

the previous results [14, 15, 16, 17, 18, 19, 20] evidence a minimum of the freeze-out radius in the collision energy range which will be accessed by the CBM experiment (Figure 1.1.5).

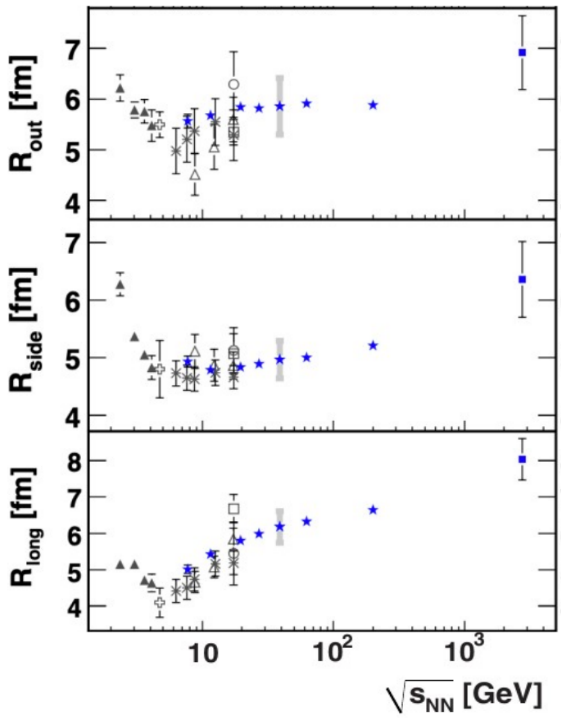

Figure 1.1.5: Energy dependence of HBT R_{out}, R_{side} and R_{long} at mid-rapidity as a function of collision energy ([13] and references therein).

Is the change from hadronic to partonic degrees of freedom causing such a minimum ? How this depends on different species and different transverse momentum of the correlated particles?

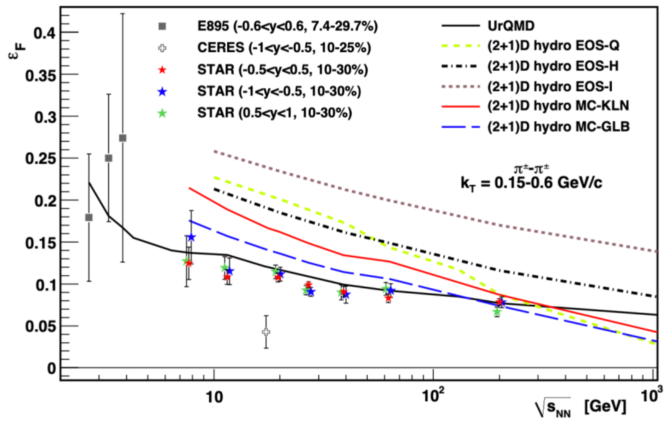

Figure 1.1.6: The eccentricity of pions as a function of collision energy for mid-central Au-Au collisions ([13] and references therein).

The freeze-out eccentricity [13] is another observable which could discriminate among different theoretical approaches (see Figure 1.1.6). As could be observed in Figure 1.1.6, the error bars of the estimated eccentricity are very large below $\sqrt{s_{NN}}$=10 GeV.

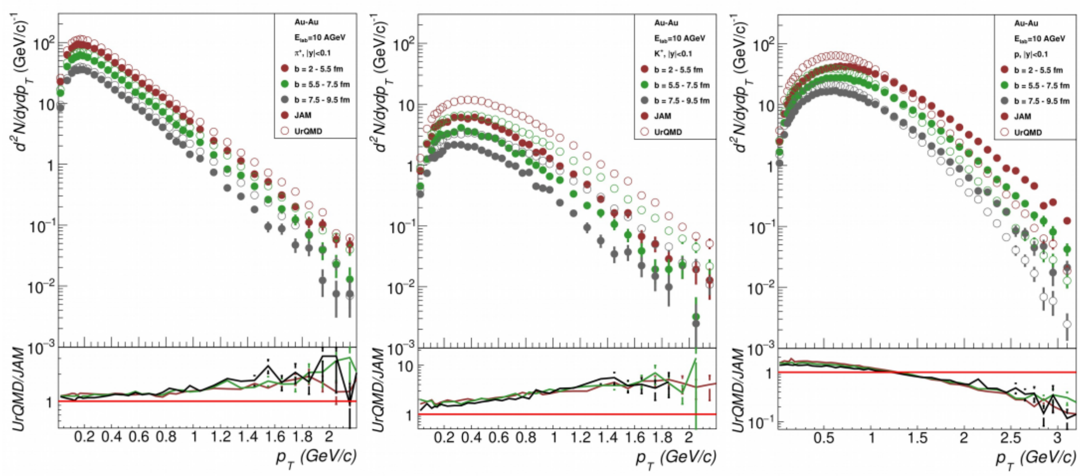

Figure 1.1.7: Transverse momentum distributions of π^+, K$^+$ and p, for three centrality bins in Au-Au collisions at E_{lab} = 10 AGeV, predicted by the UrQMD [10] and JAM [11] models and the ratios between the results (UrQMD/JAM).

In Figure 1.1.7 are presented the transverse momentum spectra for π^+, K$^+$ and p generated using the UrQMD and JAM models for the Au-Au collision at E_{lab}=10 AGeV. As expected and known from data analysis within the present running experiments and mentioned in the beginning of this chapter, it is very important for a precise estimate of the yield, average transverse momentum and fit parameters using different expressions suggested by theory, to access the low p_T region, below the maximum of the corresponding distribution.

As could be discussed in the following chapters, this is not a trivial task in high particle multiplicity, high counting rate and high background environment. Using a special architecture for the inner zone of the CBM-TRD sub-detector, this could be achieved with high efficiency and accuracy.

1.2 Design outlines for an Enhanced Tracking TRD *(A.Bercuci)*

The Multi Wire Proportional Chambers (MWPC) with signal pick-up electrodes are a standard technology for measuring position information of particles in experiments from low to ultr-relativistic energy collisions experiments. Their draw-back in terms of position measurements, namely their one-dimensional information, is linked to the actual working principle of using the charge amplification in the high electric fields created close to a charge collecting wire (anode). The anode wire direction breaks the symmetry of the detection plane and generates two methods for extracting the position information: along the wires, of continuous character, by using the induced signal in capacitive coupled electrodes and perpendicular, of discreet character, by registering firing anode wire index. Since the two methods for charge measurement, induced and direct, differ, one would need different devices (FEE) to register them. Using such devices, an unbiased 2D position measurement as needed in tracking, can only be obtained by using two detectors, mounted in parallel and rotated with 90^o with respect to each other. A possibility to partially overcome such limitations is to use GEM detectors with high granularity read-oput electrode but with additional costs.

In the CBM TRD TDR, a uniform design is offered for all the regions of the TRD stations, with various construction parameters tuned to the expected particle rates of any particular chamber. The design is mainly focused on providing $\pi - e$ separation without emphasizing on position determination. For the last observable, a classical solution of rectangular pick-up electrodes is used, which provides position resolution in only one direction (along anode wires). For the direction perpendicular, the dynamics of the detector response is mainly concealed with rare exceptions of particles entering close to pad-rows boundaries, cases when some position information can be recovered. The new designed proposed here, is intended to eliminate such a limitation and provide two-dimensional position information together with a better uniformity of the energy measurement over detection area.

For the most forward polar angles covered by CBM-TRD, where the counting rates could reach values up to 100 kHz/cm^2 and the local charged particle multiplicity is high, a new TRD design is proposed, with read-out granularity of 1 cm^2 and modified read-out topology. The key improvement for the new design is a finer control of detector dynamics on the direction perpendicular to the anode wires, with interesting consequences for all TRD observables, especially on the position. The design, conserves the active area thickness of 12 mm of the TDR prototype to maintain the same absorption volume for the TR but proposes a read-out technique for measuring two times the induced signals in pick-up electrodes (pads). This is done by pairing triangular shaped pick-up electrodes in two configurations, rectangular and tilted (see Fig. 2.3.8 left), based on a preamplifier ASIC capable of summing differently paired input channels. The effect of the two-fold read-out of signals has clear advantages:

- **identically designed anode read-out** electronics to identify the firing wire index;
- **enable 2D measurements** while still keep continuous/discrete limitations between the two directions;
- **redundant charge deposit measurement** for improved PID;
- **reduced systematic effects** in position determination by charge sharing for hits close to pad boundary wrt those on pad center and elimination of fake merging of clusters at pad-row boundaries;

The pick-up electrodes are shaped as rectangular triangles of (7.3+0.2) × (26.8+0.2) $mm^2 = 1\ cm^2$ with 0.2 mm gap between pads. The pad signals are not processed directly but paired first from two pads, by summing the charge from the current pad with the previous, respectively next pads.

The actual pairing optimizes the S/N ratio by increasing the charge collection area for each FEE input channel to 2 cm^2 and also cancels the geometrical variation over pad area due to the triangular shape[1]. The dimensions of the pads are tightly connected with the ROC parameters, especially the anode wire pitch of 3 mm, which is correlated with the *total* length of the pads of 27 mm. Moreover, positioning of the anode wires wrt the pad plane, is strictly controlled, such that the anodes are positioned identically wrt to pads for all rows, symmetric wrt the middle of the pad row.

The position sensitivity of the TRD-2D prototype has heuristic implications on the physics topics to which the TRD system can contribute:

- **stand-alone tracking :** is possible with at least two TRD-2D stations. The stand-alone tracking is mainly efficient for electrons where STS contribution is marginal. The extrapolated position resolution is matched with outer TRD detectors (STS, ToF).
- **improved track matching at low p_T :** the track probability of crossing the blind spot of STS is largest at low p_T. Such tracks are hard to seed in STS but are easily prolonged if the seeding is done in the TRD. Most of such tracks are reaching the TRD modules from the inner zone.
- **improved charged particle identification :** by correcting the systematic effects in energy deposit reconstruction through anode wire identification. One can disentangle the hits of which the charge cloud is fully read-out by pads (middle row) with respect to those which are produced close to row boundaries.
- **position reference for CBM :** is obtained by using the position calibration for TRD using static 2D masks, method which is independent of systematic effects of e.g. tracking and material budget.

1.3 Physics performance *(A.Bercuci)*

The physics topics to which the TRD detector is used in the CBM experiment at SIS100 are detailed in the TDR. Here we will a detection focus on the modifications brought by the replacement of the most inner 10 modules of each layer from the default proposal by chambers constructed using the design outlined in section 1.2. New possibilities reachable using the improved tracking design will be described in the end.

1.3.1 Spatial distribution of low p_T particle in TRD

From tracking and identification point of view it is important that an experimental setup is structured such that it offers redundant or/and complementary information to account and correct for systematic effects of its individual detection systems. Such case is nicely illustrated by following the **p** and $\boldsymbol{K^+}$ spatial distributions. In order to have a realistic estimation of such effect the following prerequisites are fulfilled. The simulation is done for Au-Au central collisions at 10 AGeV using the CBM geometry with realistic mechanical details. For a beam rapidity of $y = 1.532$ one can select particles at mid-rapidity with $|y_{CM}| < 0.25$ and register their impact position on the inner part of the TRD wall for different reconstruction conditions.

In Fig. 1.3.1 the mean p_T distributions at mid-rapidity of primary **p** and $\boldsymbol{K^+}$ are shown at $z = 550$ cm (fourth TRD station in the electron SIS100 setup). The chambers boundaries for the inner zone are also outlined in the figure. The color code describes an expansion pattern of the interaction products with $< p_T >$ values increasing from center to the periphery. Due

[1]The variation of the effective pad area wrt the charge amplification position between the top and respectively base of the triangular pad.

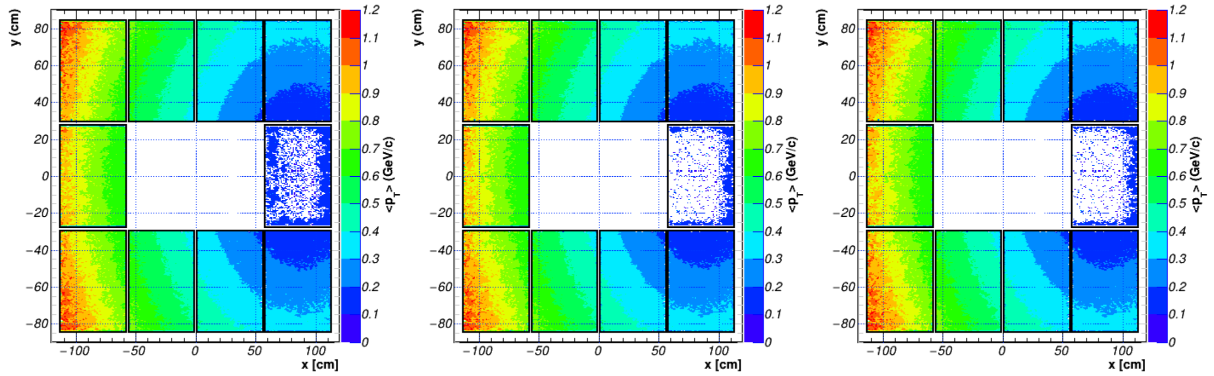

Figure 1.3.1: Mean p_T distribution at mid-rapidity of **p** and $\boldsymbol{K}^+$ in the inner zone of the last TRD station for a selection $|y_{CM}| < 0.25$ for different tracking stages: propagated STS seeds (left), attached TRD hits to STS seeds (middle) and MC matched TRD hits to particle (right).

to magnetic field the **p** and $\boldsymbol{K}^+$ products are bent at larger angles than the non interacting projectiles (Au) which are confined to the beam pipe. They reach the inner modules of the TRD station but for the lowest p_T the efficiency of STS seeding is low (see Fig. 1.3.1 left) as seen for chamber at $x = 85.5\ cm$ and $y = 0\ cm$. Additionally, the track quality for these cases is poor and the tracking efficiency is low in this region as can be seen by comparing left and middle plots in the same figure or Fig. 1.3.2 right. Obviously for such cases the stand-alone TRD tracking is the only alternative to recover some of the dynamics of the interaction. We emphasize that since TRD is outside the magnetic field, TRD by itself can not contribute to the p_T estimation but it can provide a precise seed for several scattered STS hits which can not seed a track by themselves and also form a bridge for the ToF hits in view of PID estimations. Thus the whole physics program at low p_T has to be constructed around the TRD stand-alone tracking capabilities.

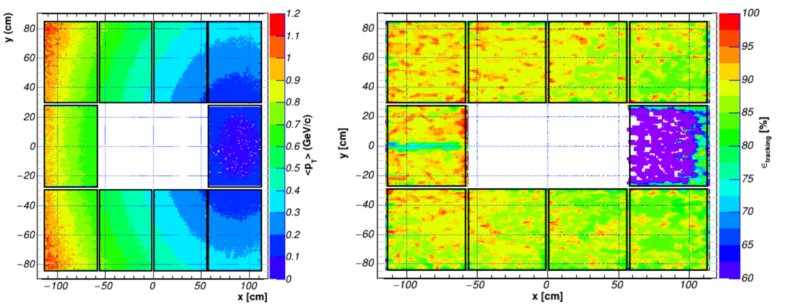

Figure 1.3.2: Mean p_T distribution at mid-rapidity of **p** and $\boldsymbol{K}^+$ for all particles which are reaching the inner zone of the last TRD station and have at least three hits in the STS (left) and the efficiency of STS seed tracking in TRD for the same selections (right).

A MC analysis of collision products which are detectable in the TRD stations and also have enough STS information (at least 3 hits) to recover the particle p_T is shown in Fig. 1.3.2 left. By comparing this representation with the middle plot from Fig. 1.3.1 one can see the geometrical complementary in terms of acceptance between STS and TRD systems (chamber at $x = 85.5\ cm$ and $y = 0\ cm$). In terms of quality the efficiency distribution from Fig. 1.3.2 right shows a slight deprecation with decreasing p_T from 90% to 80% but a huge drop around lowest p_T values of less than 60 % (same TRD inner chamber).

A similar case is presented in Fig. 1.3.3 for $\boldsymbol{\pi}^\pm$. The mean p_T distributions at $0.7 < y_{CM} < 0.9$

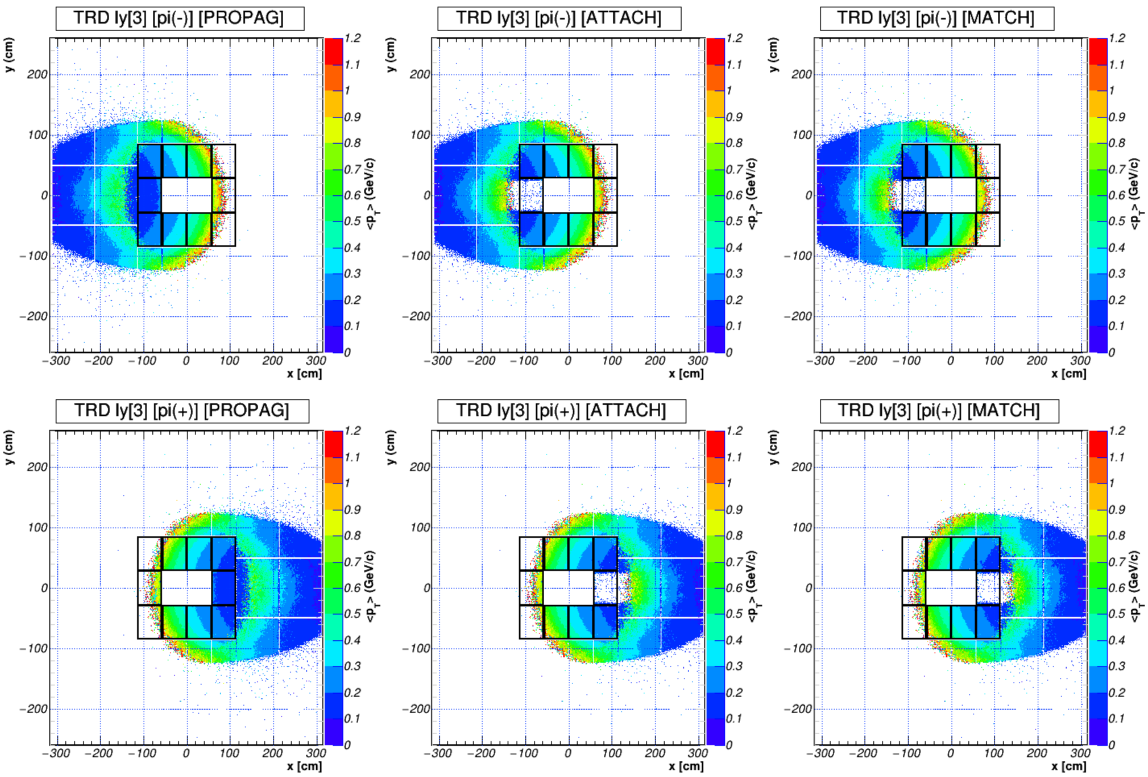

Figure 1.3.3: Mean p_T distribution of $\boldsymbol{\pi}^-$ (upper row) and respectively $\boldsymbol{\pi}^+$ (bottom row) in the last TRD station for a selection $0.7 < y_{CM} < 0.9$ for different tracking stages: propagated STS seeds (left), attached TRD hits to STS seeds (middle) and MC matched TRD hits to particle (right).

is shown for the entire TRD last station (outer chambers limits are emphasized in white). One can see the same central expansion pattern of interaction products and the dipole structure of charged particles created by the magnetic field. One can see again that chambers at $y = 0\ cm$ for various x are, depending on rapidity cut and particle identity, depleted of STS seeds due to deflection by the CBM magnet.

1.3.2 Electron component seen in the TRD

The main emphasize of the TRD physics program as detailed by the TDR is on the electron component and its identification wrt the π background. Besides the PID capabilities of the TRD wrt electrons the subject of having them propagated to the detector in the first place and eventually the systematic effects on their dynamics is totally left to seeding detectors. Therefore, we would like to provide here, further evidence for the necessity of a stand-alone TRD tracking.

In Fig. 1.3.4 the reconstruction of track-able electrons and positrons is presented. An absolute yield, at the level of the first station of the TRD (410 cm from the target in the electron SIS100 setup), is presented on the left hand side of this figure. The outline of TRD chambers is presented in the figure, in black for the inner zone, gray for the intermediate zone and orange for the outer parts. On the right side of Fig. 1.3.4 is represented the ratio of electrons which are actually seeded and propagated to the TRD. The distribution reach a maximum value of 30 % for areas uncorrelated to the input. Further, the quality of the tracks is analyzed by requiring the interaction with the TRD system, namely the attachment of TRD hits to tracks.

In Fig. 1.3.5 the tracking quality of the electron component is analyzed by presenting the efficiency of several track classes, based on MC truth attached to tracks and TRD hits. The

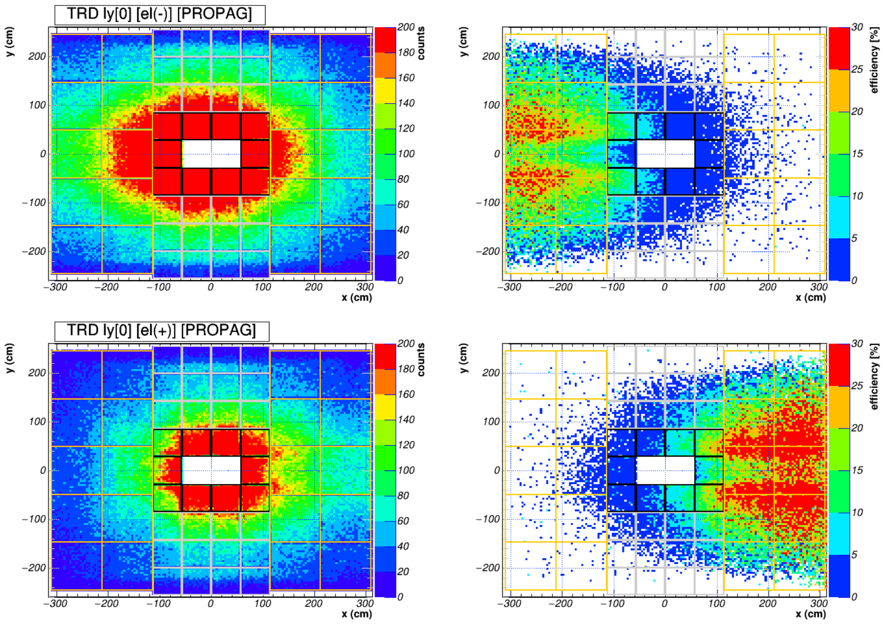

Figure 1.3.4: The electron component (upper row) and respectively positron (bottom row) seen by the TRD if all trackable tracks are considered (left) and the efficiency of the actual STS seeding wrt TRD hit matching (right).

results for electrons are displayed on the top row in the figure and for positrons on the bottom row respectively. The left column represent the correctly matched (MC tagged) tracks and TRD hits which reaches a maximum value of 70% of the generated seeds. The wrong TRD hits attached to tracks are labeled as *"FAKE"* and are shown on the middle column with probabilities on the level of 20% for outer detectors and the tracks which are not matched with TRD hits (although they are reconstructed see section 5.3) are presented in the right column of Fig. 1.3.5 and labeled as *"MISS"*. It is important to emphasize the regions included in inner chambers at $x = \pm 85.5\ cm$ and $y = 0\ cm$ for electrons and respectively positrons which form an efficiency pattern clearly distinct from the surrounding areas wrt very low *"MATCH"* probability and very high *"FAKE"* and *"MISS"* values. Obviously, the efficiency patterns shown here are not related to intrinsic TRD geometry/reconstruction but are an effect of seeding quality and as such are clearly motivating an approach of seeding from TRD.

1.3.3 Secondary particle production

The TRD system is designed as a light system with an average material budget over the whole detector area, i.e. including ROC frames, but without support structure, of $X/X_0 = 19.4\%$. Obviously the support structure, of which some details can be followed in section 3.2, is adding non-negligible amounts in localized regions. For downstream detectors relative to the TRD system, it has to provide an increase in position resolution at, e.g. ToF location, than the deprecation brought by increased local particle multiplicity through secondary creation. As the material budget might be considerable especially where supports are placed likewise the secondary generation might, locally, exceed the tracking capabilities thus producing an overall negative effect.

An active possibility to reduce the impact of material budget is the local identification of such particles and their tracking to material budget sources. By construction such an approach means seeding and reconstructing straight tracks with less than four TRD hits.

A straight forward approach to secondary particle production in the ToF detector and their

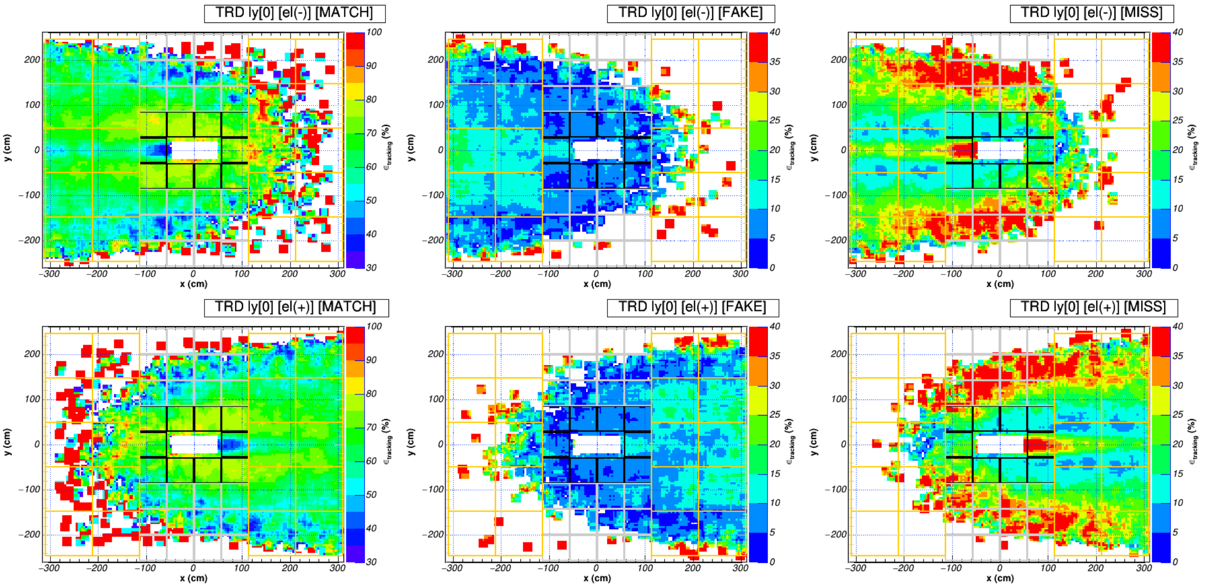

Figure 1.3.5: A measure of electron component (upper row) and respectively positron (bottom row) reconstruction quality as filtered by the TRD system for the following tracking classes : correctly matched by MC tagging (left), mis-match of STS track to TRD hit (middle) and no hit attached in TRD at all (right).

potential impact on data quality is based on observing particles rates for some typical situations. In Fig. 1.3.6 the output of a 10 AGeV Au-Au central collisions at 10 MHz interaction rate is shown in terms of particle hit rates in the ToF system - left panel and the upper limit of resolving them by STS seeding - right panel. Here, we consider ideally that any particle with at least three hits in the STS detector has 100% probability to attach ToF hits reconstructed with 100% efficiency. In reality, of course, there are systematic effects dependent on the number of STS hits, particle p_T and Particle Identification (PID), tracking, etc. which reduce it. The mean value of ToF particles hits which can be attached to STS tracks is $\approx 32\%$ with a clear spatial distribution dependent on the details of ToF implementation. The detection area centered on $y = 0\ cm$ has a particularly low efficiency wrt neighboring regions for similar arguments as those presented in section 1.3.1. Thus, about 70% of particles producing signals in the ToF detector can not be traced back to STS and are, from the tracking point of view, background, potentially disturbing the track parameters by *e.g.* fake attachments. In order to reduce such background a further

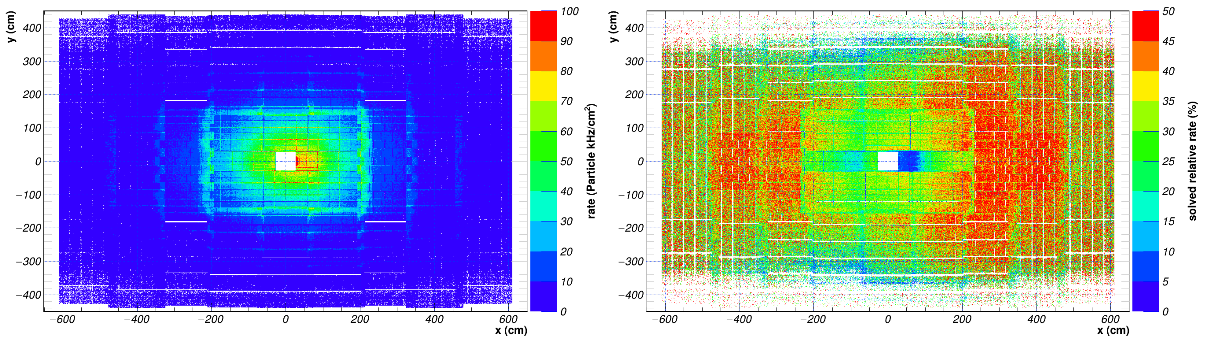

Figure 1.3.6: Expected rate of particles in the ToF stations for 10 AGeV Au-Au central collisions at 10 MHz interaction rate (left) and the upper limit distribution of resolving efficiency if only STS seeding is used (right).

classification is needed. In Fig. 1.3.7 the relative amount of untrackable particles is presented as a function of their origin wrt to the ToF entrance: entering ToF (see Fig. 1.3.7 left) and those being produced in the ToF detectors themselves or being retro-scattered (see Fig. 1.3.7 right). An average of more than 55% of untrackable particles (38% of all particles) are entering the ToF system from downstream detectors which can be partially resolved by using TRD tracking capabilities.

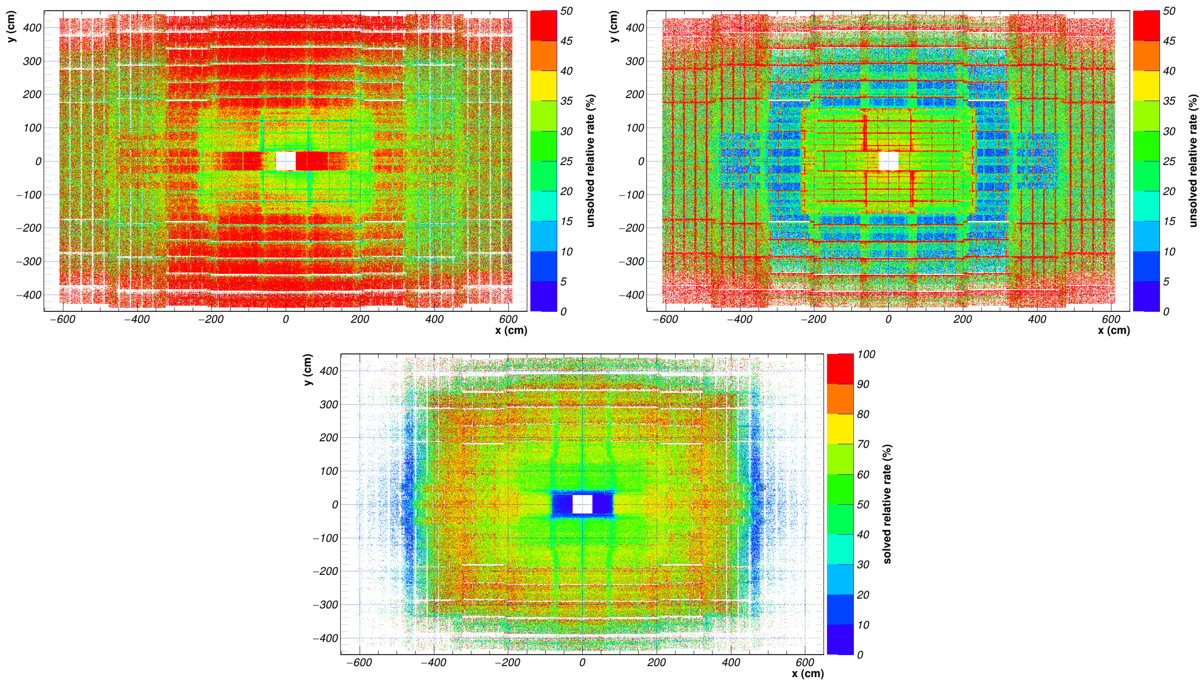

Figure 1.3.7: Top row: Relative, wrt to total (see Fig. 1.3.6 left), particle rate in the ToF detector which is *not resolved by STS seeding* for incident (left) and locally generated and retro-scattered particles (right).
Bottom row : Relative, wrt to incident rate (see Fig. 1.3.7 left), particle rate in the ToF detector which is *solved by ideal TRD seeding.*

In the bottom row of Fig. 1.3.7 the relative amount of ToF hits potentially solved by a TRD-2D architecture is presented wrt total incident rate of untrackable STS particles. The condition for TRD stand alone track reconstruction is that the particle interacts at least two times in the system. It will be seen (see section 1.4.1) that such condition approximate well a detailed reconstruction as the TRD hit reconstruction efficiency (98%) and ToF matching are high. The overall efficiency of TRD wrt orphan ToF hits is 55% (particles reaching ToF after at least two hits in TRD) which amount to ≈ 20% of the total number of hits in ToF; a value which is comparable to the one theoretically solved by STS seeds of 32%. In a realistic reconstruction such numbers might be even closer comparable as the systematic of seeding and tracking outside magnetic field from a near detector like the TRD are definitely lower than those involving STS propagation through most of the CBM setup.

In view of such potential it is interesting to study the feasibility of a parallel tracking procedure with STS and TRD seeding running independently, followed by downstream TRD propagation and hit attachment and STS propagation up to the TRD. In a final phase, the matching of the two track classes can be done in front of the TRD, eventually followed by a last phase of upstream propagation of TRD tracks to recover orphan STS hits and have some estimation on p_T for secondary tracks.

1.4 Stand-alone tracking with TRD *(A.Bercuci)*

It was shown in the last section that there are several classes of particles which are outside the tracking possibilities of an ideal STS tracker either due to limitations in the acceptance area or particles being produced outside STS fiducial volume but still impinging on the quality of physics reconstruction. In the end we suggested a new reconstruction philosophy in which the tracking can be started in the same time from STS and TRD, both processes running downstream, followed by a final merging stage at the position of TRD entrance ($\approx$ 440 cm from target in the SIS100 electron setup).

The realistic evaluation of STS/TRD parallel tracking solution proposed depends on numerical models independent of the TRD. Some of them, as *e.g.* the time-based reconstruction of hits, are available for most of the CBM systems but seeding in such environment is not. A compromise can be done by evaluating the proposal in an event-by-event scenario but also here there are missing items *e.g.* a general seeding procedure which can be applied to the TRD hits only. While waiting for such developments some estimations can be already done based on the values available for position resolution calculated from simulations or tests.

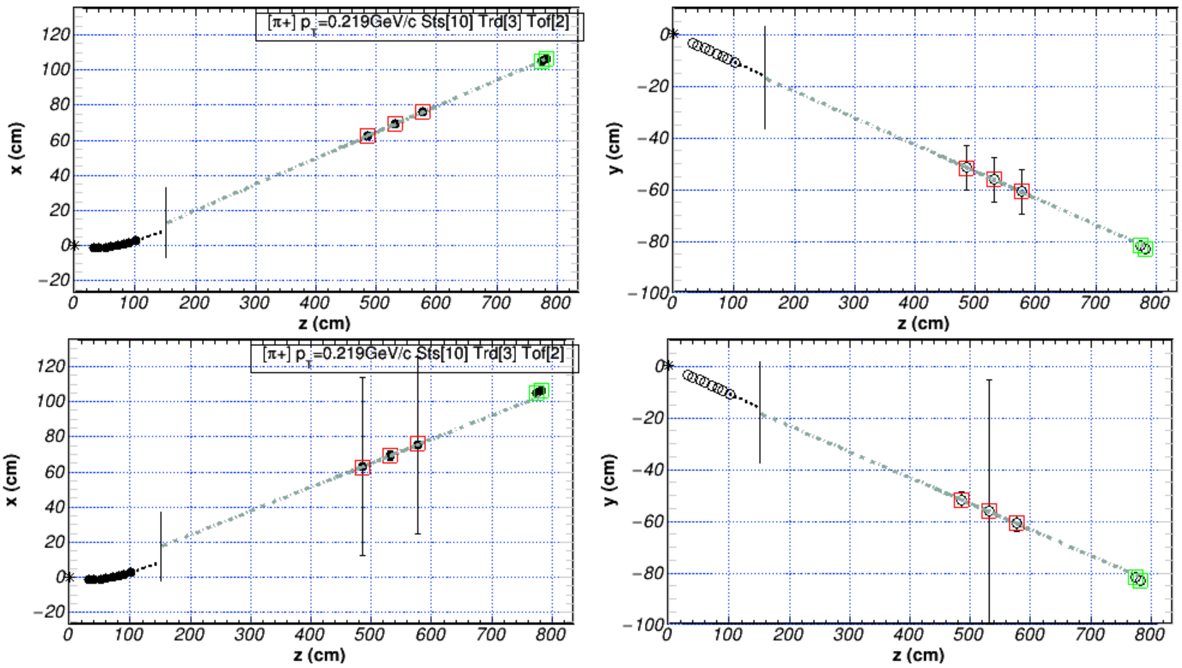

Figure 1.4.1: Basic track elements of the TRD for the two versions for the inner part design, the TRD-2D (upper row) and the TDR version (bottom row). Only hits for the following three systems are displayed in the figure : STS, TRD (red) and ToF (green).

In Fig. 1.4.1 the basic elements of TRD tracks are presented in a simplified CBM setup in which only the interactions with the STS and ToF are considered. The hits of the three systems are realistically reconstructed in an event-by-event scenario for a π^+ with $p_T = 221\ MeV/c$ from a 10 $AGeV$ Au-Au central collision. For the same track two version of the reconstruction/tracking are presented corresponding to the TRD-2D design (top row) and the actual TDR design (bottom row). The 3D track representation is projected on the $x-z$ (bending) plane (left plots) and $y-z$ respectively (right). The hits in the TRD are emphasized by red squares while those in ToF by green ones. A possible matching position is suggested at $z = 150\ cm$ from target by a vertical line. The matching between the extrapolated STS seed and the TRD respectively is displayed at the matching position by dotted lines. The TRD seed is also extrapolated downstream towards ToF to suggest the hit attachment. For each TRD hit, the estimated uncertainty is scaled by 100 in order to make them visible in the context of the whole setup and to emphasize the difference between the two solutions. The TRD-2D solution, based on arranging detectors parallel to each other in consecutive layers has $\sigma_x \approx 100\ \mu m$ position resolution in the bending plane (less than marker size in figure) and $\sigma_y \approx 800\ \mu m$ on the perpendicular direction. For the TDR version, based on rotating detectors by 90^o in consecutive layers, the one dimensional character of the measurement [2] is suggested by large uncertainties for each odd layer ($x-z$ plane) or respectively even ($y-z$ plane).

The seeding procedure is based on Cellular Automata and is applied to STS hit distribution (per event or time micro-slice). A similar procedure has to be adapted to the TRD hit distribution. Here, only theoretical estimates on the extrapolation performances is provided. The efficiency of seeding using the two sets of hits corresponding to the two TRD versions is not addressed yet.

1.4.1 Projected position accuracy of the two TRD designs

The basic ingredient for improving physics, especially in an environment dominated by event pile-ups as it is expected in CBM is precise space-time signal reconstruction. This situation is critical in the detection regions close to the beam pipe, where the particle density is highest. Here the probability of fake hits attachments to wrong seeds, the most detrimental systematic effect, increases as track is further extrapolated from its anchor points and hit has larger uncertainties. It was shown in section 1.2 that the TRD-2D design uses a technique of redundant signal reading, without increasing the number of read-out channels, for obtaining enough information to reconstruct spatially the $x-y$ position and temporally to partially correct un-isochronicity effects specific to MWPC.

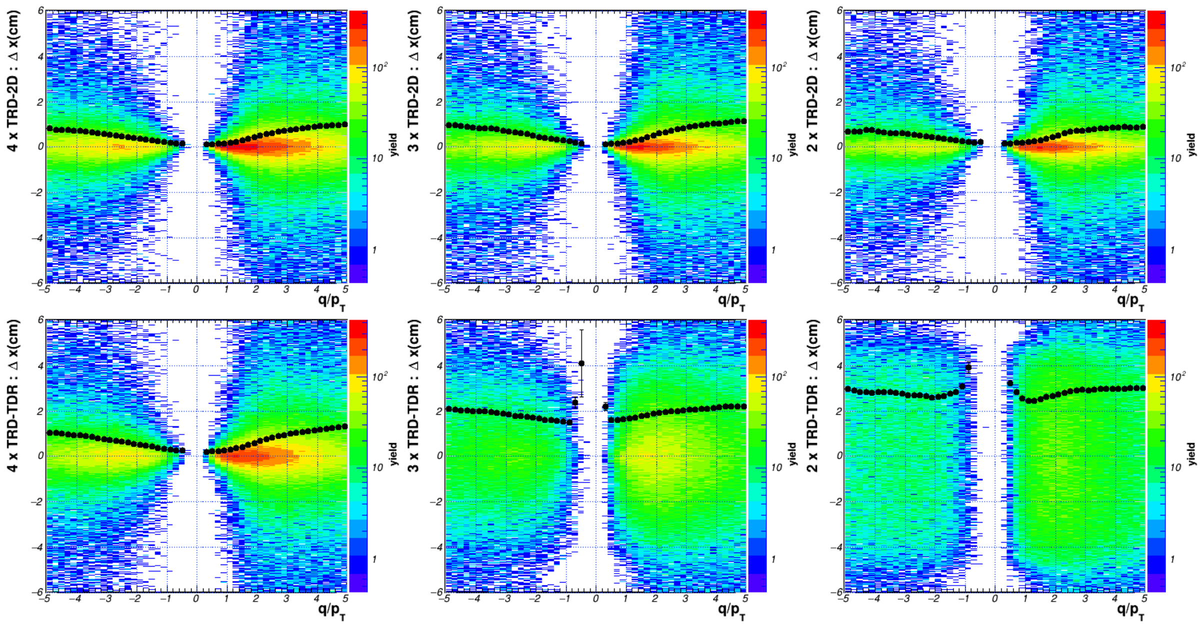

Figure 1.4.2: Distribution of the residuals in the bending plane between extrapolated TRD seed and the ToF hits as function of inverse p_T for the TRD-2D version (upper row) and TDR (bottom row) respectively and for three reconstruction scenarios: full TRD information *e.g.* four hits (left column), three (middle column) and two TRD hits only (right column).

Using the current status of CBM experiment modeling only partial tests of the performances of the 2D design can be estimated. Thus for the position accuracy of seed projecting to ToF

[2] In Fig. 1.4.1 it is presented a typical situation. There are instances when a particle can be detected in two pad rows of TRD-TDR, cases when the position resolution is improved on the second direction. A similar case happens for the TRD-2D when two anode wires (see section 5.3.3) fire simultaneously.

in a stand-alone TRD seeding scenario we can use here only the position reconstruction of the two systems and their expected uncertainties in a non-pile-up event environment. In order to correlate the two systems we use here an ideal seeding/extrapolation mechanism in which the MC information is used to select the hits defining the seed in the TRD and the attachment in the ToF. This procedure amounts to 100% efficiency of seeding/extrapolation and 0% of fake tracks[3]. Even so, in Fig. 1.4.2 the residuals in the bending $(x - z)$ plane between extrapolated TRD seed and the ToF hits as function of inverse p_T and particles charge q are displayed. Since the stand-alone TRD tracking model is also aimed at reducing the particle background the results reported here are for secondary particles, with emphasize on the low p_T region, which can be resolved by TRD as presented *e.g.* in Fig. 1.3.7. In the figure, the results for the 2D version are presented on the upper row while those for the TDR design on the bottom. For each version of a TRD detector, there are three scenarios considered: full TRD track (four hits) and respectively three or even only two hits. The drop in the hits/seed considered here is caused by geometrical acceptance only. If the reconstruction efficiency would be taken into account, the results may differ for the TDR version as it relies on hits in two consecutive layers to provide 2D pointing resolution. The resolution, σ_x (cm), as function of q/p_T is also shown in Fig. 1.4.2 as the superimposed full markers. A summary is presented in Fig. 1.4.3 where the relative improvement of pointing accuracy in the bending plane brought by the 2D design wrt TDR version is shown for the same particle classes.

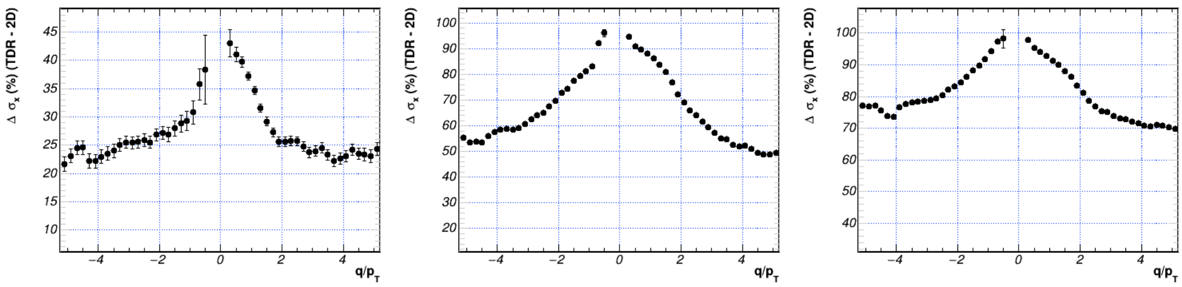

Figure 1.4.3: Relative improvement of pointing accuracy in the bending plane, of the TRD-2D wrt the TDR version, for ToF matching, for the three reconstruction scenarios from Fig. 1.4.2.

In Fig. 1.4.3 the ration $\Delta\sigma/\sigma^{TDR}$ in the bending plane $(x-z)$, is presented for $p_T > 200MeV/c$ and charged particles, for cases when only partial TRD information is available. The average values, integrated over momentum, charge and PID, for both spatial projections, are presented in Tab. 1.4.1.

	4 hits		3 hits		2 hits	
plane	$\Delta(\sigma)$ (mm)	$\epsilon(\sigma)$ (%)	$\Delta(\sigma)$ (mm)	$\epsilon(\sigma)$ (%)	$\Delta(\sigma)$ (mm)	$\epsilon(\sigma)$ (%)
$x - z$	1.4	23.4	12.1	73.5	21.8	85.7
$y - z$	-2.0	-30.4	-1.9	-12.2	11.6	49.8

Table 1.4.1: Relative pointing accuracy to ToF detector of the TRD-2D design wrt TDR for the ideal case of MC track seeding and extrapolation.

The loss of accuracy of up to 2 mm of TRD-2D wrt TDR, seen in the $y - z$ plane for *3 and 4 hits*, is due to the arrangement of detectors in consecutive TRD station for the two versions. Additionally, since the results contain only geometrical acceptance, *3 hits* tracks are detected by the last stations which, in case of the TDR solution, yield an increased accuracy on $y - z$ detrimental to the $x - z$ plane; therefore the *3 hits* scenario should be averaged over x and y for more realistic estimates.

[3]It will be shown that some estimates can be inferred based on current status of the model for such effects.

Concluding, we would state that TRD stand-alone tracking is a reconstruction step which should be implemented besides the STS driven CBM tracking. Advantages of such a procedure would be a relative easier (less systematic errors) seeding procedure (no magnetic field) and a higher position accuracy wrt downstream detectors. Also for the low p_T tracks, reconstructed without magnetic field bias, the resulting reconstruction efficiency should be more uniform over the entire dynamic range. Besides such limitations as discussed in Tab. 1.4.1, it is clear that the 2D design offers better and more resilient results for ToF matching tuned to its different precision values on x and y. A similar result can be obtained for the two TRD systems if the extrapolation towards STS is followed.

1.4.2 Extending the kinematics of CBM by using the TRD-2D design

In order to quantify the impact on the physics program of the CBM experiment by using the TRD-2D for the inner part of each TRD station, a representation of the available kinematic area based on the proposed design is suggestive.

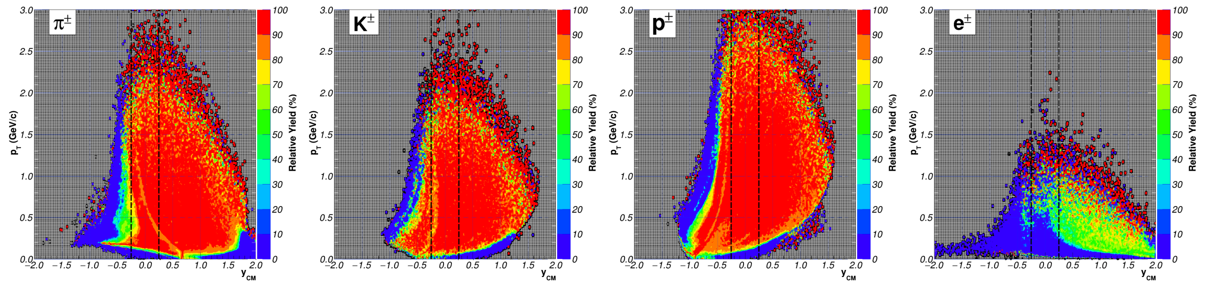

Figure 1.4.4: Efficiency of default STS seeding/propagation wrt MC particles reaching the TRD. From left to right, primary pions, kaons, protons and electrons generated within STS acceptance.

The efficiency of particle reconstruction for 10 AGeV Au-Au central collisions for the SIS100 electron geometrical setup is shown in Fig. 1.4.4 for primary $\pi^{\pm}$, $K^{\pm}$ and $p^{\pm}$ and for $e^{\pm}$ generated within the STS detection range. The mid-rapidity region is also indicated for $0.25 < y_{CM} < 0.25$ in the figure by dotted lines. The efficiency is estimated with reference to all particles having at least three interactions in the STS and two in TRD fiducial volume wrt those being propagated correctly to the first TRD layer by default STS seeding. Additionally, only those particles are considered, for which the p_T can be estimated by ideal TRD stand-alone tracking. The blue regions correspond to kinematics outside STS acceptance within the current simplified simulation model[4]. For the electron component, the contribution of particle generated in upstream detector is neglected although some decay analysis can be performed in such situations

By using the TRD-2D to populate the inner zone of the TRD stations we can reconstruct, in an idealized stand-alone tracking, particles which can interact only twice in the detectors[5]. Here the seeding of stand-alone tracks is done again based on MC information. In Fig. 1.4.5 the improvement brought to the general reconstruction in CBM in terms of extension of kinematic space is presented wrt default STS seeding (top row) and TRD-TDR usage for stand-alone seeding/propagation (bottom row). The results are presented for each of the particle species $\pi^{\pm}$, $K^{\pm}$, $p^{\pm}$ and $e^{\pm}$ for which the identification is based on MC information. An equal important feature of using the TRD-2D detector would be also the increase in p_T resolution (see *e.g.* Fig. 1.4.3) which should be estimated based on realistic track reconstruction.

In the top row of Fig. 1.4.5, the areas marked in red (100% relative efficiency) are regions on

[4] As mentioned previously the simulation is done based on an *E-by-E* model.

[5] All other reconstruction effects which are linked with using the TRD-2D design are neglected here as they can only be properly accounted for in a realistic reconstruction.

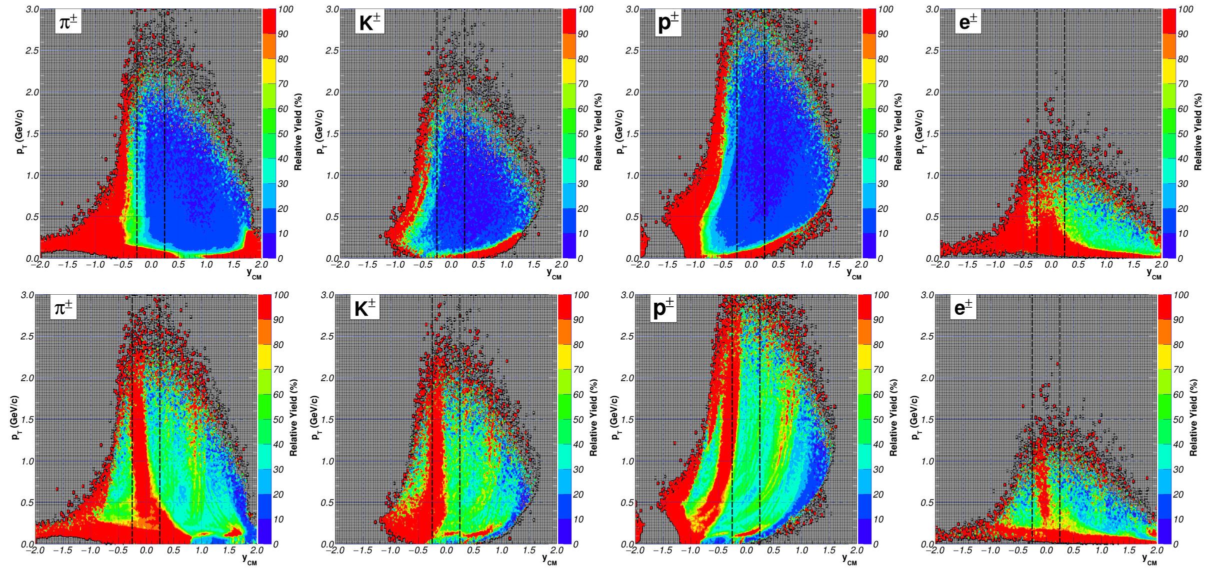

Figure 1.4.5: Extension of the kinematic space of CBM by using the TRD-2D wrt default STS seeding (see also Fig. 1.4.4) (upper row) and wrt to TRD-TDR (bottom row). From left to right, all generated pions, kaons and protons, and electrons generated within STS acceptance.

which TRD-2D stand-alone tracking is contributing only to track definition[6]. The areas with relative efficiency close to 0%, correspond to equal coverage by STS and TRD seeding, for which TRD, although not increase efficiency, can contribute significantly on increasing p_T resolution and PID (by improved matching STS-ToF). The electron component presented in the top-right figure of Fig. 1.4.5 shows the important contribution of the TRD stand-alone tracking for this component in general and the contribution of the TRD-2D design in particular.

In the bottom row of Fig. 1.4.5 we detail the relative difference between the two designs proposed for the inner part of the TRD wall wrt ideal stand-alone tracking efficiency as described above. It is seen that for the entire kinematic space the TRD-2D is superior in terms of efficiency to the default solution. There are regions of special interest for the physics program emphasized in section 1.1 which are those for which the relative efficiency is close to 100% in central rapidity region (marked by dashed lines in the figures) or those at low p_T where the efficiency is higher for the TRD-2D design.

[6] p_T estimation is based on back-propagation of TRD seeds and correct attachment of at least three STS hits.

2 Prototyping and Tests

2.1 MWPC prototypes (*M.Petris*)

2.1.1 Simple MWPC prototype

The first solution for a fast TRD detector which conserves the response function in high counting rates was a simple Multiwire Proportional Chamber (MWPC) [21]. It was designed and built with a symmetric 2 x 3 mm amplification region and 2.5 mm anode wire pitch, in order to reach the required speed of the readout signals and to reduce the possible space charge effects.

A very good energy resolution of 8.6% using an ^{55}Fe source was obtained in the laboratory tests. The effect of the high counting rate was estimated in an in-beam tests performed at the SIS18 accelerator of GSI, Darmstadt. The relative degradation of the signal in terms of pulse height (3.2%) was smaller than that in terms of integrated charge (5.0%) at the highest rate of 10^5 particles/(cm^2·s) reached in these tests. The 12.5% (2.9%) estimated pion efficiency for six (ten) TRD layers configuration at 90% electron efficiency for a Rohacell HF71 radiator and 1 GeV/c particle momentum could have been significantly improved using an efficient radiator. However, the low conversion efficiency of TR in the thin (6 mm) gas layer is the main reason for the large number of layers requiered to reach 1 % pion efficiency. The chamber signals were processed using the preamplifier/shaper hybrid version of PASA [22] based on discrete components, developed during R&D phase of the ALICE-TRD FEE, delivering semi-Gaussian signals. The experimental results showed that in a high counting rate environment a better performance is reached using the pulse height of the signal rather than integration over several time samples of it. This result triggered the development of a new front-end electronics called Fast Analog Signal Processor (FASP) for signal processing in high counting rate environment, described in section 4.1.

2.1.2 Double stack MWPC prototype

In order to maintain the counting rate performance and increase the conversion efficiency of the TR in a single TRD layer, an original TRD architecture was designed and built [23]. It is based on two multiwire proportional chambers with a common double-sided pad structure read-out electrode, almost transparent to the TRs. The configuration of this prototype is symmetric relative to the central readout electrode with identical pad structure on both sides, (back to back corresponding pads being electrically connected). In this configuration a TR photon produced in a radiator can be absorbed either in the first MWPC or in the second MWPC after crossing the readout electrode with low TR absorption, increasing significantly the conversion probability relative to the single MWPC.

The first Double-Sided TRD prototype (DSTRD-V0) of $4.5x2.0cm^2$ size had $2\ x\ 6\ mm^2$ gas thickness for TRs conversion. Double-sided pad (0.5 cm x 1 cm) readout structure was made of evaporated copper layers on a 25 μm kapton foil. The chamber was closed on both sides by aluminized kapton foils.

The ^{55}Fe source energy resolution of 8.5% using the anode signal showed that such an architecture works. The in-beam tests performed at SIS18/GSI Darmstadt, using an updated version of the ALICE - TRD PASA ASIC [24] shows that 1 % efficiency for 6 TRD layers can be reached using a regular radiator (120 foils, 20 μm thickness and 500 μm gap) at 1.5 GeV/c beam momentum. The pulse height, in direct in-beam exposure, did not show a significant deterioration up to $200\ x\ 10^3$ particles/(s·cm^2) counting rate. However, a large array based on such small chambers has a lower geometrical efficiency. Therefore, a larger size prototype with the same inner architecture was developed, increasing the size of the pads of the central double sided read-out electrode. For an appropriate granularity and two dimensional position information with a single TRD layer (see section 3.3), the initial shaped rectangular pads were split on diagonal, each triangle being readout separetely.

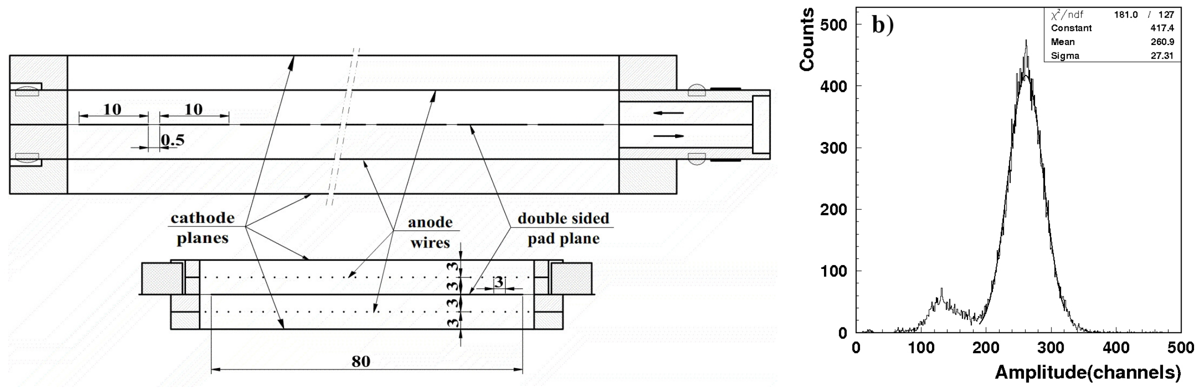

Figure 2.1.1: Schematic view of the detector structure - left side. The pulse height spectra of a ^{55}Fe source at 1750 V and Ar/CO_2 (70%/30%) gas mixture using FASP-V01 - right side.

The inner geometry of the detector can be followed in Fig. 2.1.1 [25, 26]. The readout electrode is made of a 25 μm thickness kapton foil covered on both sides with evaporated Al/Cr (200 nm/20 nm) pads, each pair of back to back pads being coupled to a single readout channel. The central electrode is almost "transparent" to the TR (absorption of about 1% for 5.9 keV X-ray of ^{55}Fe source). It has a row of 72 triangular (10 mm x 80 mm) pads along the anode wires of 3 mm pitch. The first version of the prototype (DSTRD-V1) was built with a 4 x 3 mm gain region, the second version (DSTRD-V2) was built with a 4 x 4 mm gain region.

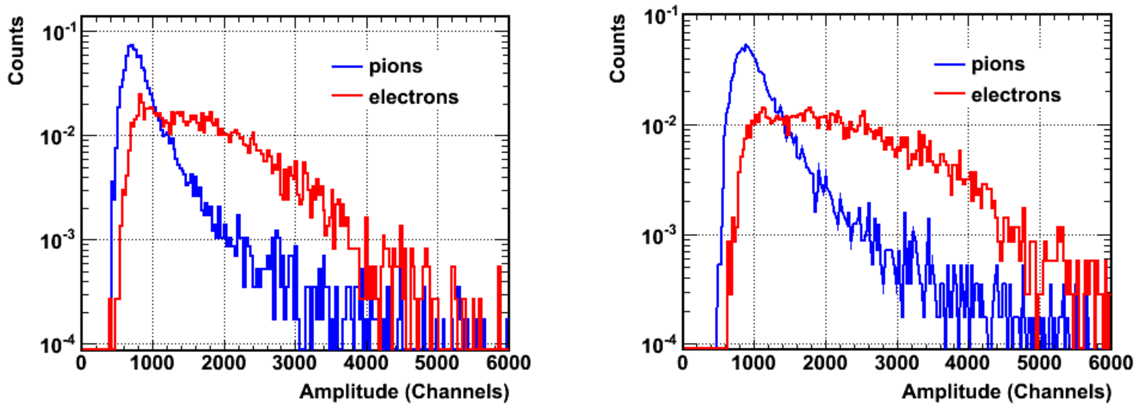

Figure 2.1.2: Energy loss spectra for 2 GeV/c electrons (red) and pions (blue) measured with DSTRD-V1+Reg2, left side and DSTRD-V2+Reg1, right side.

The functionality of the prototype was tested in the laboratory, 10% energy resolution for the ^{55}Fe source being obtained (Fig. 2.1.1 - right panel). For the pad signal processing, a new dedicated Front - End Electronics (FEE) FASP-V01 [27, 28] (see Sect. 4.1), with 40 ns shaping time and peak-sensing ("flat top") output has been used for the first time.

The detectors were tested with a mixed electron/pion beam of 1 - 5 GeV/c momenta at T10 beam line of the CERN PS accelerator using FASP-V01 ASIC and Mesytec MADC converters. Two regular foil radiators were used in the measurements: Reg1 of 120 foils of 20 μm thickness and 500 μm gap and Reg2 which is a stack of 220 foils of 20 μm thickness and 250 μm foil spacing. The differences in the TR conversion between DSTRD-V1+Reg2 and DSTRD-V2+Reg1 can be observed comparing the measured pulse height distributions for electrons and pions at 2 GeV/c shown in Fig.2.1.2 - left side and Fig.2.1.2 - right side, respectively.

Although it has a very good e/π discrimination performance [25, 26], the size of a DSTRD chamber is limited by the topology of the signal extraction (in the same plane as the readout electrode). Therefore, the geometrical efficiency of a single layer large area detector based on such an architecture is estimated to ∼76%, with a rather significant material budget introduced by the frames of individual chambers.

2.1.3 Single MWPC prototype with drift section

In order to overcome this problem we proposed a standard TRD architecture [29] of 2 x 4 mm amplification region coupled with a 4 mm drift zone (Single - Sided Transition Radiation Detector - SSTRD). It has a gas thickness identical to the 4 x 3 mm double-sided TRD prototype. The size of the drift zone was a compromise between the drift time of the ionization clusters inside the active volume and a TR conversion efficiency as large as possible. Design details of this prototype (SSTRD-V0) are presented in Fig. 2.1.3 - left side.

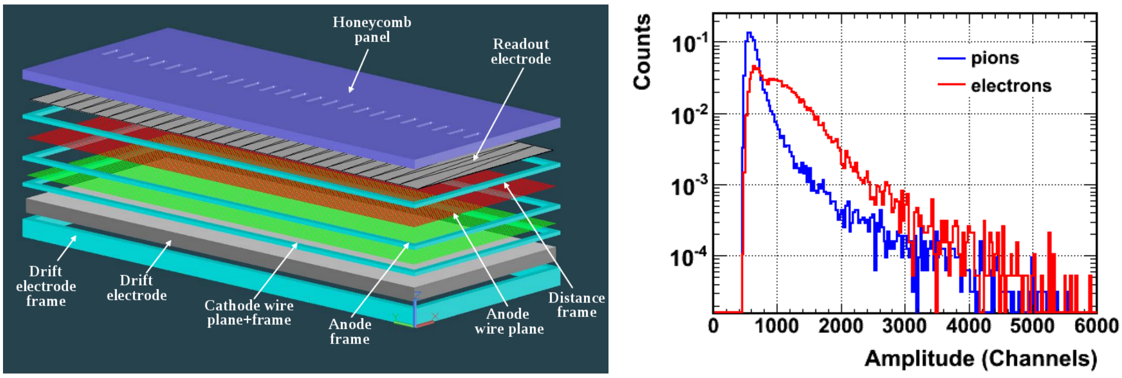

Figure 2.1.3: 3D view of the SSTRD-V0 prototype - left side. Energy loss spectra for 2 GeV/c electrons (red) and for pions (blue) measured with SSTRD-V0 using FASP-V01 - right side

The readout electrode has the same structure as for the prototypes described in section 2.1.2, the anode wire pitch is 3 mm and the cathode wire pitch is 1.5 mm. The measured energy resolutions in the laboratory using an ^{55}Fe source was 10 % with the pad signals processed using the FASP-V01 ASIC with a shaping time of 40 ns and flat-top output selection.

The pulse height distributions for electrons and pions of 2 GeV/c momentum, shown in Fig. 2.1.3 - right side were used as input for estimation of the electron-pion discrimination performance presented in section 2.2. The obtained position resolutions in both directions which define the plane of the readout electrode are presented in section 2.3.1.

2.1.4 Real size TRD prototype

The SSTRD architecture maximizes the geometrical efficiency and allows construction of large area TRD systems. In order to fulfill the granularity required by the innermost zone of the TRD stations, a readout electrode with the area of a triangular pad of ∼1 cm^2 (2.7 cm height x 0.7 cm width) was designed and produced. Two identical small chambers of 23 cm x 8.5 cm active area with this readout pad plane geometry and with the same inner layout of the wire and readout electrodes as for SSTRD (section 2.1.3), called SSTRD-V1A and SSTRD-V1B were assembled. The results of the in - beam tests (CERN-PS) are presented in section 2.3.1. Based on the obtained performances, a real size TRD prototype of 60 cm x 60 cm, called SSTRD-V2, has been assembled and tested in-beam at CERN - PS facility. In order to have a drift electrode which

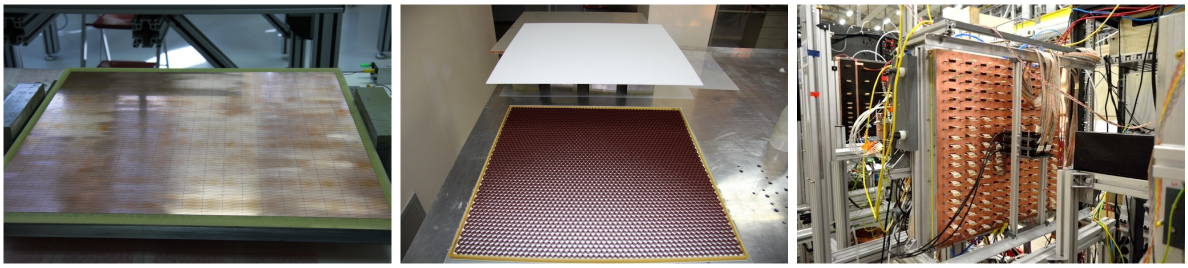

Figure 2.1.4: Photo of the readout pad-plane (left); details of the construction of the drift - electrode (middle) and the prototype within CERN-PS experimental setup (right).

minimize the absorption of transition radiation in front of the active gas volume but also with a good mechanical rigidity against the deformation due to the slight overpressure of the circulated gas, the drift electrode was built as a sandwich structure with a honeycomb material of 9 mm thickness reinforced on each side, by two one side aluminized rohacell plates, of 3 mm thickness.

In order to maintain the mechanical stability and decrease even further the TR absorption, a new structure for the drift electrode support was developed. It is based on a honeycomb layer sandwiched between two 200 μm one side aluminized carbon foils. The measured absorption for ^{55}Fe X-rays is reduced with about 9% for this version of entrance window.

2.1.5 Drift Time optimization

The maximum drift time of the ionization clusters is an important parameter for the optimization of the counter geometry and also for defining the operational parameters of the front-end electronics (i.e. shaping time). We define the maximum drift time as the longest time needed of an ionization cluster to travel from the furthest generation point relative to the anode wire to the anode wire plane. A minimization of this parameter is required by the operation in a high counting rate environment. Using the Garfield/Magboltz [30] software package the maximum

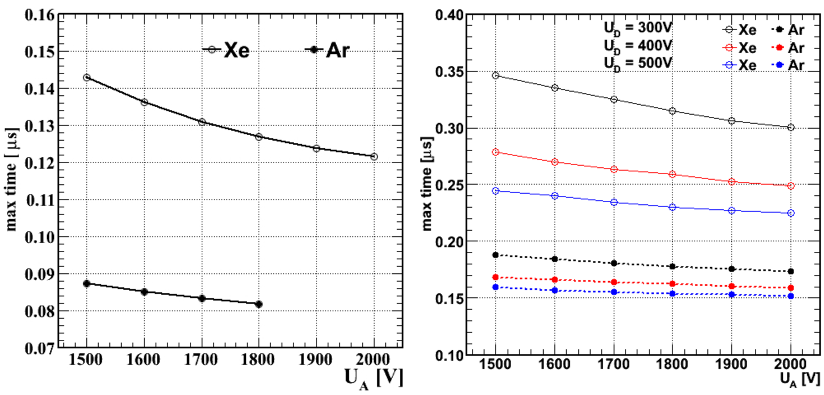

Figure 2.1.5: The dependence of the maximum drift time of an ionization cluster drifting in the gas volume on the applied anode voltage for: DSTRD-V02 (left side) and SSTRD-V0 (right side) architectures.

drift time of an ionization clusters randomly generated inside the detector volume, for different applied anode voltages and two gas mixtures of 80%Ar/20%CO_2 and 80%Xe/20%CO_2 was calculated.

In the Xe based gas mixture, a maximum drift time around 120 ns for an anode voltage larger than 1900 V for DSTRD architecture with 4 x 4 mm amplification zone (Fig. 2.1.5 - left side), was estimated. As expected, the electron drift time is much shorter in an Ar based gas mixture due to its larger drift velocity. For the SSTRD architecture, a maximum drift time of 230 ns was estimated for Xe based gas mixture and 500 V drift voltage (Fig. 2.1.5 - right side). The larger drift time is explained by the presence of the drift region with a much lower field and larger drift path length to the anode wires.

2.2 PID performance *(M.Petris)*

A likelihood method [31] was used to estimate the pion misidentification probability as a function of number of layers for 90 % electron efficiency for both detector architectures discussed in sections 2.1.2 and 2.1.3 (using as imput the measured pulse height spectra for electron and pions in a single TRD layer).

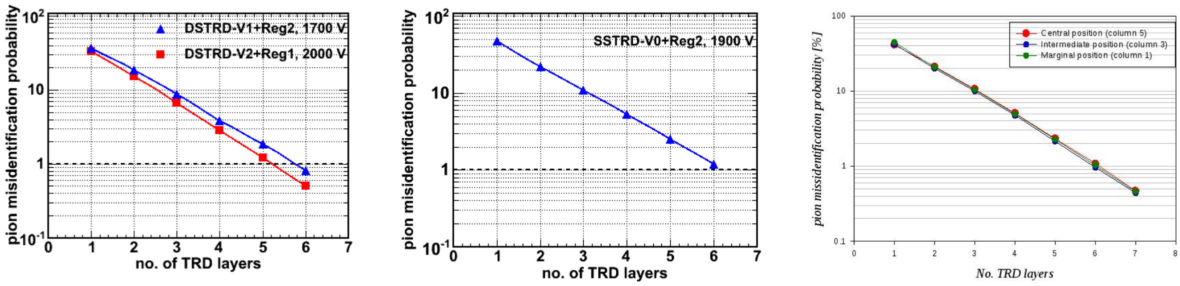

Figure 2.2.1: Pion misidentification probability as a function of the number of TRD layers for 90 % electron efficiency for: DSTRDs prototypes - left, SSTRD-V0 prototype - middle and for three position across the real size TRD prototype surface - right (the errors are at the level of the symbol size).

As could be seen in Fig. 2.2.1 a pion misidentification probability of (0.82±0.05)% is obtained for a six layer configuration based on DSTRD-V1 (4x3 mm) using Reg2 radiator and 1700 V anode voltage. For a six layer configuration based on DSTRD-V2 and Reg1 foil radiator, the pion misidentification probability is improved by a factor of 1.6, i.e (0.50±0.04) % at 2000 V applied high voltage, due to the thicker gas layer of DSTRD-V2 (4x4 mm). A value of 1.18 ± 0.07 %for the misidentification probability was estimated for a six layer configuration based on SSTRD-V0 using Reg1 foil radiator, for 1900 V anode and 400 V drift voltages. The errors are at the level of symbol size. This SSTDR chamber has the same gas thickness for TR absorption as the double sided architecture with 3 mm anode-cathode distance, however the consecutive ionization clusters with a large drift time difference between them are not integrated by the FASP-V01 version (see section 4.1.1).

The in beam test of this prototype was performed at CERN-PS (Fig 2.1.4 - right side). The detector coupled with Reg2 foil radiator, was flushed with 80%Xe/20%CO_2 gas mixture and operated with 2000 V anode voltage and 800 V drift voltage. A new designed front-end board with 2 FASP-V01 ASICs per board was used for signal processing. The pion efficiency obtained with the real size TRD prototype show that ≈ 1% for a 3 GeV/c momentum, for 6 layers of such chambers, independent on the position. Beside the detector performance, the drift and/or readout electrodes are not deformed anymore due to the slight overpressure of the circulated gas mixture. The pion suppression performance could be further improved using further developed FASP versions with 100 ns shaping time (see section 4.1.1) for signal processing.

2.3 Pad Plane Design and Read-Out (*A.Bercuci)*

It is rather obvious that the position resolution of a track reconstructed based on the rectangular pads suffers due to poor resolution along the pads. A possible solution based on slightly tilting of pads like in ALICE-TRD [32] only alleviate the problem by giving up on the good resolution across pads and adding further complications to the reconstruction. For a net improvement of position resolution using such pad geometries, a two layer set-up with layers rotated by 90 degrees relative to each other seems to be the natural choice. However doubling the amount of detector stations increases the material budget of the whole set-up and costs. A possible solution within the rectangular pad architecture would be to read e.g. the anode wires but such design would be rather poor to disentangle multi-hit events in a relatively large ROC and would require a substantial increase of the number of electronic channels. Therefore a new pad plane architecture was sought which can deliver two dimensional position information with good resolution keeping the benefits of inductive read-out and optimizing the amount of measured data.

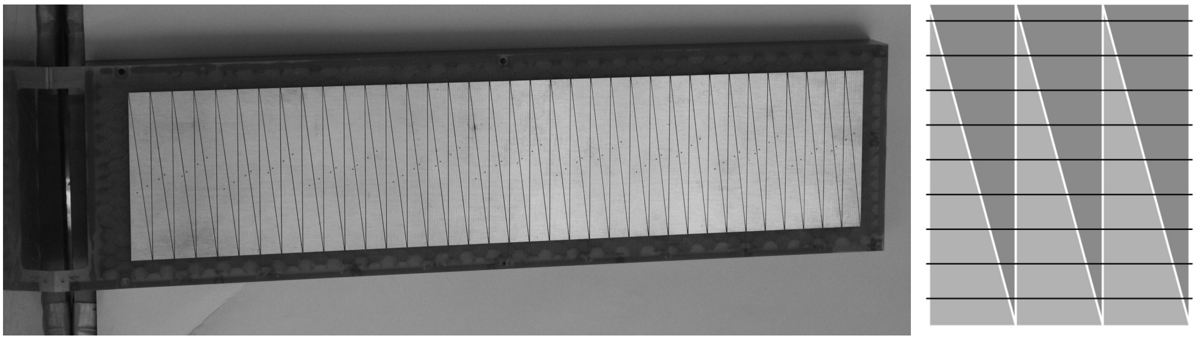

Figure 2.3.1: Photo of the readout electrode showing the triangular shaped pads (left) and a schematic view of the pad-plane architecture emphasizing the triangular pad read-out and the anode wire grid (right).

In introducing the new pad-plane architecture we start from the observation that by contrast to the position measured across pads (along anods) which is continuous in character, the positions of ionizations along the pads (across anode wires) are discreet, with a step equal to the anode pitch. To identify the anode wires hit by a crossing particle one needs beside the independent position measured by the rectangular pad architecture also an observable sensitive to the position along pads. This can be accomplished by splitting the rectangular pads of the readout electrodes diagonally. The old pad-plane architecture and position information respectively can be recovered by summing up the charge in two triangles coupled to a rectangle while the extra information can be obtained by coupling triangular pads from adjacent rectangles into a tilted pair. For clearness we will denote the coupling of triangular pads to a rectangle as *column*.

Two triangular pad architectures of the read-out electrode were used to read out the ROC. A large pad size of 80 $\times$ 10 mm^2 for the DSTRD V1 and V2 and SSTRD-V0 respectively. For the later ROCs, *i.e.* SSTRD V1 and V2, the pad size was reduced to 7.5 $\times$ 27.7 mm^2 and 0.2 mm spacing all around yielding a pad area of 1 cm^2 as suggested by detailed detector simulations (see chapter 5.1). A schematic view of the pad plane and of the anode wires used to produce the signal (thick horizontal lines) are presented in Fig. 2.3.1 (right). The induced signal can be read-out from single pads which can be coined as *triangular read-out* but also, by coupling pads to rectangles, in a so called *rectangular read-out* similar to the usual set-up.

2.3.1 Independent triangular-pad read-out

The first read-out strategy implemented in FASP-01 (see chapter 2.3) is to read out individual triangular pads. If the charge induced on the upper triangular pads is $\{q_i^{\nabla}\}_{i=\overline{1,5}}$ (see Fig. 2.3.1 right - dark gray pads) and on the lower triangular pads $\{q_i^{\Delta}\}_{i=\overline{1,5}}$ (see Fig. 2.3.1 right - gray pads) respectively than the position across columns of width w is obtained by recovering the rectangular signals by:

$$Q_i = q_i^{\nabla} + q_i^{\Delta},\ for\ i = \{1...5\} \tag{1}$$

and fitting them with a normal distribution. If no background from multi-hit is considered than, following a method described in [33], the standard deviation σ, obtained by a fit with a Gaussian to the column response function, is used to calculate the displacement d of a hit from the center of the column i with the maximum charge deposition Q_i:

$$d = \frac{1}{Q_{i-1}^2 + Q_{i+1}^2}\left(W_1 + W_2\right), \tag{2}$$

with

$$\begin{aligned} W_1 &= Q_{i-1}^2\left(\frac{\sigma^2}{w}\ln\left(\frac{Q_i}{Q_{i-1}} - \frac{w}{2}\right)\right) && (3)\\ W_2 &= Q_{i+1}^2\left(\frac{\sigma^2}{w}\ln\left(\frac{Q_{i+1}}{Q_i} + \frac{w}{2}\right)\right). && (4)\end{aligned}$$

For a given track the reconstructed position across the columns, x_{rec}, is obtained as

$$x_{\text{rec}} = d + \left(i + \frac{1}{2}\right)w. \tag{5}$$

If a constant background is also considered the signals are fitted directly with the function from eq. 6

$$\mathcal{G}(d, PRF \mid \{Q_i\}_{i=\overline{1,5}}) + P_0 \tag{6}$$

The Gaussian mean value d is selected as position observable and the reconstructed track position is given by eq. 5; an estimator for Pad Response Function (PRF) is the sigma parameter of the gaussian.

The position along anodes (anode wire identification) can be measured by constructing the observable:

$$\begin{aligned} qq &= (Q^{\nabla} - Q^{\Delta})/(Q^{\nabla} + Q^{\Delta})\ \ with && (7)\\ Q^k &= \sum_{i=1}^{5} q_i^k;\quad k = \nabla,\ \Delta && (8)\end{aligned}$$

The correlation of x_{rec} (in units of w) from Eq. 5 and qq can be followed in Fig. 2.3.2 for various sources of illumination. The sinus pattern of qq local maxima (for constant x_{rec}) as a function of x_{rec} can be used to identify individual anode wires; $n = 8$ being the number of anode wires covered by a pad row. The observed maxima in $(x_{rec},\ qq)$ correlation plot can be fit with:

$$qq(x) = A + B \cdot sin(C \cdot (x + D)) \tag{9}$$

with A, B, C and D parameters. Out of these the A and D parameters are identifying the class as they describe the mean qq value (A) and the phase shift (D). The parameters B and C are related to the geometry of the pad plane and have typical values $B \approx 0.1$ and $C \approx 2\pi$. We identify the reconstructed pairs $(x_{rec},\ qq)$ which are found around such maxima as coming from the hits amplified around a specific anode wire and thus measuring the position along the pads with the resolution of the anode wire pitch. The method for anode wire identification just described is coined Anode Wire Response Function (AWRF).

Tests using ^{55}Fe X-rays

In house, the SSTRD-V1 prototype was operated using $Ar(80\%)CO_2(20\%)$ gas mixture at atmospheric pressure and 1900 V anode and 500 V drift voltages respectively. The detector was mounted on a $(x,\ y)$ scanning device having attached a ^{55}Fe source of $1.1GBq$. The experimental setup allows uniform illumination measurements by placing the uncollimated ^{55}Fe source at a large ($\approx 40\ cm$) distance from the detector or localized illumination by placing the source close ($\approx 1\ cm$) to the TRD. Additionally, positions scans along and across pads were performed using the source close to the detector. The detector was operated on an area of 5 pad columns $\times 3$ pad rows and was self triggered by the OR signal obtained based on channel wise trigger signals delivered by FASP-01. The outputs were digitized by 32-channel peak-sensing Mesytec ADCs controlled by an GSI-MBS DAQ. In order to measure also the semi-gaussian signals (see sec. 2.5.1) all channels were delayed by 100 ns to match the read-out gate. The uniform illumination run was used to calibrate the position of anode wires as identified with the AWRF method (see Fig. 2.3.2 left).

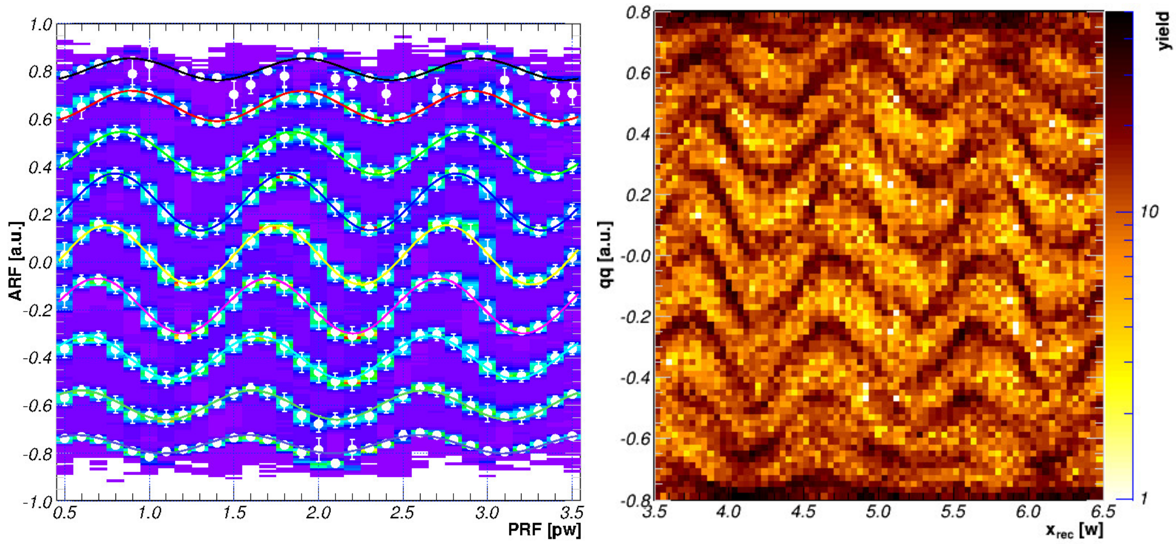

Figure 2.3.2: The correlation of the x_{rec} (horizontal axis) and qq (vertical axis) position observables from Eq. 7 as measured with the SSTRD-V1/FASP-01 for a uniform illumination with ^{55}Fe (left) and in high counting rate at CERN-SPS (right).

Low-rate first-tests at the CERN-PS

In-beam tests with a mixed electron-pion beam of $1-5\,\mathrm{GeV}/c$ momentum were performed at the T10 beam line at the CERN-PS accelerator. Three prototypes were part of the experimental setup two versions of a double sided TRD prototype [26] (here denoted as DSTRD-V1 and DSTRD-V2 see section 2.1.2) and the single sided prototype SSTRD-V0 2.1.3. They were flushed with an Xe/CO_2 (80/20) gas mixture at atmospheric pressure. Their operation parameters and the details about the experimental set-up are given in sections: 2.1.2 and 2.1.3 The performed analysis for position reconstruction is described in [25, 26].

The distribution of the residuals between the reconstructed positions across the pads in the SSTRD-V0 prototype and in the DSTRD-V2 prototype is shown in Fig. 2.3.3.a. From this distribution a position resolution *across the pads* of $327 \pm 4\,\mu m$ was obtained, assuming equal contributions of both chamber types. Using a different set-up in which DSTRD-V1 ROC, was

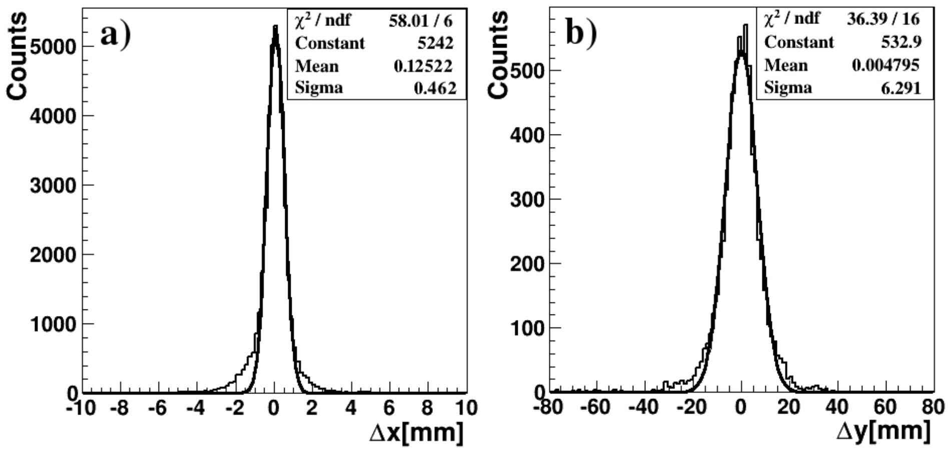

Figure 2.3.3: The distribution of the residuals between the reconstructed positions in SSTRD-V0 and in DSTRD-V2: a) across the pads; b) along the pads.

rotated by 90^o relative to the SSTRD-V0 prototype the resolution along the pads can be obtained. Using DSTRD-V1 as reference a position resolution *along the pads* of 6.29 ± 0.09 mm [29] was thus determined as shown in Fig. 2.3.3.b.

Validation of Anode Wire Response Function method at CERN-PS

In a second campaign of tests at CERN-PS the TRD prototype using the finer granularity pad plane architecture were tested with collimated mono-energetic mixed beams of electrons and pions. Here the SSTRD V1 and V2 ROC were used operated with $Xe(80\%)CO_2(20\%)$ gas mixture. The experimental setup was arranged to provide position scanning along the pads for the TRD prototype. A reference SSTRD-V1 operated in the rectangular read-out was mounted in front of tested SSTRD-V2 rotated by 90 degrees. Each of the two detector were operated on 3 rows and 8 columns yielding 24 channels for SSTRD-V1 and 2 times more for SSTRD-V2. The acquisition was triggered by plastic scintillators and RPC detectors positioned along the beam-line.

The observable x reconstructed by SSTRD-V1 can be correlated with the identified anode wire of the SSTRD-V2. Assuming parallel straight tracks crossing both detectors the correlation between the anode index (in the increasing order of qq values) measured with SSTRD-V2 on the horizontal axis and the reconstructed position x from SSTRD-V1 on the vertical axis are correlated as shown in Fig. 2.3.4. The color code in the plot represent the yield distribution of tracks crossing both detectors. For each anode index a normal fit is performed and the correlation of all maxima is deduced by a linear fit. From the slope of the fit (see box) $p_1 = 0.298 \pm 0.005$ cm we can deduce the distance between each anode wire of SSTRD-V2 as measured by the reference detector SSTRD-V1 which is identical within the error bars with the anode wire pitch of 3 mm (see chapter 2.2).

The resolution along the pads is based on the deconvolution of the position spectrum measured with SSTRD-V1 for events conditioned by anode wire identification in SSTRD-V2. A quality cut on the qq observable was also imposed *wrt.* the distribution shown in Fig. 2.3.2. If the 1D conditioned spectrum measured by SSTRD-V1 is fitted with the convolution of a Gauss distribution, modeling the cumulative resolution of TRD across pads and beam spread on the vertical axis, and a box accounting for the anode wire projected width r the later parameter can be estimated from the expression $\sigma_y = r/\sqrt{12}$. The results for conditioning on all identifiable anode wires of SSTRD-V2 is presented in Fig. 2.3.4 (right). A rather constant behavior is obtained for the central wires (index 1-5) with values close to 720 μm. The geometrical limit on

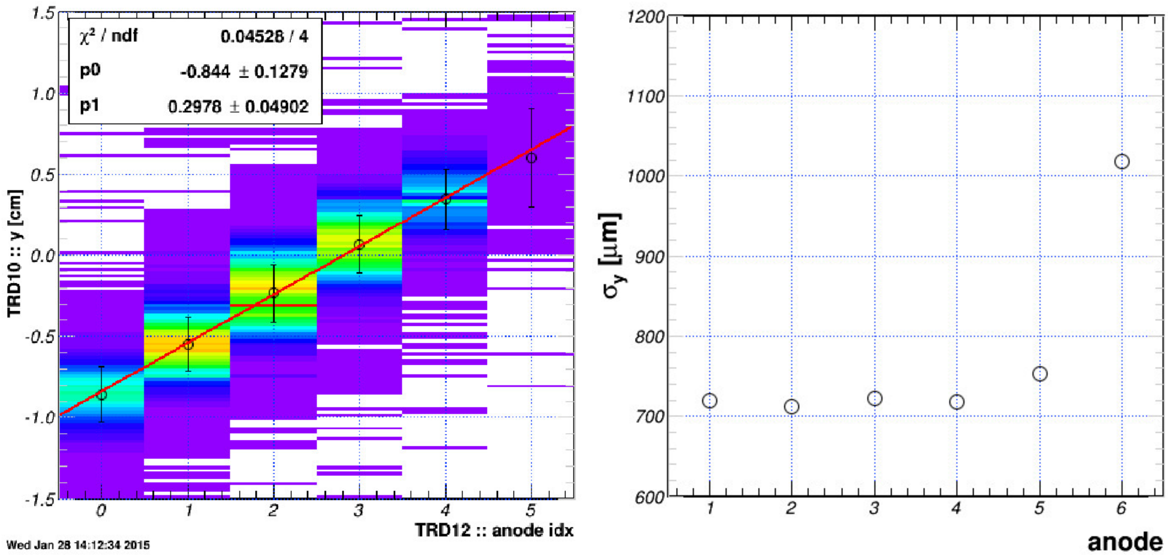

Figure 2.3.4: The measurement of the anode wire pitch using a reference TRD (SSTRD-V1) with MIPs (left); the slope ($p1$) of the fit gives the distance between anodes in cm. The position resolution along the pads as function of anode wire index (right).

the resolution can be determined from the anode pitch and has a value of 866 μm which is close to the measured value, the difference being generated by the extra conditioning in qq. For wires close to row boundaries (index 6 in Fig. 2.3.4 (right)) the results deteriorates as the image of the avalanche is shared between pad rows. For such cases a different approach should be applied which is for the moment outside the scope of the present report.

Tests in realistic CBM conditions at CERN-SPS

The final tests for the TRD prototypes were performed in conditions closed to those which are foreseen for the CBM experiment at SIS100 *i.e.* high counting rate and hit multiplicities in the detectors and a large range of particle species of various momenta. Extreme illumination conditions triggered by pile-up effects in the detector can lead to (local) signal saturation. Such effects can't be inferred in an assumption free fashion from low rate data and therefore experimental data are needed. The CERN-SPS facility can provide such conditions. Two interaction systems of 13 $A\ GeV$ Ar and 30 $A\ GeV$ Pb beams on Pb targets were used to bridge the gap from the low multiplicity conditions obtained at CERN-PS. In both cases the detector set-up consisted of two SSTRD-V1 used as reference detectors and one SSTRD-V2 as detector under test. In all cases the acquisition trigger was provided by additional detectors (*e.g.* diamond detector, RPC, and plastic scintillator) and the triangular read-out was used. ROC were always operated with $Ar(80\%)CO_2(20\%)$ gas mixture.

The detector set-up used for the intermediate conditions (13 $A\ GeV$ Ar beams) was operated with one pad row equipped with FASP-01 on each detector. The SSTRD-V2, the most upstream in beam, was operated on 42 columns (84 read-out channels) while the reference prototypes on 12 columns (24 read-out channels) each. All 3 detectors were mounted parallel to each other and aligned relative to the operated rows and the whole set-up was aligned orthogonal to the target position at a polar angle of 15 deg.

The experimental set-up was used to investigate position resolution in both coordinates in extreme conditions. To render the data as clean as possible from external assumptions only the linear track model is considered as the linear correlation of the hits reconstructed in the 3 stations which include also the mis-alignments between detectors. In order to assure proper track identification only events with one cluster per detector were selected. Additionally a cut on the energy per cluster was imposed to clean the data sample from *e.g.* secondary δ electrons). In order to estimate the resolution, the linear correlation of the position residuals between $(SSTRD-V2,\ SSTRD-V1A)$ and $(SSTRD-V2,\ SSTRD-V1B)$ was investigated [34]. Solving the distribution for its eigenvectors is equivalent to finding two uncorrelated observables, one proportional to the mean resolution of the TRDs and the other to the illumination profile of the detectors. In order to account for pad-to-pad variations, mis-alignments of the detector and dependence of the resolution on the track inclination the distribution was differentiated *wrt.* SSTRD-V2 column. Such method provide robust results relevant for systematic effects in the ROC-RO-DAQ chain.

If x_2, x_0 and x_1 are the reconstructed position across pads in the $SSTRD-V2$, $SSTRD-V1A$ and $SSTRD-V1B$ respectively and if the correlation $A = x_2 - x_0$ with $B = x_2 - x_1$ is observed than the quantity:

$$V = e_0 * A + e_1 * B \tag{10}$$

with e_0 and e_1 the eigenvalues, is proportional to the TRDs resolution. Assuming that all three detectors have equal resolution one obtains:

$$\sigma_x = \sigma_V / \sqrt{(e_0 + e_1)^2 + e_0^2 + e_1^2} \tag{11}$$

with σ_V being accessible experimentally from a gauss fit of the V distribution.

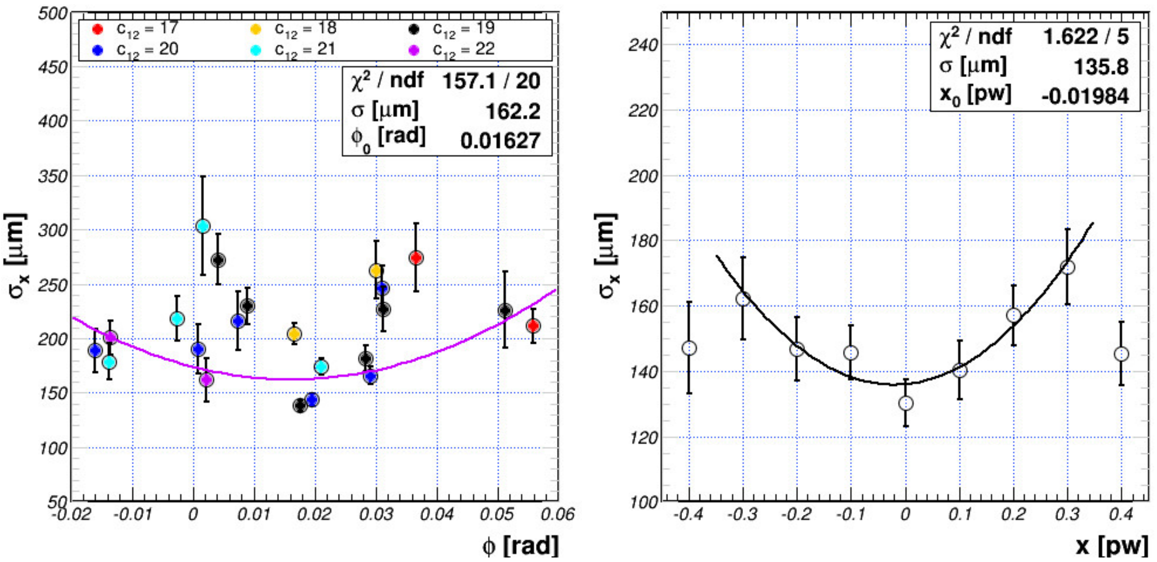

Figure 2.3.5: Mean TRD resolution across pads as function of track inclination based on SSTRD-V2 column selection (see color mapping detailed in the legend) - left and as a function of charge sharing detailed by the deviation from pad center - right.

In Fig. 2.3.5 the mean resolution of the TRD (all prototypes being considered identical) is presented as calculated based on eq. 11 for different data selections based on the largest column signal measured in the SSTRD-V2. Using mechanical measurements between the target and the TRD and the orthogonal from target to the detector surface obtained from analyzing the shape of the yield distribution as function of SSTRD-V2 column index one can estimate track inclination. The results obtained for each SSTRD-V2 column selection are emphasized by a different color as detailed in the legend of Fig. 2.3.5 -left. Error bars are determined from the Gauss fit of V. As one can see, the reaction products are seen simultaneously in the 3 detectors for 6 columns of SSTRD-V2 running from column 17 to column 22 with a maximum on $19-20$. A parabolic fit is also shown in Fig. 2.3.5 - left which yield a maximum resolution of 162 μm at normal incidence.

The same quantity was analyzed wrt. the incidence per TRD column as shown in Fig. 2.3.5 - right in units of 10% of pad width (*i.e.* 770 μm). Data were conditioned such that only clusters within the specified range expressed in pad width units were selected in all three detectors. The distribution over ϕ was integrated. A clear minimum is observed in the middle of the pad ($x_0 \approx$ 2% pw) with a value of 135 μm. From the two dependencies shown in Fig. 2.3.5 one can see that the best detector resolution at $\phi = 0$ and $x[pw] = 0$ for single track events in high rate/multi-hit environments is slightly larger than 100 μm.

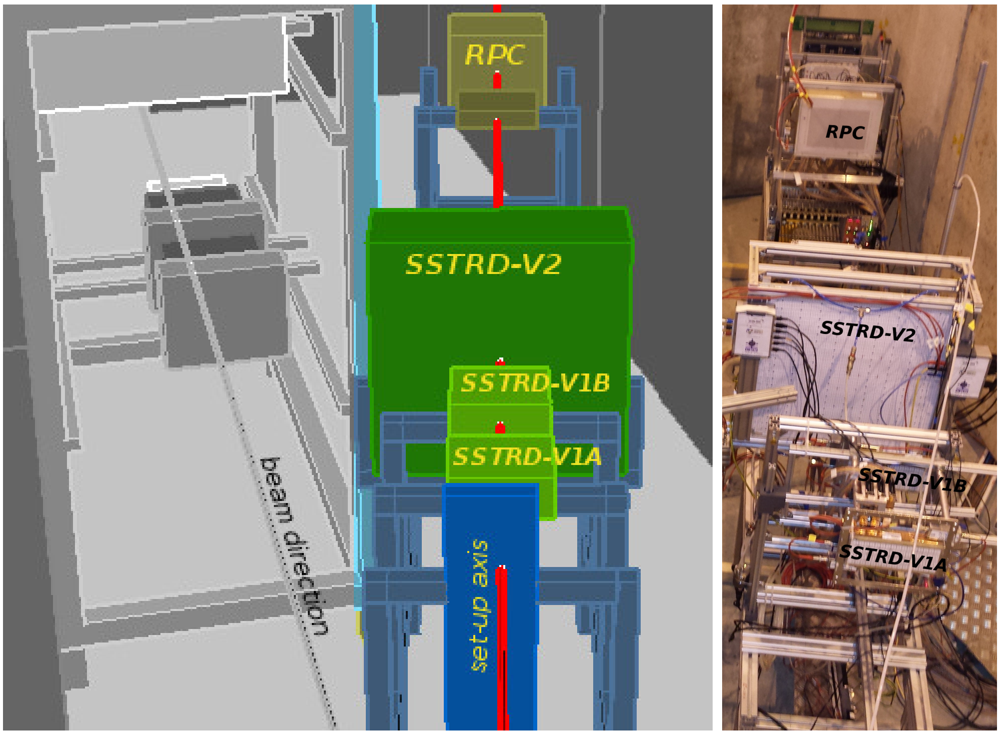

Figure 2.3.6: Detector set-up tested at 30 $A\ GeV\ Pb$ on Pb interaction system at CERN-SPS. Schematic view (left) and photo (right).

The detector set-up used for 30 $A\ GeV\ Pb$ beams is presented as both sketch and photo in Fig. 2.3.6. The SSTRD-V2, positioned this time downstream in beam, was operated on three pad rows equipped with FASP-01/02 and 16 columns/row (96 read-out channels) while the reference prototypes (SSTRD-V1) on one row of 12 columns (24 FASP-01 read-out channels) each. All 3 detectors were mounted parallel to each other and aligned relative to the operated rows.

A detailed calibration procedure was implemented to adjust the gain of each FEE channel based on injecting a given signal on the anode grid. A specific calibrated signal spectrum is shown in Fig. 2.3.7 - left, for each channel of 2 FEE boards equipped with the FASP-02 ASICs. A constant signal at 1200 ADC channels is observed which is produced by a pulser running in parallel with data acquisition. The pedestals are also calibrated as can be observed in the band centered at ADC 0 channels.

Using the position of reconstructed clusters in the 3 stations and a simple matching algorithm one can reconstruct straight tracks. Details of the analysis can be found elsewhere [35]. Worth mentioning here is the interaction point reconstruction result which is shown in Fig. 2.3.7 - right. The Pb target is placed at 160 cm from SSTRD-V1A and the whole TRD set-up is tilted with 15^o *wrt.* beam axis. Aligning the TRD detectors *wrt.* each other and extrapolating TRD tracks to such distance a peak of 0.5 cm width can be observed.

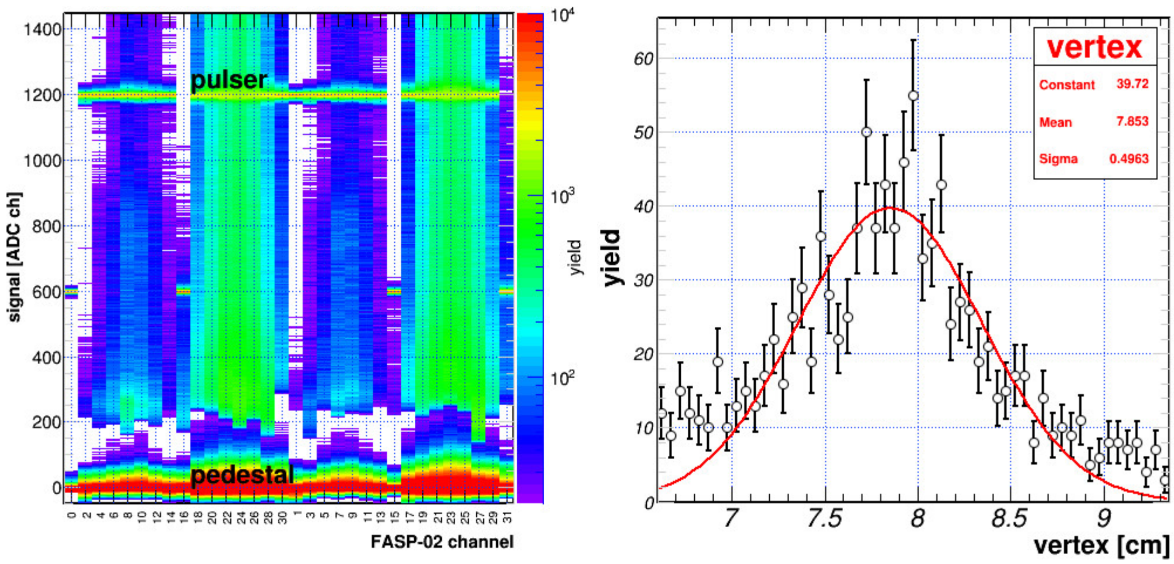

Figure 2.3.7: Calibration of FASP-02 channels at 30 *A GeV Pb* on *Pb* interaction system at CERN-SPS (left) and the interaction profile from the target reconstructed using the TRD stations (right).

2.3.2 Rectangular/Tilt paired-pads read-out

Reading out triangular pads although versatile has the drawback of variable S/B ratio and pad-to-pad cross-talk along pads (see chapter 2.4.1). In order to cure these problems a new read-out was developed in which the charge summing is performed before entering the amplification level. Thus a major improvement was introduced with the second version of FASP (see chapter 2.5.2). The charge is summed for each column on the even FASP-02 channels $\{Q_i\}_{i=\{1...3\}}$ (see Fig. 2.3.8 left - gray columns) and for each parallelogram on the odd channel $\{Q_i^{//}\}_{i=\{1...3\}}$ (see Fig. 2.3.8 left - hatched parallelograms) respectively. The signal obtained for each channel after calibration is shown in Fig. 2.3.7 (left), for the rectangular pairing on the left side of the horizontal axis and the tilt pairing for the rest.

Reconstruction of the position across pads follows from eqs. 5 and 6 with $P_0 = 0$ while for tilted pads one can apply

$$\mathcal{G}(\Delta, PRF \mid \{Q_i^{//}\}_{i=\{1...3\}}) \tag{12}$$

$$qq^{//} = \Delta + j/2 - d, \ with \tag{13}$$

$j = -1$ if tilted maximum happens before the rectangular and $j = 1$ otherwise and d from eq. 2.

Laboratory tests using ^{55}Fe X-rays

The 2D reconstruction was tested with FASP-02 using the uniform illumination with ^{55}Fe. The results are presented in Fig. 2.3.8 which shows a better separation of the anode wires *wrt.* FASP-01 (see Fig. 2.3.2). Besides the improvements mentioned above the channel wise logic marker generated by FASP-02 (see chapter 2.5.2) used in the reconstruction eliminates some of the random pile-up events rendering a better S/N ration for anode identification. Such read-out configuration appears to be the best candidate for operating the central part of the TRD wall as it inherits all features of triangular/FASP-01 read-out but adds the possibility to disentangle pile up events which are produced in extreme illumination conditions and allows for a better position resolution along wires due to the very good separation of anode wire characteristic lines. Such goal can be easily reached by decreasing the anode pitch [35].

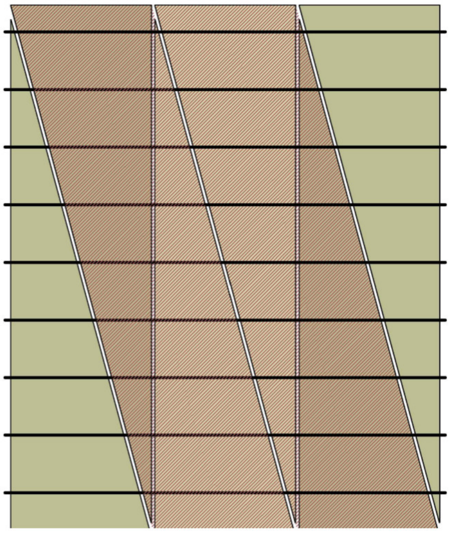

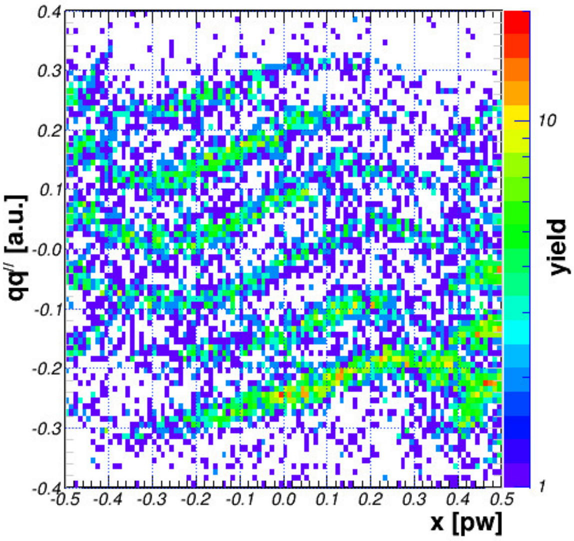

Figure 2.3.8: A schematic view of the pad-plane architecture emphasizing the tilted/rectangular pairing read-out and the anode wire grid (left) and the corresponding AWRF plot obtained for ^{55}Fe illumination (right).

2.4 Simulation of the detector response *(A.Bercuci)*

The charge seen by each triangular pad was modeled by considering a point like charge multiplication located on the anode wire and its electrostatic image induced on the conductive pads described by 2 orthogonal independent normal distributions centered on it. Their integral over a pad area is proportional to the measured signal. The free parameters of the model are σ_x and σ_y describing the charge distribution across pads for variable x and along the pads y respectively. The integration was performed on a rectangular grid of size $dx \times dy = 0.04 \times (w \times h)$ [7]. Modeling a uniform illumination of 1 column was performed by scanning all anode wires span by a column in steps of 1% of pad width (i.e. 77 μm). The charge seen for each triangular pad was therefore calculated according to the approximation

$$q^{\nabla/\Delta} = \int_{-w/2}^{w/2} dx \int_{-kx}^{kx} dy \;\; \mathcal{G}(x|x_0, \sigma_x)\; \mathcal{G}(y|y_0, \sigma_y) \tag{14}$$

$$\approx \sum_{i_x}\sum_{i_y} \mathcal{G}(x(i_x)|x_0, \sigma_x)\; \mathcal{G}(y(i_y)|y_0, \sigma_y)\; d\mathcal{A}(i_x,\; i_y) \tag{15}$$

where k is the slope of the boundary between upper and lower triangular pads, $(x_0,\; y_0)$ is the charge multiplication center, $(x(i_x),\; y(i_y))$ is the center of bin indexed $(i_x,\; i_y)$ and $d\mathcal{A}$ its effective area i.e.

$$d\mathcal{A} = dxdy \quad if\ (x(i_x),\; y(i_y)) \in\ pad \tag{16}$$

$$= dxdy/2 \quad if\ (x(i_x),\; y(i_y)) \in\ boundary \tag{17}$$

$$= 0 \quad rest \tag{18}$$

Applying the eq. 5 for position across pads and eq. 7 or 13 along pads for triangular or paired read-out respectively one can render observables similar to the measurements [8]. In Fig. 2.4.1

[7] Calculations were performed for $w = (7.5 + 0.2)\ mm$ and $h = (27.5 + 0.2)\ mm$ corresponding to SSTRD pad plane.

[8] The model neglects effects like varying signal with charge deposit, charge amplification on 2 anode wires by inclined trajectories, multi-hits on single pad etc. Such effects will be studied in details as soon as the detector architecture will be frozen.

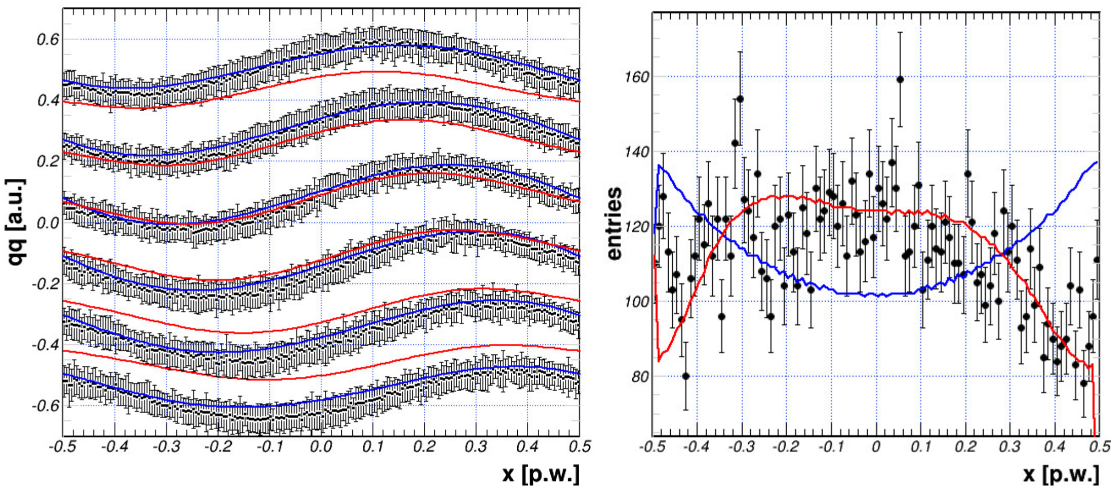

Figure 2.4.1: Comparison between 13 $A\ GeV\ Ar$ on Pb data (black) measured with the SSTRD-V1 protype and simulations with XT=4% (red) and without XT (blue) for the 2D position observables of the TRD (left) and the measured yield/column for uniform illumination as function of x_{rec} (right).

a fit ($wrt.$ σ_x and σ_y model parameters) of 13 $A\ GeV\ Ar$ on Pb data is shown for triangular read-out on 2 correlation plots; the $(qq,\ x)$ left and the $(yield,\ x)$ right. Data are shown in black as $(mean,\ RMS)$ quantified $wrt.$ x_{rec} expressed in pad width $(p.w.)$ units for identified anode wires. The model correlations are shown in blue. In order to avoid secondary effects not covered by the model, only single cluster events on all TRD stations were selected.

The results presented in Fig. 2.4.1 show a very good agreement for the $(qq,\ x)$ plot for all [9] anode wires simultaneously and for the full width of a column. On the other hand we observe that trend of the measured yield per column and for an anode wire is not explained. The opposite trend of the model $wrt.$ data suggests a strong effect when interaction happens close to the column boundaries where the relative width of the pads $wrt.$ anode wire differ the most. Such effect can be modeled by introducing a cross talk (XT) parameter [10].

2.4.1 Cross-Talk effects

The cross talk (XT) of signal between adjacent triangular pads due to capacitive coupling is defined by the effective charge seen by a triangular pad altered by its neighbors according to:

$$q^m = q_0^m + \chi \cdot q_0^l + \chi \cdot q_0^r \tag{19}$$

where q_0 is the charge seen by the triangular pad as calculated before (see sec. 2.4), upper indexes are shorthands from $m$iddle, $l$eft and $r$ight and χ is the XT parameter[11]. The results obtained with a value XT=4% are displayed as the red curve in Fig. 2.4.1. Although the matching from the $qq-x$ correlation plot deteriorates (Fig. 2.4.1 left) the $yield-x$ trend is described much

[9] Actually only the central 6 out of 8 anode wires are shown. For the other two boundary effects between pad rows start to be important and modeling become technical complicated. Nevertheless the heuristic performance of the model is not affected.

[10] Such effect is relevant for the triangular read-out. Using paired read-out the effect should be significantly diminished by construction.

[11] The model is simple but rather general as it uses one XT parameter to describe the full detector (i.e. independent of anode wire or position across pads). It is also symmetric wrt to the left and right neighbours and it assumes non zero values only for first order neighbours. A dedicated electromagnetic modeling of the capacitive coupling between triangular pads and subsequently estimation of the XT from first principles is beyond the scope of present TDR.

better thus confirming our assumption. A more explanatory model covering a larger range of data correlations is beyond the scope of this report.

2.4.2 Systematic effects on position reconstruction across pads

The reconstruction of position across pads using the Eq. 5 is biased (see e.g. [33]). Using the model described above one can estimate and correct them.

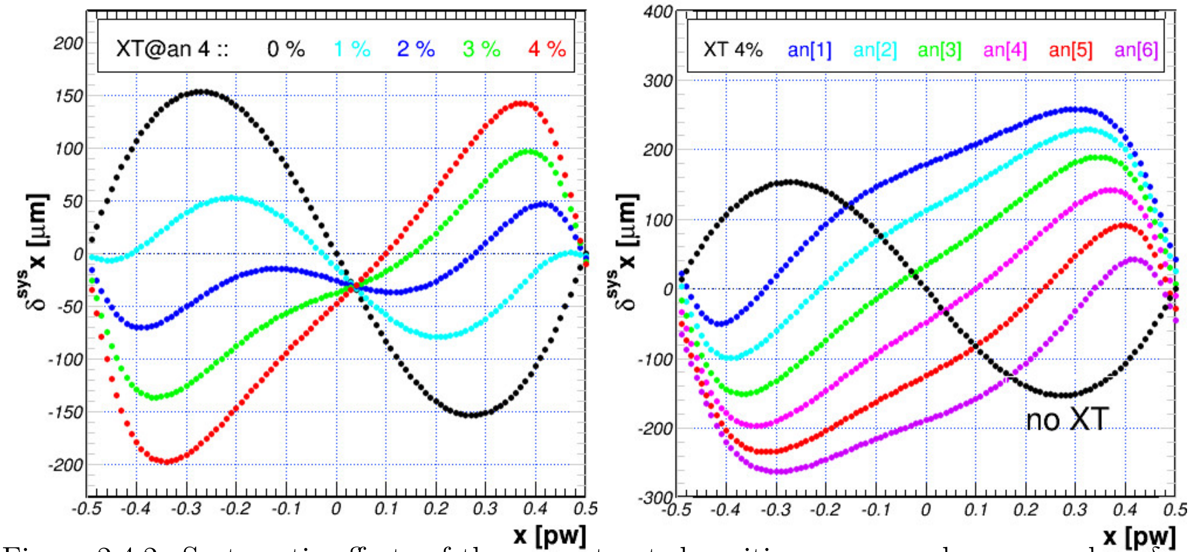

Figure 2.4.2: Systematic effects of the reconstructed position across pads expressed as $\delta x = x_0 - x_{rec}$ as function of x_{rec} in units of pad width for the 4^{th} anode and XT range $0-4\%$ (left) and their dependence on the anode wire for fixed $XT = 4\%$ (right).

In Fig. 2.4.2 the residuals $\delta x^{sys}(x_{rec}) = x_0 - x_{rec}$ between the center of the charge multiplication (see eq. 14) and the reconstructed value obtained from eq. 5 are shown as function of the reconstructed position x_{rec} for various anode wires and XT values. By selecting a particular anode (*e.g.* the 4^{th} in Fig.2.4.2 left) one can evaluate the systematic shift for XT values in the range $0-4\%$. A non negligible (wrt position resolution see chapter 2.3.1) correction to the reconstructed position across pads is identified which has the effect of *e.g.* deforming a flat spectrum as seen in Fig. 2.4.1 right. The dependence of the shift in case of $XT \neq 0$ is asymmetric wrt center pad and is anode wire dependent (see Fig. 2.4.2 right). Moreover the position for which the systematic effect is independent of XT is defined by the intersection of the anode wire with the diagonal slit between adjacent triangular pads.

In order to produce unbiased results for the reconstructed position across pads the observable x_{rec} is corrected to:

$$x_{rec}^{unbiased} = x^{rec} + \delta x^{sys}(x_{rec}|XT) \tag{20}$$

with the XT parameter as found from a fit to the data (see the red curve in Fig. 2.4.1 right).

We have determined the parameters of the model σ_x, σ_y and XT from fitting simultaneously the correlation plots from Fig. 2.4.1 on data for all operated prototypes. The data used for the fit were selected events with one cluster for each TRD station, from measurements at CERN/SPS on the 13 $A\ GeV\ Ar$ on Pb system. The results for the 3 prototypes ($2 \times SSTRD - V1$ and $SSTRD - V2$) over the full column range operated in the test beam show for the $(qq - x)$ correlation plot a values of $\sigma_x \approx 2.5\ mm$ and $XT \approx 2\%$. They are also independent of the TRD column/FEE channel due to the way they are constructed. The fit of the $(yield, x)$ correlation plot depends on the position along the prototype and is best explained by $\sigma_x \approx 3.2\ mm$ and $XT \approx 4\%$. The least sensitive parameters of the model σ_y best describes the data for a value of $\approx 3.5\ mm$. More details are presented elsewhere [34].

2.5 FEE prototypes (*V.Catanescu*)

The concept of Fast Analog Signal Processor (FASP) as an ASIC is based on the high counting rate in-beam results obtained with the very first prototypes of TRDs developed for CBM Experiment at FAIR. The final target is to have a fast amplifier for MWPC or GEM detectors used in high counting rate environments which delivers minimum information without deteriorating the detectors performance. The first two prototypes designed by the Bucharest group uses AMS 0.35 μm N-well technology [36].

The FASP ASIC has eight (v0.1), respectively sixteen (v0.2), identical channels, each processing one TRD pad (see Fig. 2.5.1-left in channels). The current signal is amplified and shaped optimizing the signal to noise ratio. The chip provides two types of output for each channel: a semi-Gaussian shaped output and a peak-sensing output (see Fig. 2.5.1-right top 2 responses).

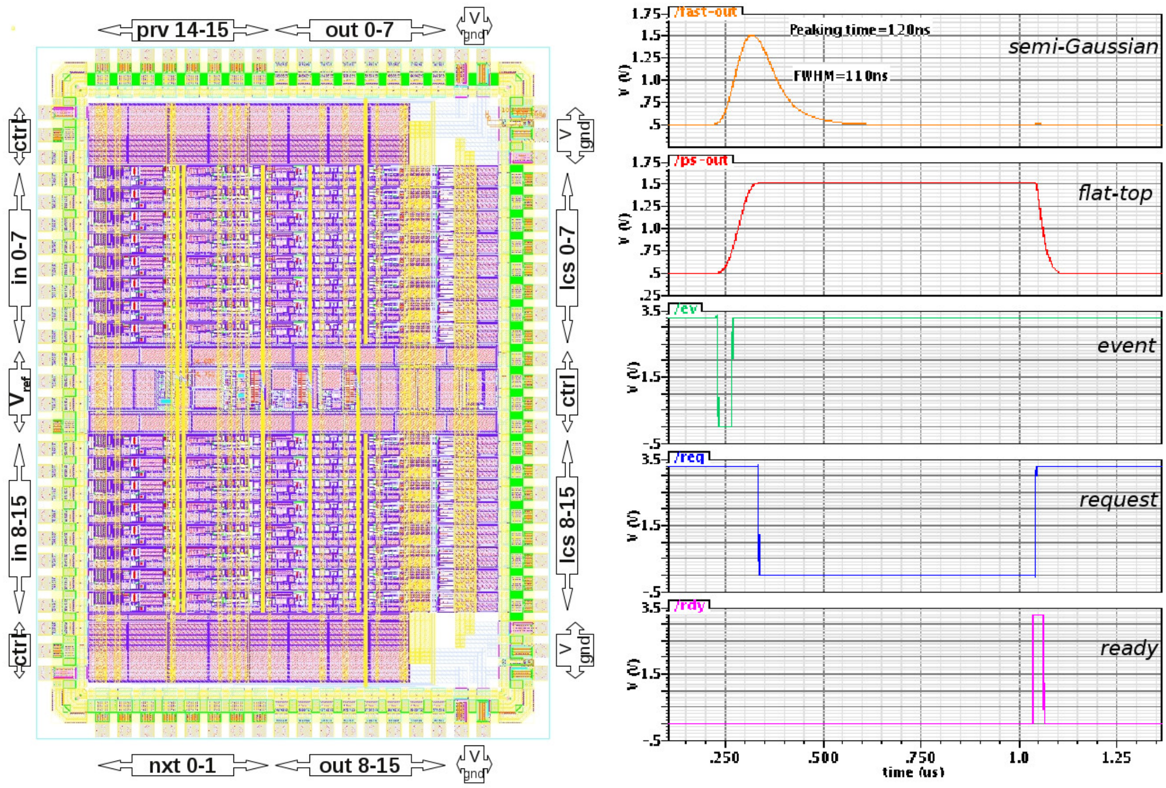

Figure 2.5.1: The layout of the FASP-0.2 ASIC with its in/out pads connections (left) and the typical analogic/logic response to a delta curent for one FASP channel (right).

An I/O interface inside the chip, working on request/grant basis, assures a correct data transfer between the output of each channel and the data acquisition system. All channels have a self trigger capability with variable threshold [37, 38] coined *chip select* (see Fig. 2.5.1-left **lcs** channels and -right the **request** signal). For testing purposes a test pulse generator is implemented into the ASIC. The most important features of the FASP ASIC [37, 38] are summarized in Tab. 2.5.1.

Table 2.5.1: The general FASP ASIC features

Average pulse rate	over 300 kcps
Charge input range	0.15 fC ... 165 fC
Input coupling / type	DC / single ended
Channel gain	6.1 mV/fC
Shaping time, (CR-RC**4, semi-Gaussian, 1-bit selection)	20 ns or 40 ns
Semi-Gaussian output pulse FWHM	62 ns (shaping time 20 ns)
	110 ns (shaping time 40 ns)
Output type (semi-Gaussian or peak-sensing)	single ended
Output voltage swing (semi-Gaussian or peak-sensing)	0 ... 1 V
Output pulse variation (semi-Gaussian or peak-sensing)	
- with temperature $T = 0 \dots 70$ C	< 0.03 %/C
- with power supply $V_\mathrm{d} = 3.0$ V ... 3.6 V	< 0.18 %/V
Output base line shift (semi-Gaussian or peak-sensing)	
- with temperature $T = 0 \dots 70$ C	$< 8\,\mu$V/C
- with power supply $V_\mathrm{d} = 3.0$ V ... 3.6 V	< 0.07]%
- with detector leakage current	$< 5\,\mu$V/nA
Channel ENC ($C_\mathrm{det} = 25$ pF)	
- for shaping time 40 ns	980 e
- for shaping time 20 ns	1170 e
Integral nonlinearity (semi-Gaussian or peak-sensing)	
- for shaping time 40 ns	< 0.21 %
- for shaping time 20 ns	< 0.90 %
Overshoot / undershoot (semi-Gaussian)	
- for shaping time 40 ns	< 0.20 %
- for shaping time 20 ns	< 0.80 %
Peak-sensing output settling time to 0.1 % of final value	< 450 ns
Peak-sensing output decay	$< 25\,\mu$V/μs
Self trigger capability	
- variable threshold (cont. adj.)	0 ... 165 fC (full range)
- hit occurrence signal	logic level
Power consumption	11 mW/channel

2.5.1 Features of the FASP-0.1 ASIC

The FASP-0.1 version ASIC of $3.15 \times 2.10\,\mathrm{mm}^2$ has the following characteristics:

i. **Good response to double pulses and high rates** was obtained using an appropriate number of shapers and values for the shaping time. In Fig. 2.5.2-left one can observe the performance on the semi-Gaussian output to a pair of delta pulses of amplitude 1.0 and 0.2 separated by 1 μs.

ii. A special circuitry in each analog channel allows a very **fast and clean recovery to charge overload.** In Fig. 2.5.2-middle the performance is shown when signal overloads of ten times the nominal range are simulated. The situation is worse when such precautions are not considered (see Fig. 2.5.2-right). The fast recovery circuits reduce the dead time of the analog channels and result in a very good double pulse separation and an excellent response to high pulse rates without base line perturbation.

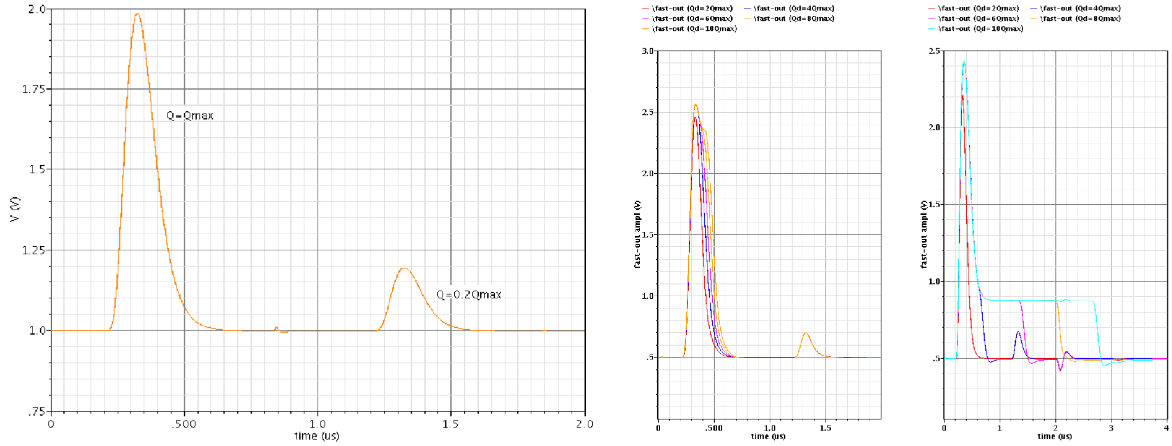

Figure 2.5.2: Semi-Gaussian output response of one analog channel to delta pair pulses. Semi-Gaussian output response of one analog channel to delta pair pulses with fast recovery circuits (left panel) and without fast recovery circuits (right panel).

iii. Specific circuits are implemented for the **restoration of output base-line** which allows to compensate the effects of detector leakage currents. For example a pad leakage current in the range of $\pm 50\ nA$ the output base line shift is reduced from shifts of 0.8 mV/nA to below 3 μV/nA as detailed CADENCE simulation show [39]. The same circuits are also very efficient to avoid a base line displacement due to high counting rates.

iv. A **shaping time selection** is implemented with a 1-bit logic input line. Two possible values of 20 ns and 40 ns are available depending on the results obtained during the tests of the TRD prototypes.

v. For each channel, a second **peak-sensing self-trigger** output (Fig. 2.5.1 -right second signal), offers a flat top pulse with a value corresponding to the peak of its semi-Gaussian output. The peak-sensing output is generated only for pulses with an amplitude above a defined threshold, generating also a self-trigger logic signal (Fig. 2.5.1 -right forth signal). The peak-sensing signal is maintained until a **ready** is received from the acquisition unit (Fig. 2.5.1 -right fifth signal). The threshold level is common to all analog channels but its value can be adjusted within the full output range of the analog channels.

Besides the features mentioned above there are also additional circuits such as: calibration pulse generator, reference and bias circuits, and also a fast input/output interface for data processing.

2.5.2 Features of the FASP-0.2 ASIC

The second version of the TRD ASIC, FASP-0.2, of die size $4.65 \times 3.45\,\mathrm{mm}^2$ was developed also in the AMS 0.35 μm N-well technology. It preserves all specifications of the previous version, but includes some additional features summarized below:

i. **16 input channels** for detector signal processing (see Fig2.5.1 -left **in** pad entries).

ii. User **selectable polarity for the inputs**.

iii. **Multiplexed analog inputs** allowing for different pad pairing (see Fig. 2.3.8-left).

iv. Capability of each data processing channel to generate a **separate chip-select, clock-synchronized logic signal** and to act as its individual ADC.

v. **Channel wise logic time signal** allows to transmit the variable threshold level or can be used for the signal peak detection according to the selection by the user.

vi. Selectable **channel neighbor trigger** to increase cluster size. Such facility is used to force flat-top generation on under threshold channels and thus increase position and energy resolution performance.

The input channel signal polarity, the shape of output signal (semi-Gaussian or flat-top), the logic time signal generation (threshold or peak-sensing), and the neighbor trigger can all be selected by the user, each via a 1-bit selection line (see Fig2.5.1 -left **ctrl** pad entries) resulting in 16 different working modes of the FASP-0.2 chip. The user can modify dynamically the control parameters via a dedicated *ctrl* link.

The main specifications of FASP-0.1 and FASP-0.2 are listed in Tab. 2.5.2, while the whole layout of the FASP-0.2 ASIC is presented in Fig. 2.5.1.

Table 2.5.2: The specifications of the FASP-0.1 and FASP-0.2 ASICs.

Specifications	FASP-0.1	FASP-0.2
Average pulse rate	> 300 kHz	> 300 kHz
Detector pad capacitance	25 pF	25 pF
Number of analog channels	8	16
Input polarity (1-bit selection)	positive	positive / negative
Channel pairing	no	yes
Charge input range	0.15 fC ... 165 fC	0.15 fC ... 165 fC
Input type	DC single ended	DC single ended
Channel gain	6.2 mV/fC	6.2 mV/fC
Shaping time / (1-bit selection)	20 ns and 40 ns / yes	100 ns [12] n.a.
Analog output type (1-bit selection)	semi-Gaussian or peak-sensing	semi-Gaussian or peak-sensing
Analog output polarity	Positive (single ended)	Positive (single ended)
Analog output voltage swing	0 ... 1 V	0 ... 1 V
Analog output DC voltage level base line (cont. adj.)	0.2 V ... 1 V	0.2 V ... 1 V
Semi-Gaussian output FWHM	62 ns / 110 ns	290 ns
Peak-sensing output plateau	typ. 400 ns (cont. adj.)	typ. 400 ns (clock dependent)
Channel ENC ($C_{\mathrm{det}} = 25\,\mathrm{pF}$)	980 e (ST = 40 ns), 1170 e (ST = 20 ns)	940 e
Crosstalk (max. signal in only one ch., no signals in others)	0.5 %	0.012 %
Crosstalk (max. signal in 15 ch., no signal in one channel)	0.7 %	0.022 %
Self-trigger capability:	0 ... 165 fC	0 ... 165 fC

variable threshold (cont. adj.)		
Logic common event output	neg. 20 ns width	neg. 20 ns width
External clock synchronization	no	max. 50 MHz
Logic signal channel wise, clock synchronized, output	no	yes
Channel synchronized logic signal for semi-Gaussian output	n.a.	to thres. level / to max. ampl.
Channel-wise synchronized logic signal for semi-Gaussian output	n.a.	neg. 20 ns to thres. level / to max. ampl.
Channel-wise synchronized logic signal for peak-sensing output	n.a.	neg. 20 ns to thres. level / neg. 14 clock cycle to max. ampl.
Channel neighbors trigger enable / disable	n.a.	yes

2.5.3 FASP Simulation

The response of the FASP ASIC was tested using CADENCE simulations [39]. The main results are summarized as follows:

i. The **typical response to delta current signals of one self-triggered analog channel signals** is shown in Fig. 2.5.1-right for an input charge of 165 fC, a shaping time constant of 40 ns, and for a channel threshold of 6 fC.

ii. The **integral nonlinearity**, for both type of outputs (semi-Gaussian and peak-sensing) and for shaping times of either 20 ns or 40 ns are below a 1 % as summarized below: In

Shaping time [ns]/Output	20	40
Semi-Gaussian	$<$ 0.47%	$<$ 0.21%
Peak-sensing	$<$ 0.91%	$<$ 0.19%

Fig. 2.5.3-left the semi-Gaussian output as a function of the input charge for one analog channel with a shaping time of 40 ns is shown. The corresponding integral nonlinearity is 0.21 %.

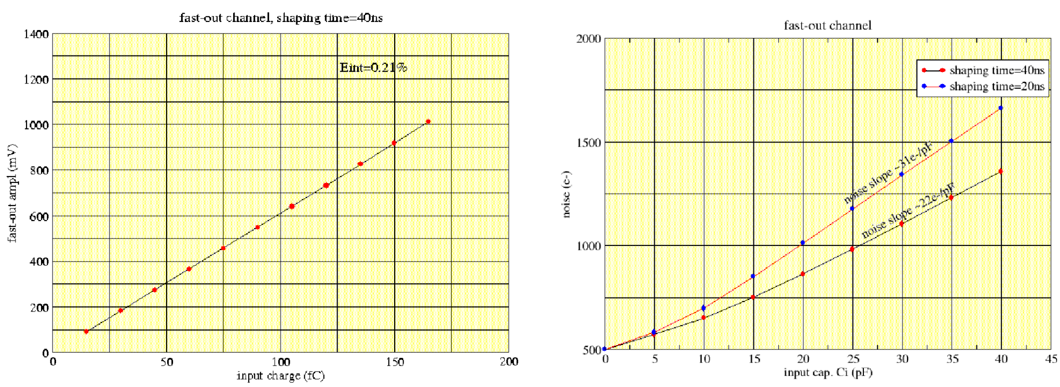

Figure 2.5.3: Integral nonlinearity for the semi-Gaussian output with a shaping time of 40 ns (left) and the ENC for the semi-Gaussian output as a function of the input capacitance C_{in} (right).

iii. The **noise characteristics** were carried out for a typical input pad capacitance of 25 pF, as well as for varying capacitances C_{in} in the range $[0,\ 40]$ pF as shown in Fig. 2.5.3-right for both 20 ns ($\approx$ 31 e/pF) and 40 ns($\approx$ 22 e/pF) shaping time values. For the typical value the simulated channel noise is 980 e and 1170 e for a shaping time of 40 ns and 20 ns respectively.

2.5.4 Analog channel response to a GARFIELD input

The FASP design has to be optimized *wrt.* two opposite requirements derived from the operation conditions of the TRD prototype:

- it has to be fast for running in high rate environments without dead-time truncation;

- has to conserve energy deposit by particles crossing the active area as the basic requirement for PID and position performances.

An optimum was reached by simulating the response of the FASP channel using the CADENCE software [39] with realistic detector signals simulated with GARFIELD [40] (see chapter 2.1.5).

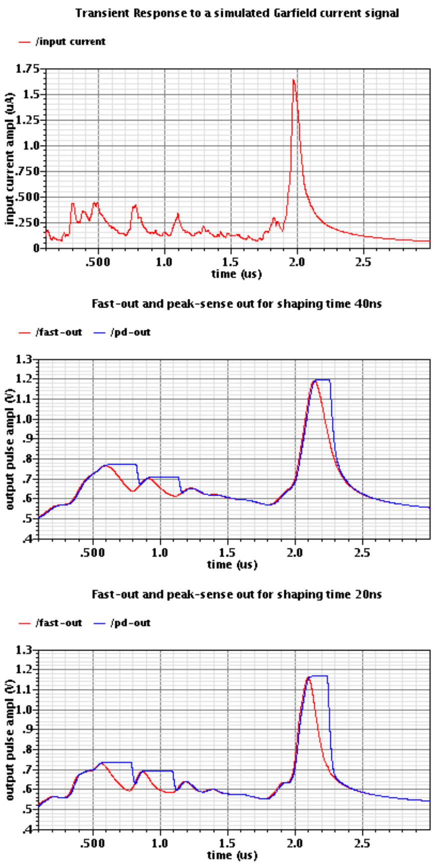

- Input signals simulated with GARFIELD

- Semi-Gaussian fast output (red line) and peak-sensing output (blue line) for a shaping time of 40 ns.

- Semi-Gaussian fast output (red line) and peak-sensing output (blue line) for a shaping time of 20 ns.

Figure 2.5.4: Analog channel response to simulated GARFIELD signals.

In Fig. 2.5.4 the transient responses of the analog channels to simulated input current signals are presented. The length of the simulated signal is 3 μs. In the upper panel the detector current signal simulated with GARFIELD is shown, which is used as input to the analog channel. The middle panel displays the results of the semi-Gaussian output (red line) and of the peak-sensing output (blue line) for a shaping time of 40 ns. In the lower panel the same two outputs are shown for a shaping time of 20 ns. For both peak-sensing cases (40 ns and 20 ns shaping time) the threshold is adjusted such that it allows only the analysis of the peaks of interest.

The two main designs for which FASP was designed are presented in chapter 2.1.2 for the DSTRD and 2.1.3 for the SSTRD respectively. It was shown (see Fig. 2.1.5 - left side) that the maximum drift time of an ionization cluster produced by a charged particle inside the gas volume, calculated with GARFIELD, was about 100 ns for DSTRD and 250 ns (see Fig. 2.1.5 - right side) for SSTRD respectively. Since the FASP amplifier was originally designed for DSTRD [26], the shaping time (ST) of this version was optimized to 40 ns, in order to process the fast signals delivered by this prototype. The linearity of the FASP output signal processed with a shaping time of 40 ns is shown in Fig. 2.5.5 - left, where the ionization clusters are randomly distributed inside the drift volume over a drift time window (DTW) of 100 ns (triangle markers). A very good proportionality and linearity of the signal to the input charge is observed. The extracted slope of 5.97 mV/fC is very close to the conversion gain and the offset of 2.43 mV is small. For comparison the FASP performance on a SSTRD prototype with maximum drift time 250 ns (square markers) is included. The observed slope of 5.17 mV/fC is lower than the conversion gain and an offset of about $\sim$ 50 mV is observed. In Fig. 2.5.5 - right the uniformity of the FASP response to tracks depositing a constant $E_{dep} = 65\ fC$ for the same configurations as used in the left panel. The standard deviation of 5 mV around a mean output value of 392 mV, which is very close to the theoretical mean of 402 mV, is small for the DSTRD architecture. For a DTW of 100 ns the average FASP output conserves the gain and the the fluctuations are rather small. For the SSTRD geometry, the rather large standard deviation of 40 mV around a mean of 289 mV shows that the FASP ST has to be optimized for an undistorted processing of such signals.

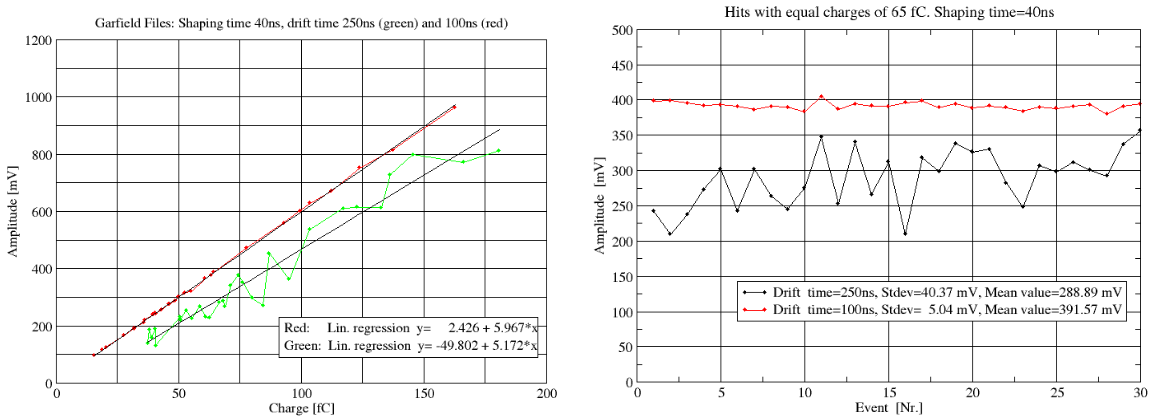

Figure 2.5.5: Linearity of the FASP response (shaping time of 40 ns) for particles of various E_{dep} $[fC]$ in DSTRD (triangles max drift time 100 ns) and for the SSTRD (squares max drift time 250 ns) prototype respectively - left and the uniformity of the signal for various tracks with fixed $E_{dep} = 65$ $[fC]$ - right.

It is obvious that the operation of SSTRD requires an increase of the shaping time to accommodate the larger DTW of such ROC architectures. The improvements in the linearity of the output signal due to an increase of the shaping time from 40 ns to 80 ns, resp. 100 ns, for a DTW of 250 ns are shown in Fig. 2.5.6 - left. For a shaping time of 100 ns, the slope of 5.88 mV/fC, obtained with a linear fit, approaches the conversion gain and the offset is reduced to $\sim$ 12 mV.

Figure 2.5.6-right demonstrates the improvements in the fluctuations achieved by an increase of the shaping time for a constant $E_{dep} = 65$ $[fC]$ delivered by various track parameters. The mean value of the distribution increases to 371 mV for a shaping time of 100 ns, and the standard deviation of the distribution is reduced to 16 mV. Based on these results, a second version (v0.2) of the FASP amplifier has been developed with a larger shaping time of 100 ns. This value can still cope with the 100 kHz/cm^2 counting rate expected in the innermost zone of the CBM-TRD

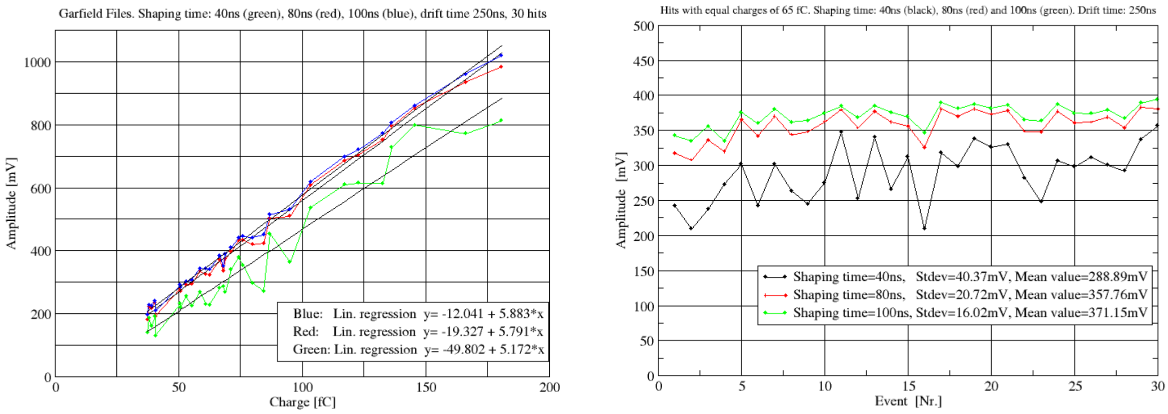

Figure 2.5.6: Linearity of the FASP response for the SSTRD prototype for particles of various E_{dep} $[fC]$ for 40, 80 and 100 ns shaping times (left) and its uniformity for various tracks with fixed $E_{dep} = 65$ $[fC]$ (right).

at SIS100.

2.5.5 Front-End-Electronics integration

FASP ASICs were integrated on prototype Frond-End-Boards (FEB) developed by the Bucharest group as interface between DSTRD and SSTRD ROC architectures on one end and various Data-AQquisition (DAQ) systems. In order to cope with both triggered and free-running DAQs sitting at large distances (several meters) the single-ended output of FASP is converted to differential and shipped over twisted pair cables.

The FASP-0.1 ASIC has been integrated on various FEBs housing 1 or 2 chips. In Fig. 2.5.7 - left an example with 2 chips is shown. The largest part of the FEB is dedicated to **Analog**

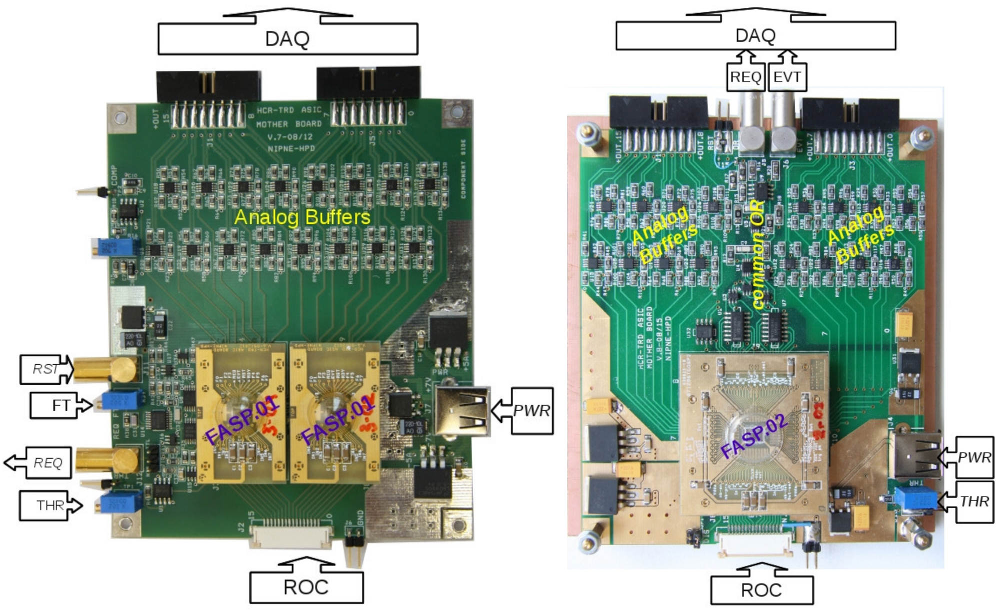

Figure 2.5.7: Two FEB versions for housing FASP ASICs and their *in/out/ctrl* functions with 2 FASP.01 chips (left) and 1 FASP.02 respectively (right).

Buffers (see Fig. 2.5.7) which besides transforming the single ended output to differential have also functions for DC compensation and extra gain such to optimally match the ADC range used to digitize the signals. For this FEB version a common request **REQ** TTL signal is provided for both chips which might be used to self trigger the DAQ. Control functions for threshold adjustment **THR** and for flat-top **FT** duration are located on board and are interfaced via simple mechanical devices. The board is powered via a USB socket **PWR**.

For the second version of the FASP a version of FEB housing 1 chip is presented in Fig. 2.5.7 - right. As this board houses its own 33 MHz CLK the flat-top adjustment **FT** and external reset **RST** are omitted and are replaced by phasing the chip output with the CLK. Threshold adjustment is still kept. From the central/top area of the chip (see also Fig. 2.5.1 - left) the channel wise *chip select* logical signals produced by FASP.02 when generating the flat-top are temporarily combined in a general *OR* to cope with the triggered DAQ used in tests. The chip-wise **REQ** signal can be used for self triggered data acquisition (see e.g. chapters 2.3.1 or 2.3.2).

3 The TRD-2D Read-out Chamber

In this chapter we summarize the modifications of the TRD-2D Read-Out Chamber (ROC) solution with respect to the TDR version in order to fulfill the tracking enhanced capabilities. We start from a Multi-Wire Proportional Chamber (MWPC) of 12 mm thickness with 2×4 mm amplification region and 4 mm thick drift region, for fast signal collection. For a low material budget in the region of highest particle multiplicity where such detectors will be installed, the mechanical resistance of the chamber was integrated with the wall structure and some modifications where also performed on the entrance window.

3.1 The active volume

The particle reconstruction at a rate of 100 kHz/cm^2 imposed a faster charge collection time wrt. the TDR version. In order to keep the Transition Radiation (TR) absorption constant a small modification was operated on the ratio of amplification to the drift region such that a $4\ mm + 4\ mm + 4\ mm$ active volume segmentation was selected as suggested in Fig. 3.1.1. In a

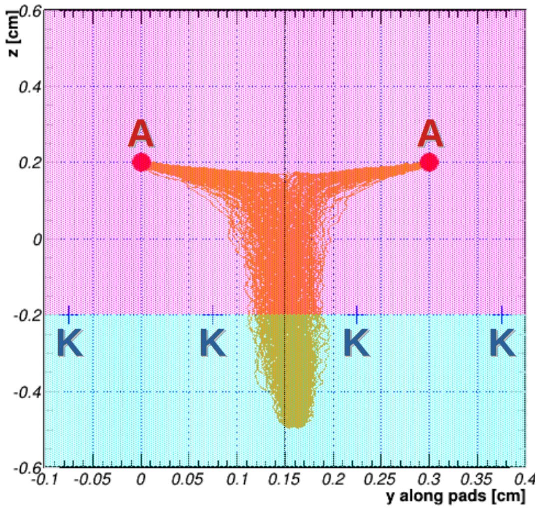

Figure 3.1.1: Basic elements of the TRD-2D MWPC implementation with the anodes marked in red, cathodes with blue crosses, and the amplification and drift regions in magenta and cyan respectively; The formation of an avalanche around two anode wires is tracked via MC simulation of electron trajectories (thin curvy lines) for a TR photon absorption in the gas.

Monte-Carlo (MC) simulation of charge amplification in the TRD-2D ROC, the conversion of a TR photon, interacting close to the boundary of two amplification cells[13] to an electron avalanche is presented. By such calculations based on GARFIELD++ code [30] one has tuned the ROC geometry for gain and charge collection time and fit them to the Front-End Electronics (FEE) signal amplification and shaping time respectively. A detailed collection of time map is calculated for all gas mixtures used in the operation. An example is presented in Fig. 3.1.2 left for a $Xe(80\%)CO_2(20\%)$ gas mixture operated at $U_{anode} = 1.7\ kV$, $U_{drift} = 0.8\ kV$ in a section plane perpendicular to the wire planes. The position of operating wires is also marked on the plot as "A" for the anode wire and "K" for the cathodes. The color code in the figure separates spatial regions of drift time intervals as *e.g.* the whole amplification area, with $0.4 < z_{CBM} < 1.2$, drift times less than 100 ns are expected. For ionization in the drift region we expect 100 $ns < t_{drift} <$ 200 ns while for a narrow band on the boundary of two amplification cells and also close to the drift electrode ($z_{CBM} = 0$ in the figure) the value can exceed such limits. The qualitative dependence

[13] The space centered on an anode wire and operated by two cathode wires.

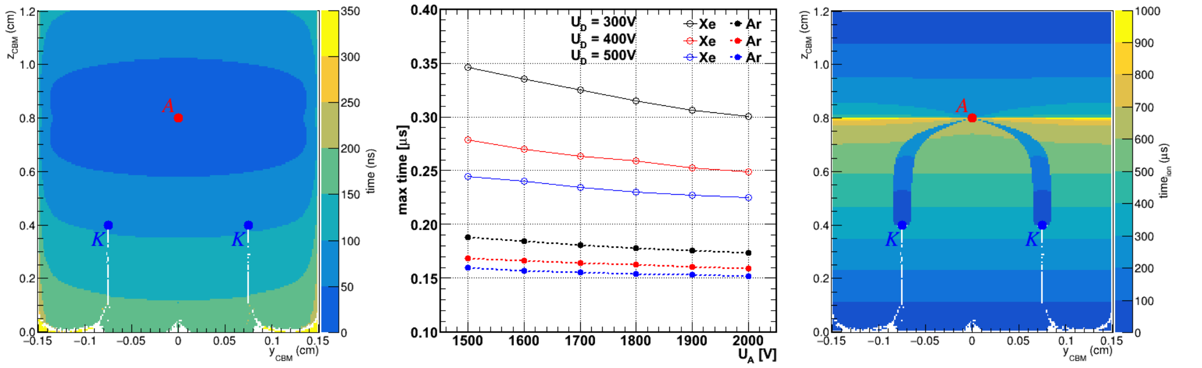

Figure 3.1.2: Timing of the TRD-2D response wrt. signal formation (left) for $Xe(80\%)CO_2(20\%)$ at $U_{anode} = 1.7\ kV$, $U_{drift} = 0.8\ kV$ as a function of the position of the primary ionization inside the amplification cell; the dependence of the maximum drift time as function of active gas, anode and drift voltage (middle) and the collection time of the ions (right) for the same gas parameters as in the left panel.

for the drift time described in Fig. 3.1.2 left is representative for all combinations of $gas/U_a/U_d$. To capture the quantitative variation of the drift time, its maximum value for any configuration is presented in Fig. 3.1.2 middle for 20% CO_2 quencher gas mixed with Xe (open symbols) and Ar (closed symbols). The calculations presented here are instrumental to define the shaping time of the pre-amplifier such that, *e.g.*, TR photons which are mainly absorbed in the drift region (signal formation delayed by more than 100 ns) should be integrated in one hit with the underlying ionization signals which can be prompt (see sect. 3.4).

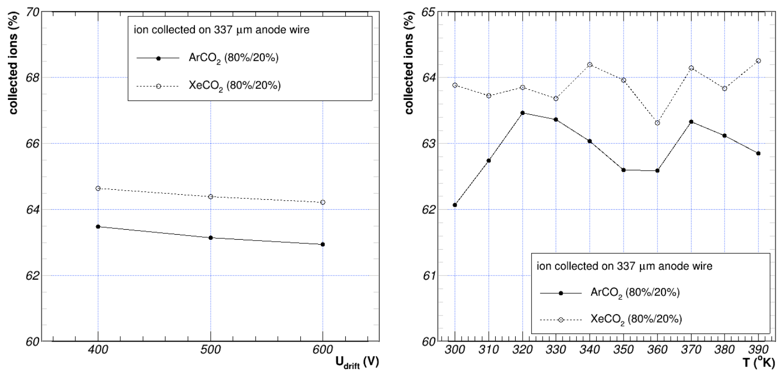

Figure 3.1.3: Percentage of collected ions on a anode wire segment of 337.5 μm (equivalent uniform particles rate of 100 kHz/cm^2) for $Ar(80\%)CO_2(20\%)$ (filled symbols) and $Xe(80\%)CO_2(20\%)$ (open symbols) as function of drift voltage (left) and gas temperature (right).

A secondary feature of the MWPC which has to be realistically considered here due to the high counting rate environments is the collection time of ions produced by gas amplification. Garfield calculations for the TRD-2D ROC geometry operated with $Xe(80\%)CO_2(20\%)$ gas mixture at $U_{anode} = 1.7\ kV$, $U_{drift} = 0.8\ kV$ are presented in Fig. 3.1.2 right for all positions in a section plane perpendicular to wire direction. Contrary to the electronic component which is drained through the anodes, the ions have three electrodes sinks: the cathode wires and the drift and pad planes. Accordingly the ROC volume is divided in three regions as can be seen in the same figure: the upper part of the amplification region collected by the pad plane (I), the region bellow the anode wire plane collected by the drift electrode (II) and the median regions which have the cathodes as sinks (III). From the color code in the figure it is seen that region III has max ion collection times of 300 μs, region I of 400 μs and region II of up to 1 ms. Conversely, the rate at which the amplification cell is completely cooled down is $\approx\ 1\ kHz$. In order to accommodate 100 $particles/cm^2$, the amplification cloud size along the anode wire should be $<\ 337.5\ \mu m$ along the wire direction in order to keep the ROC in a non pile-up operation mode. In Fig. 3.1.3, using the MC simulations of the avalanche and a uniform illumination of the amplification cell, we show the percentage of ions created in the avalanche which are created on a wire span compatible with $10^5\ particles/cm^2/s$ as function of drift voltage (left) and temperature (right). For the U_{drift} dependency we assume normal temperature of $T\ =\ 300\ K$ and U_{anode} uniform in interval $1.4\ -\ 1.7\ kV$ while for the temperature dependency we fixed $U_{anode} = 1.7\ kV$ and $U_{drift} = 0.5\ kV$. From such calculations we see that in general there is a better ion collection for Xe than Ar but still, more than 30% of ions will be not collected when the next particle hits. Nevertheless, the spatial distribution of the remnant positive charge has a minimum at anode when the subsequent particle hits thus not influencing the gain. Some effects should be felt on TR detection (close to the drift electrode) but we assume they are smaller than systematic uncertainties produced by other sources (see section 5.3.2).

3.2 ROC Design and Mechanical Integration (*L.Radulescu, A.Bercuci*)

As it was already mentioned, the mechanical design of the TRD-2D detector was modified wrt the TDR version to optimize:

- the support structure in the inner region of the TRD wall aiming to minimizing the material budget and secondary particle production;

- the services (gas connections and HV cables) such that the full active area of the ROC is used for data read-out (see also section 3.5);

- the mechanical rigidity of ROC both during construction phases and operation by designing an optimal entrance window (see also 5.3.2).

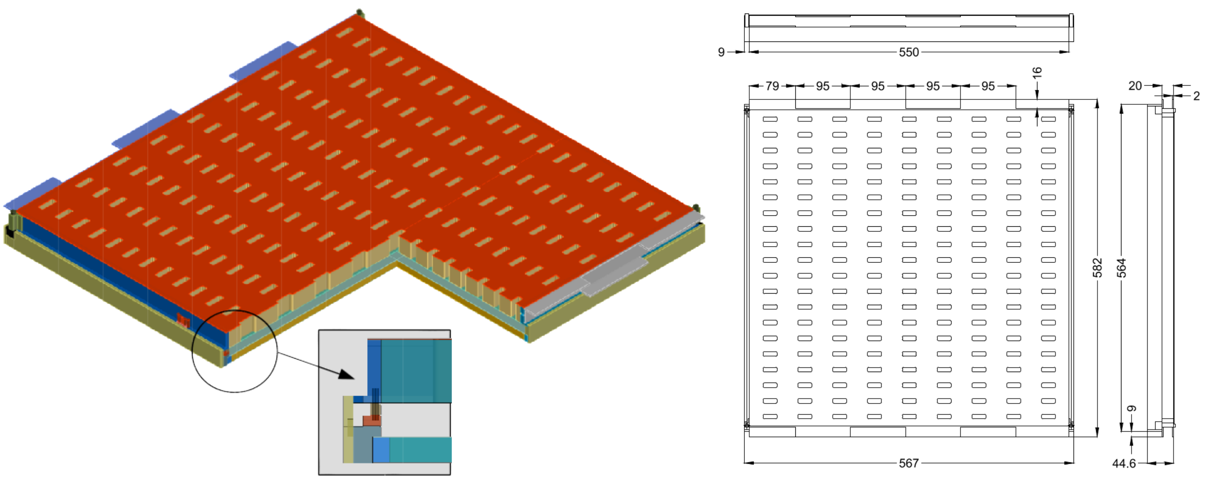

Figure 3.2.1: 3D model of the TRD-2D ROC as seen from the back-panel, also a representative section parallel to the wires direction (left) and technical drawing of the TRD-2D ROC assembly (right).

The design of the ROC according to the requirements from above is presented in Fig. 3.2.1. There are three main components of the chamber which are also instrumental during construction and wall mounting: the entrance window, the active area and the back-panel. The entrance window is a light structure of FR4 reinforced honeycomb (HC) used as alignment frame for chamber assembly (see Fig. 3.2.2 (c)); more details are provided on the next section and also on section 5.3.2 regarding the TR absorption.

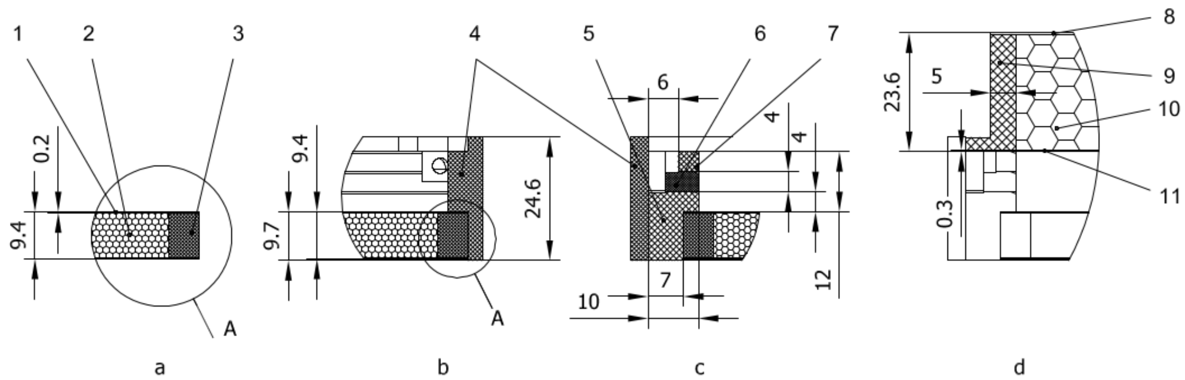

Figure 3.2.2: Structural elements of the ROC wall: entrance window **(a)**, longitudinal ledges **(b)**, wire supporting ledges **(c)** and a detail of the back-panel on top of the ROC **(d)** (see details in Tab. 3.2.1).

The structure holding the active volume is presented in Fig. 3.2.2. There are four ledges on the chamber's wire supporting edge (c) which hold the anode and cathode wires towards gas volume and also generate a logistic space toward the chamber wall for routing HV cables. The spacer ledge is used as interface with the back-panel.

component name	**id in Fig. 3.2.2**	**material**
drift plane support	1/a	C
entrance reinforcement	2/a	HC
entrance window frame	3/a	FR4
chamber wall	4/b, 4/c	FR4
cathode ledge	5/c	FR4
anode ledge	6/c	FR4
spacer ledge	7/c	FR4
grounding screen	8/d	FR4, Cu
back-panel frame	9/d	FR4
back-panel reinforcement	10/d	HC
pad plane	11/d	FR4 diclad 35 μm

Table 3.2.1: List of the TRD-2D components.

The back-panel structure is a layered structure supporting the read-out pad-plane (see section 3.3) towards the active gas and a similar FR4, Cu coated structure towards exterior with flat-cables going-through openings. The 23 mm gap is filled with HC reinforced with FR4 ledges on the boundaries (see Fig. 3.2.2 d). Al supports are mounted on chamber's edge parallel to the wires (see in Fig. 3.2.1 left) in order to connect chambers in a larger structure.

3.2.1 Estimation of entrance window deformation

The entrance window design is of special importance as it has to withstand two mutual contradictory requests: should be thin to transmit the TR photons produced in the radiator but robust to maintain the planarity of the chamber against the pull of the wires during the assembly. The most critical moment for entrance window deformation is after cathode wire installation. The supporting structure, on which the 180 $CuBe$ cathode wires of 80 μm diameter are glued, is

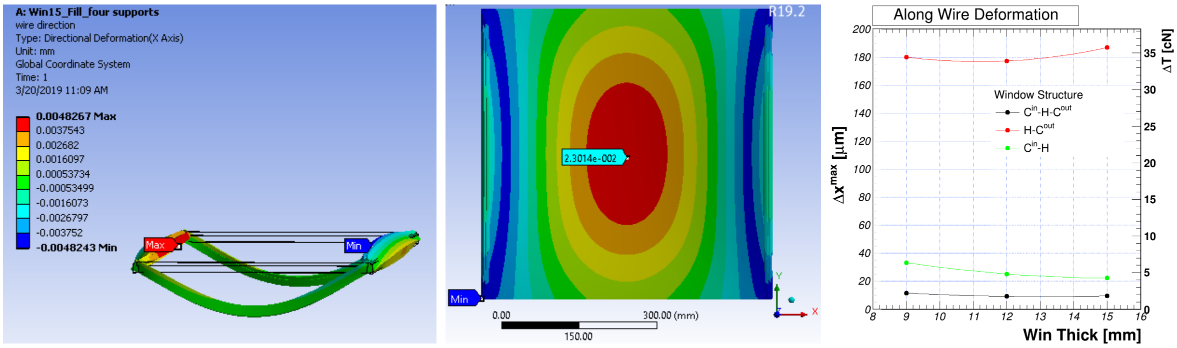

Figure 3.2.3: Deformation of the ROC ledges (left) and the entrance window (middle) induced by the cathode wires pull when glued to the frame and a summary of frame deformation (right) for different entrance window structures according to figure legend.

composed of the entrance window (Fig. 3.2.2 a) on which two ledges are added, the "cathode ledge" and two pushing "chamber wall" ledges (see Tab. 3.2.1). Each wire is tensioned to 100 cN.

In Fig. 3.2.3 the color code encrypt the value of the deformation of the ledges parallel to the wires (left) and "drift plane" perpendicular to it (middle). The values are given in mm and the maximum values are on the level of 2×5 μm for the ledges and 23 μm for the drift electrode. In order to optimize the entrance window design a set of nine structures were tested for three Honneycomb (HC) thicknesses of 9, 12 and 15 mm and three structures with two or one carbon planes towards the drift plane ("in") or/and radiator ("out") according to figure legend (see Fig. 3.2.3 right). As it can be seen from the figure there is little variation for different thicknesses of one window structure but a major difference between the $HC - C^{out}$ and the default $C^{in} - HC - C^{out}$ sandwich. A compromise solution from the structural stability of the chamber which renders the minimum absorption is $C^{in} - HC$. For a Hc thickness of 9 mm a contraction of the chamber along the wires of 30 μm is estimated and a maximum deviation from nominal tension on the cathodes of 7 cN. Such deviations are within the specifications as derived from previous experiences (see production of ALICE TRD). The implications of this strategy on the absorption of the TR photons will be followed elsewhere (see section 5.3.2).

3.2.2 Inner wall integration

In the TRD TDR, it is proposed for the mechanical integration of the modules in the TRD wall a concept of independent units attached to a monolithic support structure. Obviously such a compact and modular design optimizes the installation and maintenance of the TRD system as it skips intermediate integration (e.g. super-module). Additionally to the general support structure concept, for the inner part of the wall, where particle fluxes are the highest, the secondary particle production in the passive material budget becomes an issue, for the TRD system itself but also for downstream systems. It makes sense to look for concepts which rather optimize on the material budget. The TRD-2D ROC was designed based on this optimization criteria as sketched in Fig. 3.2.4.

The Al profiles mounted on two chamber edges (see Fig. 3.2.1) are used to interlock a ROC with an upper and bottom neighbors in a stack structure. A guiding FR4 crossbeam is inserted horizontally between rows of chambers to stabilize the structure. To keep the planarity of the structure, thin Al profiles are inserted as vertical poles, between columns of chambers, locking the FR4 crossbeams on a plane. The assembly works as a brick wall with the back-panel structures of the TRD-2D ROC used to transport the weight from the upper chambers to a support. A reduction of the material budget in the inner regions of the TRD wall from 75.8 $kg/layer$ Al [41] to 11.7 $kg/layer$ Al and 4.3 $kg/layer$ FR4 is thus obtained, with implications to be quantified

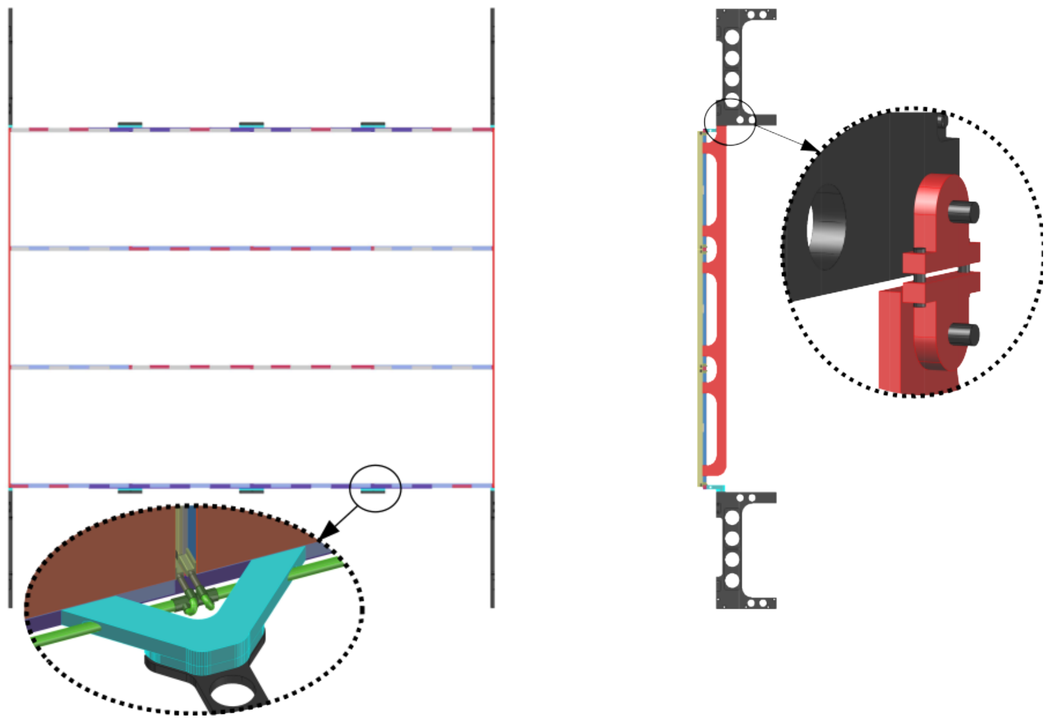

Figure 3.2.4: The supporting structure of ten TRD-2D ROCs for integration in a *super inner-module* by horizontal $FR4$ crossbeams coated with 2 mm thick Al profile with a detail of one bottom support (left plot) and the lateral reinforcement with a detail on the connection lock (right plot).

in secondary particle production.

As consequence of the introduction of the light TRD-2D structure, the original TRD wall support has to be modified such as the weight of the top chambers to be transported to the outer frame through different paths.

In Fig. 3.2.5 two versions of support structures are presented to recover the structural strength (proposed extra posts are marked in blue). In the left panel an intermediate version wrt. the TDR is shown in which some structure is also found behind the TRD-2D modules. A material budget price tag of 22 $kg/layer$ is attached to it [42]. A more radical approach is presented in the right panel where, at the cost of approximately 370 $kg/layer$, an outer crane structure is imagined which pushes the material budget to regions of relatively low particles rates. Detailed simulation of the geometry and its implication on physics observables are in progress.

3.2.3 Inner wall installation and maintenance

As discussed above, the optimization of the mechanical support structure of the inner wall had the consequence of imposing special connection between all 10 ROCs from a layer. The structure thus formed, is light and not self supporting. Therefore, we have to rely on additional structures for assembling it, transporting to the experimental hall and inserting it in the TRD frame. For these operations we are proposing two devices: *the mounting frame* and *the mounting table*

The mounting frame, sketched in Fig. 3.2.6 left, is a rigid structure, supporting one inner-supermodule, horizontally and vertically. It is used in the installation phase to precisely align the ROCs wrt. each other, to transport them to the experimental hall and to insert them in the TRD frame. In the maintenance phase it is used to extract the inner-supermodule from the frame and transport to the maintenance area.

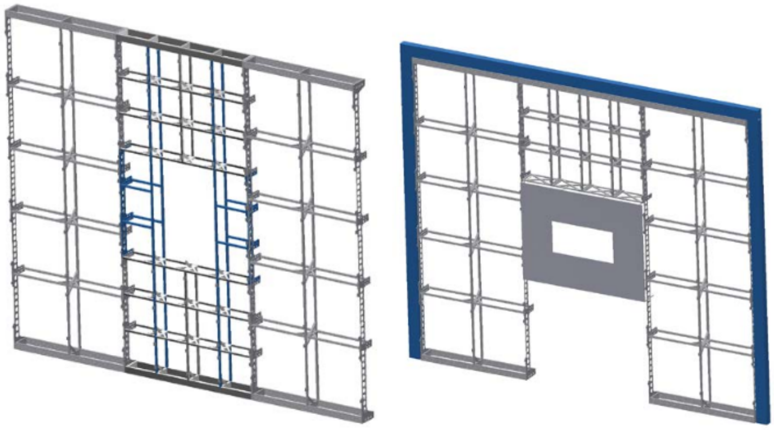

Figure 3.2.5: Two possible scenarios (see blue beams) proposed here [42] for reinforcing the central part of the TRD wall due to the new light structure in the present proposal.

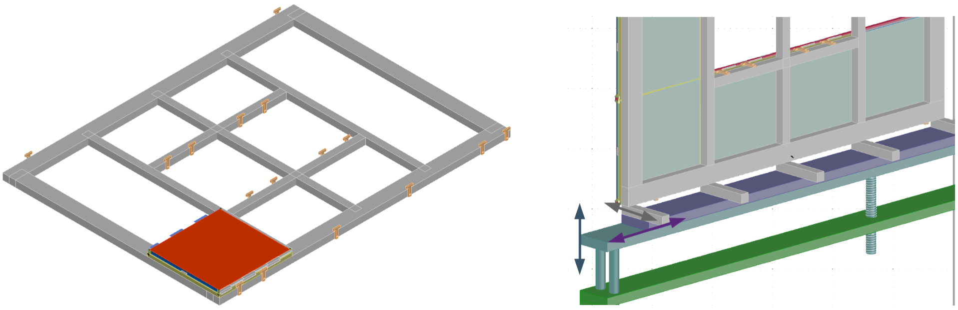

Figure 3.2.6: The mounting devices for installation and maintenance work of the TRD-2D system; *the mounting frame* (left) used to assemble and keep in position the inner-supermodule structure outside the experimental setup and a detail of *the mounting table* (right) used to insert it in the TRD frame.

The mounting table, shown in Fig. 3.2.6 right, is a device which can be attached to the TRD outer-frame and it offers three translations as it is suggested in the figure by the arrows. The device is used to hold the mounting frame in front of the TRD inner-frame and align it wrt a target and support it until the TRD-2D structure is secured in the inner-frame.

Since the installation/maintenance of the TRD-2D inner region has to be performed independent of the installation of the radiators for the outer ROCs the only possibility is to insert it from the front of the wall. This extra requirement implies that the total outer frame has to be enlarged by ≈ 120 *cm* to allow a larger opening of the inner frame and fully exposure of the inner region. Such modifications of the TRD frame may be also suggested by moving the regions of high secondary production from the frames out of the ToF acceptance. Such calculations are in progress, in order to fully estimate the modifications required on the supporting structure by the integration of TRD-2D system in respect to other sources.

3.3 Pad Plane Design and ROC Assembly (*A.Bercuci, D. Bartos, L.Radulescu)*

The main difference relative to the TDR design of the TRD system, which is proposed here, is the granularity of the signal read-out which implies a change of the pad-plane topology.

The present arhitecture is based on a triangular geometry of the pads as can be followed in Fig. 3.3.1 right. In order to keep the number of FEE read-out channels/module constant for the same charge sharing between pads the height of pad-rows was increased to 27 *mm* for a pad width of 7.5 *mm* thus yielding an effective read-out area/channel of 1 cm^2.

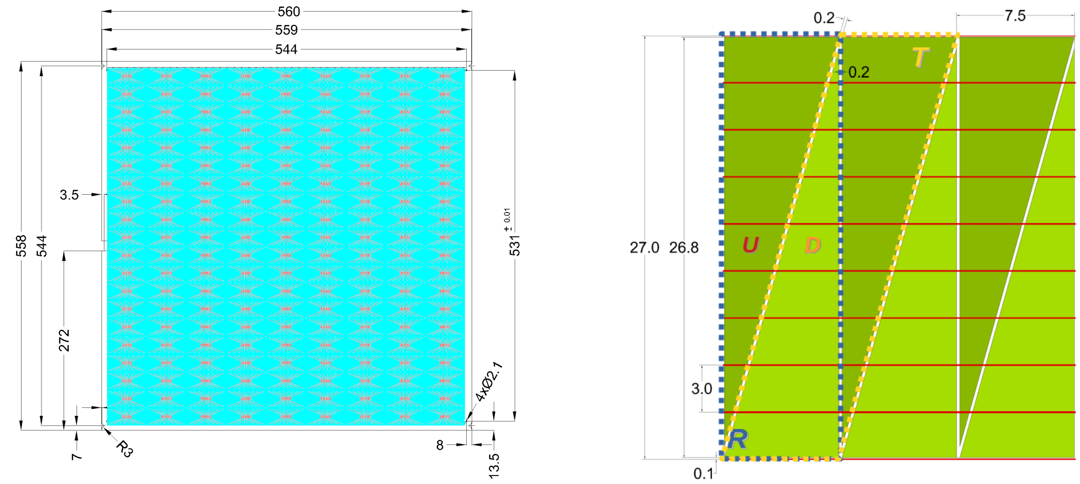

Figure 3.3.1: The TRD-2D pad-plane overview; dimensions and the pad-to-FEE connectors on the back of the plane (left) and a sketch of the pads towards the active volume wrt. anode wires marked in red (right).

In Fig. 3.3.1 the main components of the pad-plane design are presented. In the left panel an overview of the plane seen from the FEE side is presented, where all connectors, each of 16 channels, are depicted together with their traces to the pads. A total of 20 *rows* $\times$ 9 *columns* connectors adding up to 2880 independent FEE channels are used to read-out a TRD-2D module. The pad-plane sized of little less than $600 \times 600\ mm^2$, is realized of 300 μm thick FR4 plane with Cu imprints of 35 μm on both sides. The pads, towards the active area, are of triangular shape as seen in Fig. 3.3.1 right with alternating orientation, up (U) - light gray in figure, and down (D) respectively. It is of paramount importance for the quality of the TRD-2D signals to have no variation of S/N along the pad length and thus one has to introduce pad pairing to realize this condition. The traces from pads to connectors are rooted such that consecutive entries are mapped to triangular pads in the following order $U - D - U - ..$, allowing for two types of parring of the pads: the rectangular pairing (R) of type $U - D$ and tilt pairing (T) of type $D - U$. The real novelty of the design consists of the fact that it allows recording of the signals with both types of pad shapes (R and T) *in the same time*, effectively providing a twofold coverage of the active area. It is obvious that the type of read-out pairing described above can not be achieved with passive circuitry and thus it require a specific FEE ASIC. Moreover, the pad pairing constrain exceeds the domain of one connector, and thus it impose another design request on the ASIC, the CHIP-CHIP signal pairing, in fact, an ANALOG communication of nA currents of MHz frequencies over distances of 6 cm. The *Fast Analog Signal Processor* (FASP) (see section 4.1) which implements all these requests is thus an integral part of the pad-plane design and consequently of the TRD-2D.

The size of the pads is yet another parameter of the detector which defines on one hand the input capacitance (25 nF for the geometry of active area considered) for the ASIC but which is in turn defined by the anode wire pitch; the condition for the length is $L = n \times d$ where d is the anode wire pitch and n is an integer. Such condition is instrumental for the anode wire identification capability of the TRD-2D - a unique feature of the design discussed in section 5.2. Additionally there is a strict alignment constrain between the anode wire electrode and the pad-plane such that for each pad-row there are two anode wires which are on its upper and bottom boundaries. This requirement is translated in the mechanical precision at which the alignment pins have to be realized (see details in Fig. 3.3.1 left) both on the pad-plane itself but also on the chamber ledges.

Last but not least the pad-plane is the top cover of the active volume and the mechanical connection between the ROC frame and the back-panel. As such it has to be leak tight and mechanical rigid. The gas can leak through pin-through in the FR4 material where pads are connected to imprinted traces and plane edges where connected to the ROC frame. We have addressed these requests by designing the ROC frame such as to provide a twofold connection with the pad-plane as seen in Fig. 3.2.2 left. Thus, the pad-plane is supported by both the "space ledge" and the "chamber wall" (see Tab. 3.2.1) on two edges respectively by the "push ledge" and the "chamber wall" on the perpendicular direction (see Fig. 3.2.2 middle). A special care has to be devoted during ROC assembly to the filling of the pin-through with glue and consequently gluing the HC to avoid gas leaks through the flat-cable openings in the back-panel.

3.4 Front End Boards (*C. Schiaua, A.Bercuci)*

Supported on the back-panel of the TRD module are the *Front End Boards* (FEB) which are housing the *Front End Electronics* (FEE). There are several layers of the FEE which have to be installed near the ROC as follows:

- The FEE analog ASIC dealing with first stage amplification of the signal
- The first digital level responsible for analog to digital conversion
- The second digital level for data serialization and formatting
- The data transport layer

The design strategy of the whole FEE chain for the TRD-2D system, was to build and test independently each of these components, in order to optimize debugging. Another argument for a late integration was the need to align to the electronics market dynamics on which improvements and price drops can be fast over the development time span of our chain. Therefore here we are presenting the building blocks of the FEE chain operating the TRD-2D, the final realization being pushed as close as possible to the moment of module mass production to maximum benefit from the electronics market dynamics. A direct consequence of our strategy is a relatively low integration at present of our chain which occupies three layers of FEBs. The final goal is to use only one layer. In the following the FEBs, as they are now configured, will be presented and the target integration will be emphasized.

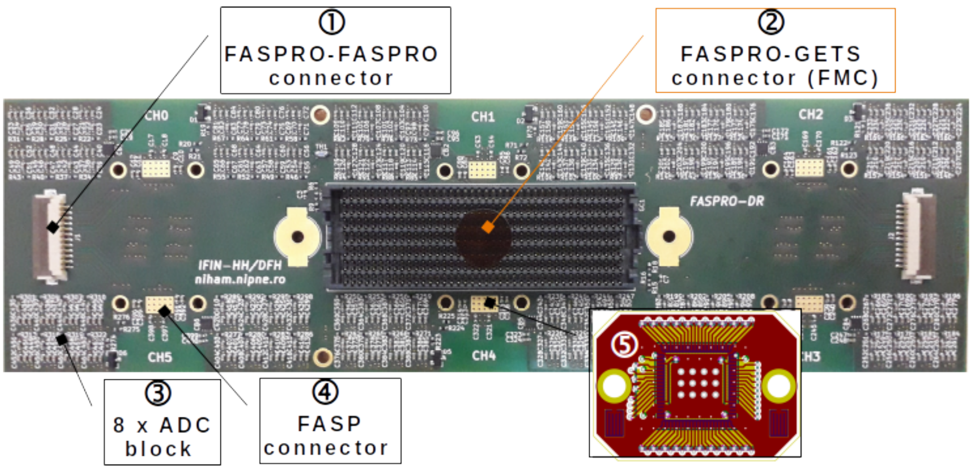

Figure 3.4.1: The FASPRO board housing six FASP chips and the ADC digital layer; the main building blocks on the board are indicated in the figure.

The main FEB housing the FASP ASIC is the *FASPRO* (FASP Read-Out) board presented in Fig. 3.4.1. The board of $180 \times 54\ mm^2$ covers almost entirely the active region operated by the 6 FASPs which are mounted on it. It is build on 10 layers having a thickness of 1.8 mm. The FASPs are organized on a 2×3 grid servicing 2 pad rows. Communication between FASPs on the same board is assured while for neighboring boards two connectors (①) are foreseen to connect neighboring FASPs on different boards. A total of 3×10 boards are needed to operate one TRD-2D chamber. A large space in the current design is used for each FASP as it comprise a compression connector ZA1-10-2 with 100 pins (④) and two batteries of 8 times single channel ADC (③). In order to keep the design flexible the FASP ASIC was not yet BGA encapsulated but rather bonded to a board (⑤). The board, tagged $FASP03B-v5$, is an asymmetric board with 6 layers for which a priority was the isolation of input traces. A massive ASP connector (②) completes the design for connection with the second FEB for digital processing. For the final design the following changes are foreseen: replace the FASP bonding board with a BGA encapsulation, replace the 16 single channel ADC with one 16 channel ADC and remove the ASP connector. Thus there will be enough room on the board to install the digital processor and the transporter chips.

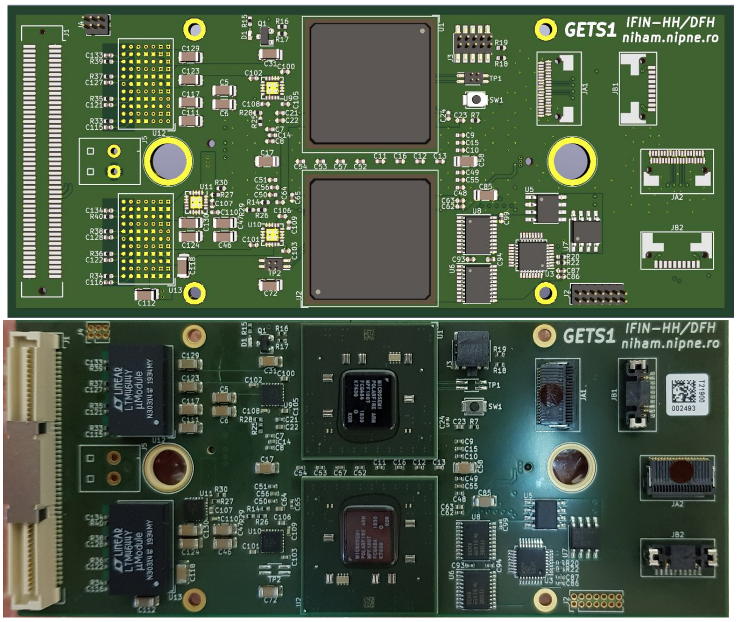

Figure 3.4.2: The GETS board housing the second layer of digital processing responsible for data formatting and serialization; design (top) and realization (bottom).

The second FEB involved in TRD-2D read-out is the *Generic Event Time-stamping Streamer* (GETS) board. As the free-running DAQ need a elaborated digital component, we select a development board to connect the FASP ASIC to the CBM experimental acquisition. Of paramount importance is the timing of the two ends of the DAQ chain such that the time information generated on the analog part should be transported unchanged and synchronous for all FEE channels. This implies having the digital part close by the FASP ASIC and flexible enough to afford fast development and adjustment. The solution offered by *Field-Programmable Gate Array* (FPGA) is optimal for our requirements. Unfortunately the common FPGA (of the "RAM" type) are sensitive to radiation fields and does not offer a practical solution for operating the TRD-2D in realistic environments. Luckily, in the years 2017-2018, a new family of FPGA was launched by Microsemi, the PolarFire [43]. It is build using SONOS "FLASH-type" technology which intrinsically is more resilient to radiation than the "RAM" technology. As time past, more and more data become available wrt. the good behavior of this chip in radiation ([44] [45] [46]). For the final version of the FEE we consider both strategies for the digital part, namely freezing the development to an ASIC in the UMC180 technology or keeping the further the flexibility of the PolarFire FPGA near the detector.

The GETS board includes two $PolarFire^{TM}$ MPF100 FPGAs, one 560-pins ASP connector towards the analog board FASPRO, a *Bergstack* connector for further extensions, two connectors for high speed $FireFly^{TM}$ transfer modules, one (low-speed) multichannel ADC, two (low-speed) DAC chips, commuting and linear DC-DC sources for powering itself as well as the FASPRO board. A set of auxiliary circuitry are also present for potential DCS tasks. The board is implemented on 14 layers PCB with a thickness of 2.0 mm. Programming of the FPGAs is performed via a dedicated JTAG adapter for lack of space.

The connection to the CBM DAQ chain is done for the moment based on a 3^{rd} layer of FEBs, a board developed by the collaboration, the C-ROB [47] board. It contains three GBTx ASICs as well as the associated optical interface modules. This components were developed by CERN for high energy physics applications and used by all other detection systems of the CBM experiment. For cost optimization in the R&D period we select SATA cables and consequently add some passive connectors from this technology to the FMC entry point on the C-ROB. The final version of the FEB will contain also the GBTx ASICs bonded on it.

3.4.1 Material budget of the TRD-2D module

As described before (see section 3.2), one of the main criteria used to re-design the inner part of the TRD wall was to further minimize the material budget in areas of highest particle multiplicity and rates. To quantify the result, our design was converted into GEANT geometry with maximum accuracy and checked as percentage of radiation length X_0. Unfortunately, the main contributors, the FEBs system and the general support structure are not yet in their final version, but nevertheless estimations are possible for the target design. The FEE, following a conclusive redesign (see section 3.4), will be mounted on only one FEB, parallel to ROC backpanel, of yet undefined thickness while the TRD wall supporting structure still need GEANT implementation and systematic evaluation of all technical possibilities put forward in section 3.2.2.

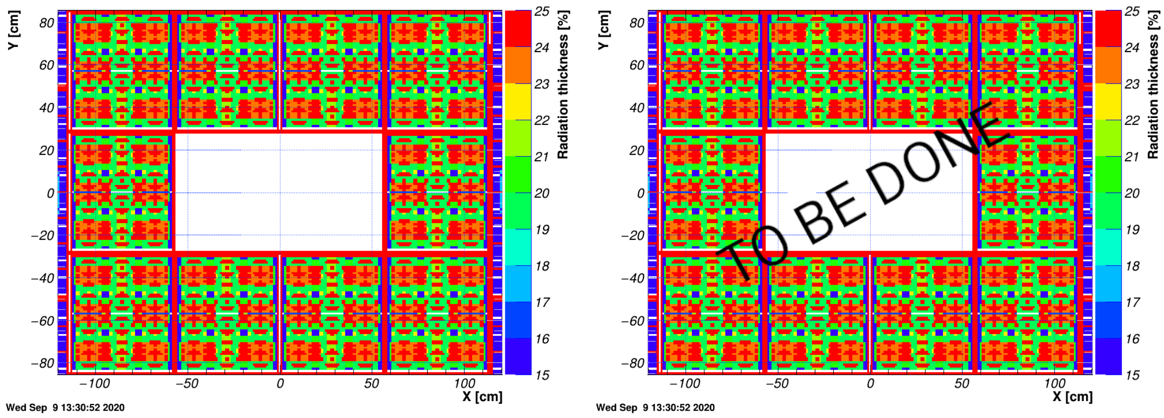

Figure 3.4.3: The material budget expressed in percentage of radiation length X_0 for the TRD-2D module (left) and the same quantity without the FEB contribution (right).

An estimation of the current material budget of the TRD-2D system including the current status of FEB is presented in Fig. 3.4.3 left. On the right panel the same structure is presented for the target geometry with only one layer. The support structure proposed for the TRD-2D is implemented for both scenario from Fig. 3.4.3.

The material budget introduced by the supporting structure is best seen in the amount of secondary hits produced in the next downstream detector, the ToF.

3.5 Gas System Integration (*A.Bercuci, D. Bonaventura)*

The gas distribution system of the TRD detector is designed to have 5 independent feeding lines for each station. Each of the input lines feeds a daisy chain of 12 chambers as presented in

Fig. 3.5.1. The constrain of each feeding line is to have a pressure difference between inlets and outlets of same height less than 0.05 *mbar* to assure a deformation of the entrance window of the TDR prototype within specs (see ref TDR).

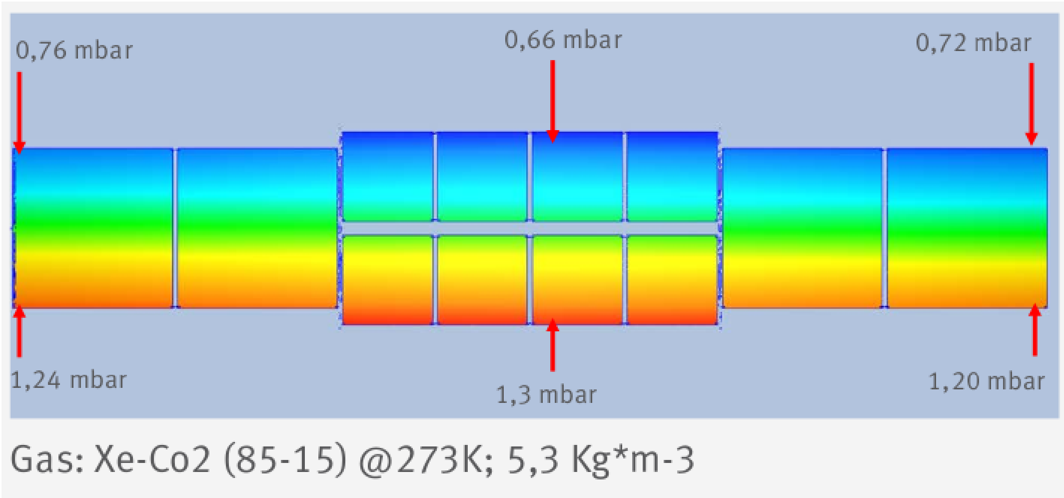

Figure 3.5.1: The differential pressure of the gas flow for normal operation of one daisy chain, in the current TDR.

In Fig. 3.5.1 it is presented a standard case of flushing $XeCO_2$ at 15 l/h and normal temperature. It is observed that the pressure gradient is independent of the flow (left to right in the figure) but it has a gravitational component of ≈ 0.5 *mbar* which is due to a gradient in the gas concentration, the Xe being heavier tends to accumulate on the bottom of the ROC. The *pressure difference constrain* illustrated in Fig. 3.5.1 has been obtained by selecting 8 *cm* inlet/outlet inner diameters and placing them directly on the active area.

The TRD-2D chambers have a rigid entrance window wrt. the TDR design and therefore is not subject to such constrains. On the other hand, to simplify the design of the whole gas system, we select to daisy chain the TRD-2D ROCs within the same design but we didn't drop the requirement of having the inlet and outlet pipes totally included in the service area (see Fig. 3.2.2 (a)).

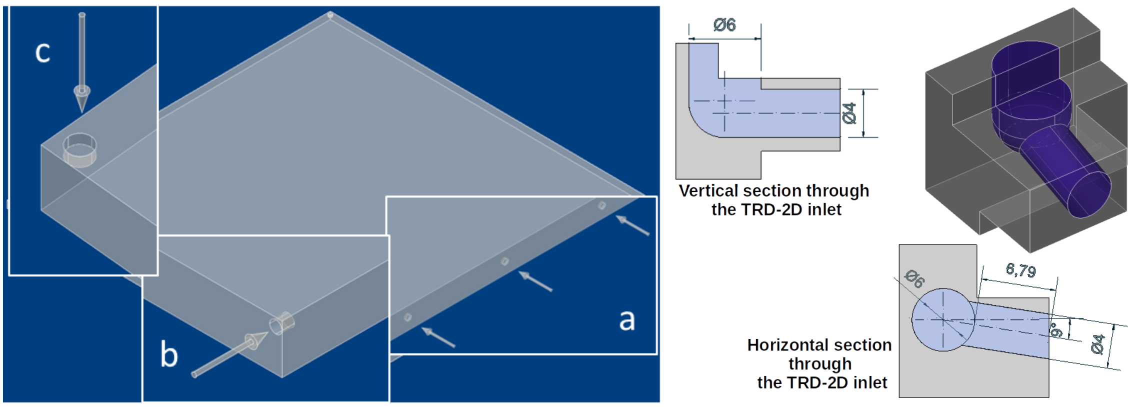

Figure 3.5.2: Inlet/outlet strategies for the TRD-2D prototype (left) and the selected solution (right); the *TRD-2D inlet box* implementation with a vertical and horizontal wrt ROC plane cross-sections.

We have studied several strategies for the inlet/outlet position and numbers, as shown in Fig. 3.5.2 left, in order to optimize the uniformity of the gas flow inside the ROC. The solution marked as **a)** represent a distribution of gas with 20 gas inlets and outlets distributed on the ROC edge parallel with the wires; solution **b)** is with 2 gas inlets and outlets at the corners of the ROC, blowing the gas parallel with the wire plane, and the last, **c)**, is the TDR solution. Based on flow simulations [48] we select the solution **b)** which represent a compromise between the distributed flow solution with very difficult mechanical implementation (**a)**) and the TDR version which penetrates through the pad-plane. A vertical and horizontal cross-sections of the *"inlet/outlet box"* which fulfills the above conditions are presented in Fig. 3.5.2. The inner diameter of the pipe entering the TRD-2D ROC is 4 mm. In order to have a similar flow section for the inner region as for the TDR version a gas distribution line has to be inserted such that the input 100.5 mm^2 total pipe section is distributed to 4 TRD-2D ROCs and also accommodate the pressure differences in the distributor and extra pipes. Thus the strategy would be to connect the top/bottom 4 of the inner ROCs of one TRD station to one daisy chain and keep the middle two TRD-2D for a third. This distribution, not optimal from the point of view of flow resistance, is nevertheless dictated by the constrain on the maximum difference in vertical direction between two lines of small chambers (see Fig. 3.5.1).

Feeding the gas through the top inlets via a distributor has two benefits:

- ensure similar gas properties (O_2 contamination etc.) for all chambers thus uniform gain.

- improve the gas flow uniformity in the chamber by using the the gravitational pull of the heavy Xe. Simulations of the gas flow have shown that for lateral inlets there is no directional flow inside the chamber and thus areas of various gas exchange rates are possible with consequences to the gain uniformity.

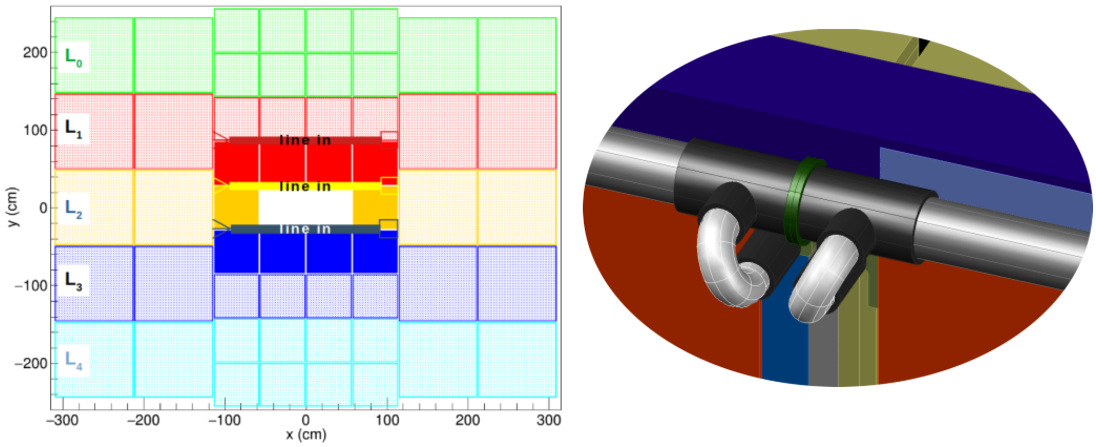

Figure 3.5.3: A sketch of the gas distribution system (left) for one TRD station and the connection of the TRD-2D inlets to the distribution line used to link the TRD-2D ROCs in the predefined gas distribution system from TDR (right).

A sketch of the gas distribution system including TRD-2D chambers is presented in Fig. 3.5.3 left. Out of the five feeding lines allocated per station, two, namely L_0 and L_4 are of the TDR type while L_1, L_2 and L_3 are modified. Each modified feed contain two distribution lines (*"line in"* in figure and "line out", parallel to it, not shown) used to adapt the flow impedance of 4 TRD-2D ROCs to the flow resistance of a TDR gas feed line. For each modified feeding line, the gas is distributed to the TRD-2D ROCs from the top two inlets and exhausted on the bottom outlets, thus the line terminators (rectangular open symbols) in the figure. The connection from the distribution line to individual chamber inlets is sketched in Fig. 3.5.3 right for two adjacent ROCs (marked 1 and 2). The distribution line (gray in figure) is a stainless steel pipe of 12 mm diameter, mounted on top of the wall connectors (see section 3.2). The connection to the ROC inlet/outlet is realized with industrial Tees and Couplings (black in figure) through a stainless steel pipe of 6 mm diameter. The distribution pipe is terminated towards the input with a tee for accepting two connections from upstream large chambers and a termination cap at the opposite end. A similar structure is realized also for the exhausting distribution pipe which transport the gas from the 4 TRD-2D ROCs to the downstream large ROCs.

An alternative to the gas flow scheme presented above, which considers also the difference in elasticity of the two TRD ROC designs, would be an independent feed line (L_5) for the 10 inner chambers. The advantage of such design would be a total separation of ROCs but, besides increasing the costs of the gas system, it would allow only a flow rate of 15 l/h for all 10 TRD-2D ROCs which is rather small wrt the ionization rate (see below) compared to outer modules.

The TRD operation depends on the gas quencher (CO_2) to absorb fluorescence photons produced in the working gas. A potential production of O_2 is associated with the dissociation of the CO_2 molecule in high particle rates. Such processes, more abundant in the inner chambers of the TRD wall, are hard to quantify in laboratory measurements, but qualitatively they tend to build the concentration of O_2 along a daisy chain and tend to form conductive C deposits with the possibility to generate electrical sparks. Thus a possible draw-back of the system presented in Fig. 3.5.3 left, not related to the TRD-2D gas flow design, is a gain variation decreasing from left to right in the figure, associated with electrons attachment. A parallel gas feeding alleviates somewhat such problems.

3.5.1 Systematic effects on the TRD observables induced by gas flow set-up

The gas system of the TRD detector is a complicated mechanical system composed, essentially, of storage volumes connected by pipes. One can analyze such system using an electromagnetic analogy of capacitance/inductance replacing the *gas storage/flow resistance* pair. In an electromagnetic system, the appearance of resonances is well established for certain frequencies of the input signal. A similar question has to be answered in the case of the TRD gas system in the presence of pressure gradients. The effect can be visualized by heavy ionization.

We have performed several long-term tests of the full TRD-2D detection chain, in laboratory conditions, in order to observe such resonances and estimate their influence on the TRD observables. In Fig. 3.5.4-top such an experiment is described, by presenting the time monitoring of three main parameters of the system: the cluster rate (black), the anode current (red) and the drift current respectively (blue). The TRD module is operated for more than 40 *min* under changing external conditions. The list of modifications are presented in figure and also summarized in the Tab. 3.5.1 together with the moment of their implementation.

Table 3.5.1: The list of actions on the TRD-2D system and their time of application as shown in Fig. 3.5.4.

id	time	operation
1	13:41	Acquisition Started
2	13:43	Pulser set at 1 Hz
3	13:43	Pulser set at 100 kHz
4	13:43	Pulser set at 100 Hz
5	13:45	*Start X-rays* tube @ $I_X = 20.4\mu A$ $U_X = 15kV$
6	13:50	*Stop X-rays* tube
7	13:51	Pulser stopped
8	13:56	Oxygen meter started
9	14:01	**Gas flow stopped**; Oxygen meter stopped ($\approx$ 100 ppm)
10	14:02	*Start X-rays* tube @ $I_X = 20.4\mu A$ $U_X = 15kV$

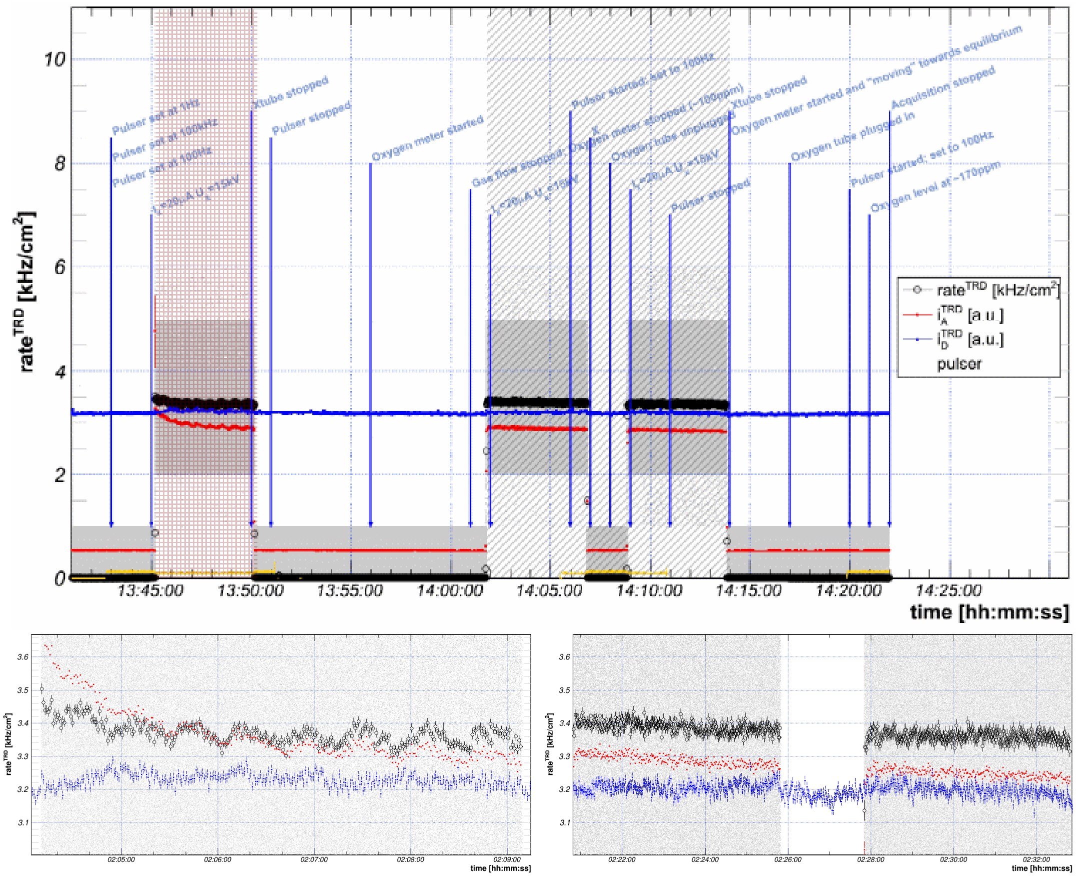

Figure 3.5.4: Time monitoring of reconstructed particle rate and currents in the TRD-2D detector over a period of $\approx$ 40 min during which the detector is exposed to varying conditions of irradiation and gas flow (top) according to labels in figure and list in Tab. 3.5.1; a zoom on the detector behavior for gas flow **ON** (bottom left) and for gas flow **OFF** (bottom right) is also shown.

11	14:06	Pulser started; set to 100 Hz
12	14:07	*Stop X-rays* tube
13	14:08	Oxygen meter stopped
14	14:09	*Start X-rays* tube @ $I_X = 20.4\mu A$ $U_X = 15kV$
15	14:11	Pulser stopped
16	14:14	*Stop X-rays* tube
17	14:14	Oxygen meter started and "moving" towards equilibrium
18	14:17	**Gas flow started**
19	14:20	Pulser started; set to 100 Hz
20	14:21	Oxygen level at 170 ppm
21	14:22	Acquisition stopped

The irradiation of the module is done with an X-rays tube operated at $I_X = 20.4\mu A$ and $U_X = 15kV$ on a Au target. The currents in the MWPC are on the level of $I_A = 0.80\ \mu A$ and $I_D = 0.34\ \mu A$. The irradiation is done in three bunches of 5 min: $id : 5-6$, $id : 10-12$ and $id : 14-16$ respectively according to Tab. 3.5.1. For the first irradiation the flow of $ArCO_2$ of 80%/20% is at the nominal value of 6 l/h and it is stopped @$id : 9$ for the last two irradiations. During the whole time of the experiment the currents in the module are monitored synchronously with the data. A full reconstruction is performed on the free-running acquisition (see section 5.2) and the cluster rate is calculated on a one second interval. Values of $\approx$ 3.4 kHz/cm^2 photons are reconstructed which show that the system was not stressed, such values being far from the nominal operation (100 kHz/cm^2). The behavior of the TRD-2D under irradiation for the two conditions of gas flow is zoomed in the bottom of Fig. 3.5.4 with a slight offsetting of I_A for a better comparison with the data. The O_2 contamination for the first irradiation is constant at a value of 100 *ppm* while for the next two, with the gas flow stopped, it increases linearly with time, to less than 170 *ppm* over $\approx$ 16 *min*. Although the parameters of the irradiation system (X-rays tube) are the same in all three cases the response is rather different wrt. the two flow cases. For the continuous flowing of the gas (Fig. 3.5.4 bottom; the nominal conditions of the flow system) the anode current shows two systematic features: a power-law drop in time proportional to $t^{-\tau}$, $\tau = 0.035$ and a repetitive pattern with a frequency of $\approx$ $30mHz$. In the case of no gas flow the anode current shows a linear drop but no periodic structure.

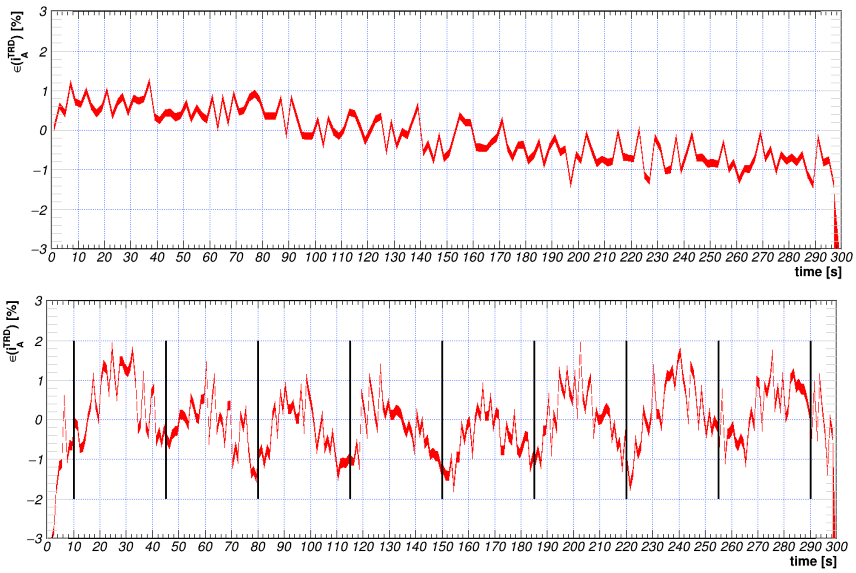

Figure 3.5.5: Behavior of the anode current for TRD irradiation with no gas flow (top) and the anode current oscillations (bottom); the current is normalized to the mean and the power-law value respectively; the periodic structure from the bottom plot is emphasized by the vertical lines spaced by 35 s.

The anode current oscillation for the flow **ON** condition are presented in Fig. 3.5.5 bottom, emphasized by the subtraction of the power-law time dependence and represented in percentage of this value. The pattern shows a drop of $\approx$ 3% over $25 - 30$ s followed by a rapid recovery. On the top plot of Fig. 3.5.5 the situation is presented for flow **OFF** condition. Here a variation of 2 % is recorded over a 5 *min* time interval, mainly due to increased attachment in the gas due to increasing O_2 contamination. From the time constants of the two dependencies of the TRD-2D system wrt. gas flow, one can clearly conclude that the oscillatory pattern is NOT to the *e.g.* O_2 impurities entering the system between controller cycles.

Another view on such phenomenon is summarized in the time dependence of the reconstructed cluster rate from Fig. 3.5.4 clearly seen in the bottom plots for the two gas flow cases. While for the flow condition **ON** (left), the rate clearly follows the variations of the anode current with relative less accuracy, the condition of flow **OFF** shows a flat behavior of a somewhat decreasing trend. The incident photon flux being constant (X-rays tube parameters are monitored to be constant during irradiation) and also FEE chain being unchanged (monitored by the pulser signal - see Tab. 3.5.1 and also discussions on the calibration section) the observed variation in rate is related to variation in the gas gain only. The only conceivable way to have gain variations of such large amplitudes is through pressure variations, related to the mechanics of the gas system, propagated in a resonant way by the particular design of the gas system: storage/flow resistance combinations. For the current experimental setup the gas system was very simple as it was composed of two bottles of high pressure Ar and CO_2 and a gas mixing station of a commercial type. To exclude the hypothesis of malfunctioning in the mixing station we have tested two products of totally different design (mechanical/digital controlled) without observing differences[14].

We have shown in this section that at higher rates of particles, the gas resonances which are natural in (large) gas systems start to be observed in the reconstructed data[15]. It is our conviction that avoiding such effects is beyond the tasks of the gas system designers, which left only the possibility to monitor and calibrate out such effects. A simple application of such a technique will be described when discussing the TRD-2D energy resolution in section 5.3.2.

3.5.2 Gas effects in high dose environments

The gas composition used to operate the TRD is either $XeCO_2$ with better TR absorption and higher operating costs or $ArCO_2$ for tracking applications. In both cases, the addition of CO_2 ($\approx 15-20$ % volumetric amount) is used as gas *quencher* to absorb fluorescence photons emitted by radiative de-excitation of the working gas. On high radiation intensity fields the dissociation of the quencher molecule is increased producing free C and O radicals. The oxygen content decrease the gas gain by increased electron attachment while the carbon will settle down on the bottom of the detector. Such carbon deposits and some times carbon chains will be produced more copiously around chamber outlets as they get driven by the gas flow. In the current design of gas connectors (Fig. 3.5.2 right) the gas pipe entering the ROC volume is tangent to the chamber wall (see Fig. 3.2.2 (b) and details in Tab. 3.2.1). For a vertical positioning of the chamber the accumulation of C ash will tend to clog up the low sitting connectors acting as gas outlets, with implications in gas flow and pressure distribution. In order to alleviate such effect one possibility would be to carve a few mm groove into the chamber wall (item 4/b in Fig. 3.2.2) used as ash collector. Other alternatives will be investigated during detailed studies of gas aging.

[14]In the experiment we also tested the O_2 sensors which are inserted in the gas system in order to exclude influences on their side (see Tab. 3.5.1 $id: 8, 9, 13$)

[15]The variation in the energy of the clusters with the gas flow was not discussed here but it was also observed during tests (see also section 5.3.2).

4 The TRD-2D Front-End-Electronics

In section 3.3, together with the pad-plane topology, we introduced also a feature of the TRD-2D *Front End Electronics* (FEE) which defines the functionality of the detector, namely the pairing of the input signals. Their time distribution was discussed in section 3.1 and we have emphasized on the TR timing. In section 3.4 we discussed the different layers of FEE processing with emphasize on the geometrical organization and material budget. Here we will reiterate the same topic, this time presenting the signal processing and timing.

We will start with a short description of FEE challenges in a free-running experiment where, each Read-Out Unit (ROU) is hardware independent from the rest. For triggered experiments Data AQuisition (DAQ) is based on digital signaling each *detection component* in the experiment. Here, additionally, there is an extra data layer of "time", which is the common interface, for all ROU in the experiment. It is thus self-understood that a new, non-hardware-trigger-type experimental component, namely the Time Fast-Control (TFC), which keeps all ROU synchronized, is now mandatory. Also, for the DAQ-type experimental components, such as the TRD, the integration with the TFC becomes of paramount importance for its operation.

Besides the strict synchronous timing of the "signals" the TRD FEE has to be fast. *E.g.* for an average 100 kHz/cm^2 particle rate, with the average cluster size (see section 5.2) of 7 ROU (each ROU is connected to a 1 cm^2 triangular pad) per particle, a processing speed of minimum 700 kHz is requested on the ROU. Taking into account also more complicated signal topologies (*row-cross clusters* see section 5.2) and statistical particle rate variations around the mean, a 1 MHz signal processing speed is needed. We have demonstrated, that the signal collection time only, is on the level of 300 ns (see Fig. 3.1.2), especially for the TR photons. Thus the time left for first level digitization and processing is less than 700 ns. Obviously, second level digitization and synchronization has to happen parallel and thus needs considerably elaborated electronics and FIFOs.

The TRD signals are used to build two types of observables; *extensive*, e.g. the energy deposit (see section 5.3.2) and *intensive*, the position of the particle (see section 5.3.3) in the detector volume. For the observables of the first type, the absolute value of the signal does matter while for the second not, as only their relative ration is used. In the case of energy measurement, a solid reference (electronic baseline) is mandatory. The effects which are modifying the baseline are: signal tails of $\approx$ 400 μs from ions drifting toward the pad-plane (see Fig. 3.1.2 left) which depend on particle rate, the short time span between consecutive signals (see above less than 700 ns) in which signal processing and also baseline restoration has to happen in parallel and last but not least electronic response to exceptionally large input signals (*e.g.* particle pile-ups, ions, etc.) outside the dynamic range.

Last on the list of challenges for a FEE operating the TRD-2D in the CBM experiment is the data volume/ROU. It is obvious that the global synchronization of the experiment happen in a delayed phase and a remote position wrt signal measurement. Therefore we need to transport the data away from the detector, without errors, and synchronous with the global timing. In order to optimize our data volume transfer over the allocated data band-width, to the space-time of final event building procedure, we have emphasized the position information. Contrary to the TDR FEE version which register up to 32 time frames for each interaction, we choose to send two times the same one-time frame signals, one in the R-pairing and second in the T-pairing (see section 3.3). The signal itself is measured at the maximum of the analog signal.

We will describe in the next section how all requirements and optimization strategies discussed above were incorporated in the design of the main back-bone of the FEE, the ASIC FASP.

4.1 Fast Analog Signal Processor ASIC

The Fast Analog Signal Processing (FASP) ASIC is designed for processing the signals induced on the TRD-2D pads. The CHIP delivers outputs compatible with the CBM DAQ in which the FASP is integrated. The ASIC is composed of 16 processing channels and a set of common circuitry (see Fig. 4.1.1) in the middle region. The main components of a processing channels are:

a. Charge-sensitive pre-amplifier : It is responsible for amplifying the pad signal with a minimum noise contribution. For this reason we have selected a charge-sensitive amplifier of folded-cascode type.

b. Pole-zero circuitry : It differentiate the output signal of the pre-amplifier such that one can obtained a larger dynamic range and a more stable base-line.

c. RC filter of the second order of type "double T" : It transforms the output of stage *b.* to a half-Gauss shaped, thus effectively limiting the frequency output range with direct consequences on noise reduction.

d. RC filter of the second order of type "Sallen-Key" : It improves the output of stage *c.* for a better noise reduction.

e. Peak-detection circuitry of a half-Gauss shaped signal : This stage, which operates on the output of stage *d.*, detects and maintains the peak value of the half-Gauss shaped signal, thus providing as channel output two types of signals: the half-Gauss or its maximum value over a predefined time interval (*flat-top*).

f. Logical time signals generator for downstream control : Each channel can control an auxiliary Analog to Digital Converter (ADC), implemented either as a different block in the same ASIC or as an independent component. These circuitry is responsible for mixing the digital output of a discriminatory analysis of the analog signals from previous stages to control the ADC unit. It also adds similar logical signals from neighboring channels in order to generate commands (*e.g.* flat-top) from multi-channel correlated analysis (*e.g.* processing of a sub-threshold signal if an over-threshold signal is detected on neighbors)

In the median zone of the FASP layout, as it is presented in Fig. 4.1.1, a region of common components is located which are used for all 16 channels described above. This circuits are selected from standard libraries according to the implementation technology for the ASIC and noise optimization:

a. Processing circuits for reference V_{ref} and threshold V_{th} voltages : They are controlled from outside and applied to all processing channels through a network of amplifiers, buffers and current mirrors.

b. Generator circuits for polarization potentials : This are components which adjust the input voltage of 3.3 V to the operating potentials of NMOS and PMOS transistors of various amplification stages.

c. Analog and digital buffer circuits for I/O and over-potential protection.

The production of the FASP ASIC was done by the AustriaMicrosystems-AG (AMS) company according to the CADENCE design. We have used the 0.35 *microns* CMOS technology of type B4C3 NWELL. The resulting CHIP has an area of $3.4 \times 4\ mm^2$ without the scribe-line[16].

A list with the technical specifications for the FASP ASIC is provided in Tab. 4.1.1.

[16] The boundary line of identical CHIPS on the silicon wafer.

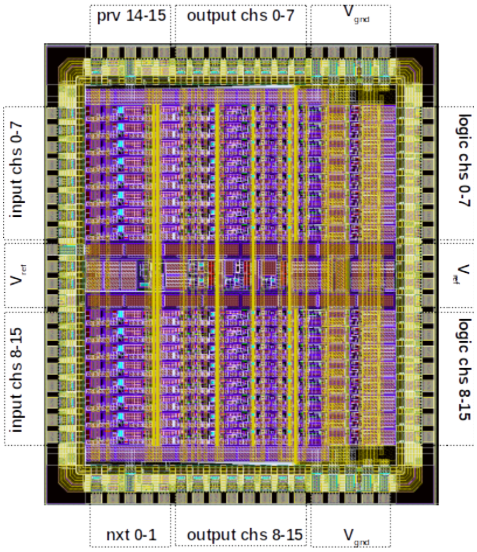

Figure 4.1.1: The layout of the FASP ASIC (AMS 0.35 μm technology); the 16 processing channels are arranged from top to bottom in pairs of 8 and the median region is allocated to common circuitry.

Table 4.1.1: The specifications of the FASP (version 04) ASIC.

Specifications	FASP-v0.4
Average pulse rate	0 - 2 MHz
Detector pad capacitance	25 pF
Number of analog channels	16
Input polarity	positive
Adjacent channel pairing	yes
Charge input range	0.15 fC ... 165 fC
Input type larity	Positive (asymmetric)
Analog output voltage swing	0 ... 1 V
Analog output DC voltage level base line (cont. adj.)	0.2 V ... 1 V
Semi-Gaussian output FWHM	290 ns
Peak-sensing output plateau (time)	14 clk. cycles
Channel ENC (C_{det} = 25 pF)	940 e 1170 e (ST = 20 ns)
Cross-talk (max. signal in only one ch., no signals in others)	0.12 %
Cross-talk (max. signal in 15 ch., no signal in one channel)	0.22 %
Self-trigger capability: variable threshold (cont. adj.)	0 ... 165 fC
Logic common event output	neg. 20 ns width
External clock synchronization	max. 80 MHz
Logic signal channel wise, clock synchronized, output	yes
Channel synchronized logic signal for semi-Gaussian output	to thres. level / to max. ampl.
Channel-wise synchronized logic signal for semi-Gaussian output	neg. 20 ns to thres. level / to max. ampl.
Channel-wise synchronized logic signal for peak-sensing output	neg. 20 ns to thres. level / neg. 14 clock cycle to max. ampl.
Channel neighbors trigger enable / disable (1-bit selection)	yes

A detailed analysis of the main characteristics of the FASP ASIC was done within the CADENCE framework. Here, only some highlights of this studies will be reported. In Fig. 4.1.2 left we have studied the electronic noise associated to the input capacitance. The capacitance of the 1 cm^2 pads coupled at FASP inputs for lower than 1 kHz/cm^2 rates is 25 pF which translates to a noise of 840 e^-. With increasing rate, the dielectric properties of the active gas are changing, and therefore the noise. A technique to measure the relative variation of the input capacitance during data taking is covered in section 5.3 where a calibration with injected step signals on anode wires is discusseed. In Fig. 4.1.2 right the estimation of the linear response of the chip is presented. The deviation from linearity was estimated to 0.06% on the specified input range. More details on the topic as well as measurements are given in the next section.

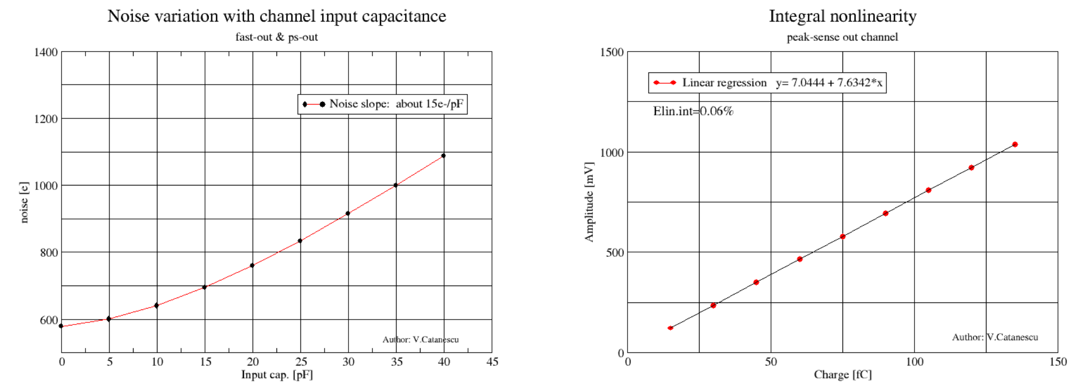

Figure 4.1.2: Main characteristics of the FASP amplifier estimated based on CADENCE design; The noise level as function of input capacitance (left) and the integral linearity as function of input charge for the specific range (right).

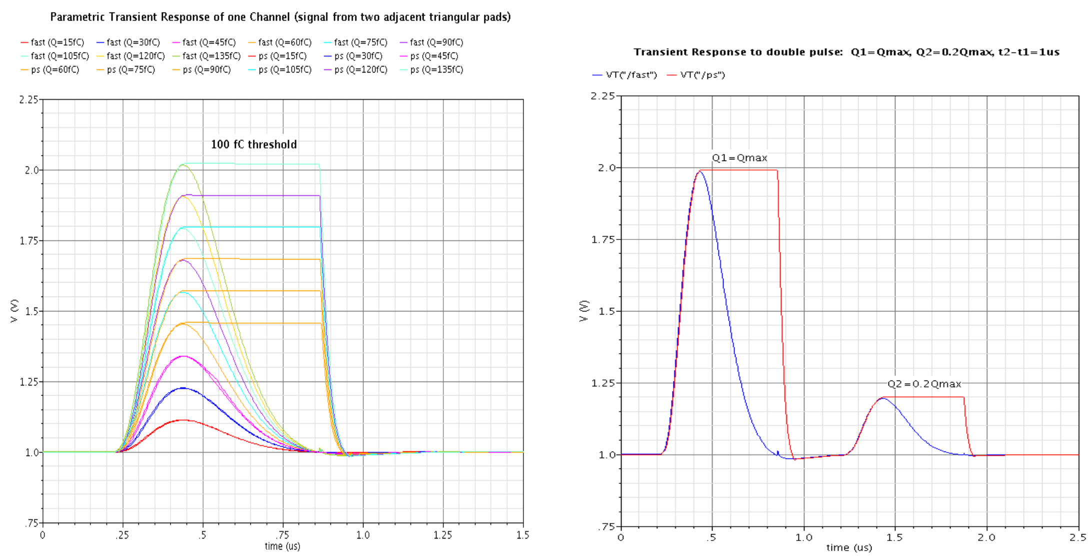

Figure 4.1.3: Analog signal output for the FASP ASIC as function of input charge for a 100 fC threshold (left) and the response to a repetition rate of 1 MHz (right).

The response of the chip in terms of timing, shape and amplitude, is needed to define the next stage of data processing, the ADC. In Fig. 4.1.3 the FASP output is estimated as function of two external parameters; the input charge (left) and the time interval between consecutive signals (right). In the left panel, one can see the two types of outputs generated by FASP, the semi-gaussian and flat-top. It is seen that for the set of 18 input charges from 15 fC to 135 fC the output may differ depending on the threshold of 100 fC set in this example; thus for charges bellow threshold only semi-gaussian is generated while for charges larger than this value flat-top (and chip-select) signal is also generated (user selectable). For normal operation only signals over the threshold will trigger the ADC and thus data recording. A realistic example of high rate signals per RO channel is presented in Fig. 4.1.3 right, for two signals separated by $\Delta t = 1\ \mu s$, the first signal being at the end of input range ($Q_{max} = 165\ fC$). One can see that both signals are fully processed thus proving that FASP can fully process signal rates/channel up to 1 MHz.

4.1.1 The QA procedure for the FASP chip

In this section we will present the performances of the FASP chip as they are tested on the test board (YBE IT WOULD BE NICE TO HAVE SOME DESCRIPTION OF THE BOARD).

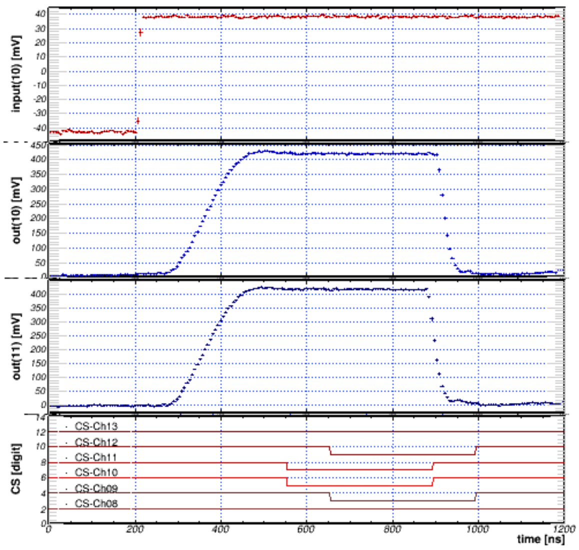

Figure 4.1.4: Main signals of the FASP ASIC as they are measured on the QA board; from top to bottom: the single channel input, the analog output of the direct and paired channels and the logic signals which are used to control the ADC.

In Fig. 4.1.4 a selection of signals is presented which explains the main functionality of the FASP ASIC. The top plot shows the input signal which is applied at time offset of 200 ns on input pad 10. The signal on input 10 is fed on channel 10 and 11 due to pairing. On the next two plots the analog output of channel 10 and 11 is presented as function of time. One can notice the Flat-Top (FT) shape which conserves the maximum value of the formatted semi-Gauss shape for a predefined time. In the bottom plot of Fig. 4.1.4 the logic gates used to control the ADC stage, the so called Chip-Select (CS) signals, are presented for channels $8 - 13$. The CS gates for channel 10 and 11 are opened at 550 ns for 350 ns *e.g.* 14 clk cycles of 40 MHz. The CS gate is used to mark the length of the FT for ADC conversion of the maximum signal. Besides the channels which have signals, and subsequently the CS, there are also two CS on channels 9 and 12. They are produced by enabling the *neighbor channel trigger* option. Such option is used to force the processing of under-threshold signals adjacent to the triggered signal clusters. The digital processing inside FASP to force trigger on neighbor channels takes up to 4 clk cycles which explains the relative delay of 100 ns between over and under threshold signals.

A complementary behavior wrt. Fig. 4.1.4 is presented in Fig. 4.1.5 where a screen shot from the oscilloscope with four analytic signals is shown. The test is used to observe the pairing of input channels from chip to chip, *e.g.* the pairing of last channel from first chip to the first channel of the last one. The setup is realized on the test board with two inter-connected FASP chips. A positive step function signal, used to mimic the detector signal, presented in yellow (①) in figure, is inserted on the 15^{th} input of first chip. The clock of 40 MHz used to operate the chips is inserted from outside and also synchronized in the figure under magenta (③). The analytic outputs of channel 15 and 0 from the two chips are observed in figure under the green signal (④) and blue signal (②) respectively. From the settings of the oscilloscope one can see the two signals being of the same amplitude and synchronous. The successful transmission of control gates as in Fig. 4.1.4 was also observed.

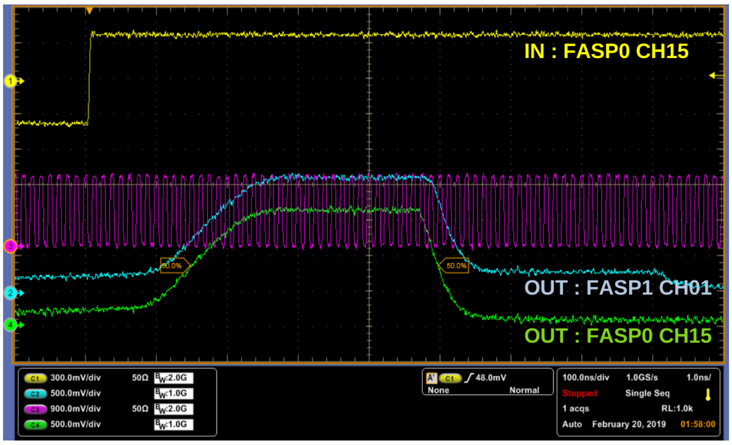

Figure 4.1.5: Chip-to-chip FASP pairing. Four relevant signals for FASP processing are presented in a screenshot from the oscilloscope : the input on channel 15 (last) of FASP $id = 0$ (yellow), the clock of 40 MHz steering the chip (magenta), the direct signal on channel 15 (green) and the paired signal on channel 0 of a second FASP chip $id = 1$ (blue).

4.1.2 Performance of the FASP ASIC; Model vs produced chip

The shaping, amplification and timing characteristics of the FASP chip, need to be well controlled at the design level as well as for each individual chip used in the experimental set-up. Such information is needed for calibrating the local features in the setup in order to produce unbiased measurements. For such procedures, the CADENCE tool and a test board was developed. For both setups the corresponding FASP design/chip was instantiated. A step function was feed in the ASIC on one input and the output was observed for the direct channel. In the simulation case two time intervals were selected injecting the same charge, of 3 ns and 100 ns respectively.

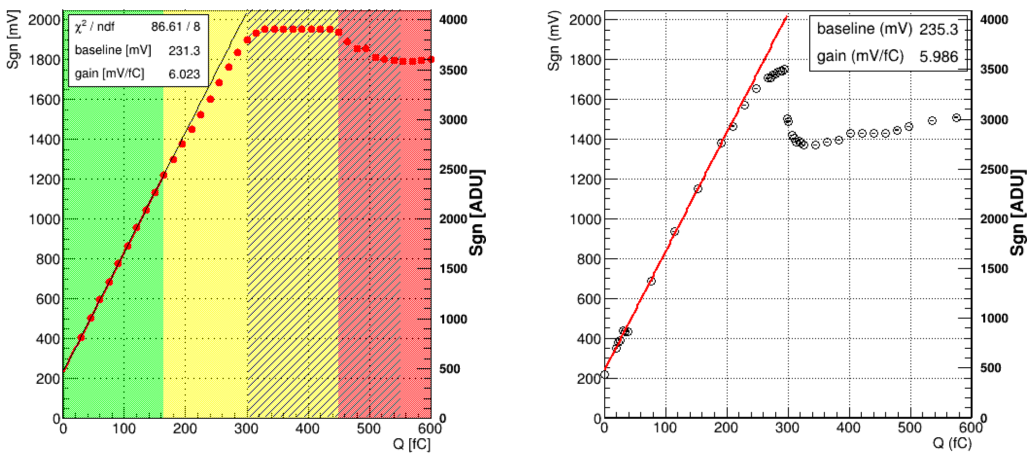

Figure 4.1.6: Transfer function of the FASP ASIC based on CADENCE simulation (left) and tests of bonded chips (right); the gain of 6 mV/fC and a baseline of 225 mV is considered for both CADENCE and the test chip.

In Fig. 4.1.6 the gain calibration procedure is exemplified on both the design (left) and one channel of a bonded chip (right). On the Tab. 4.1.1 the entry *"Charge input range"* defines the upper limit for the linear response. The linear fit is performed on Fig. 4.1.6 (left) up to charge $q = 165$ fC with thick colored line (see green shaded area). The linear fit is extrapolated up to 300 fC to show that good linear behavior is kept for almost double the range in specifications.

It is also shown that for a short pulse (3 ns width)[17] the gain from this simulation confirmed the design value of 6 mV/fC. As discussed above for the properties of the FASP ASIC it is mandatory for the chip to have a good behavior in case of charge overflow. This feature is tested by feeding the FASP design charges which are above the nominal range (15...165 fC). One can see in figure, that up to $q = 450$ fC (almost three times the maximum specified value) the FASP response has a linear dependence and nice saturation plateau (see yellow shaded area in Fig. 4.1.6 - left). For even larger values there is a drop in the plateau value (see red shaded area). Such behavior, although rarely possible in practice, can potentially produce wrongly reconstructed energy deposits. To avoid such operation corners we selected a 12 $bits$ ADC with the input voltage range of 0...2048 mV. The conversion to ADC units (ADU) is shown on the scale on the right of the figure. For all charges above the ≈ 300 fC we can estimate only a lower limit for the energy deposit.

In order to check the FASP design, we have tested the bonded chip, channel by channel, on the test board. An example of such a measurement is shown in Fig. 4.1.6 right. The charge is induced on a capacitance by a fast raising signal of 5 ns comparable with the CADENCE simulation. The linear fit shows the gain of 6 mV/fC demonstrated on the chip. The region up to charge 300 fC is very similar to the CADENCE design. Above this limit, the plateau region present in the left figure is missing, and a more enhanced depression of the return value is observed (see hatched area). A possible explanation may be searched in the details of the input signals used, for design simulation relative to the bonded chip. The CADENCE input current signal of 3 ns width has fast fronts of 50 ns. For the bonded chip, the voltage input is converted via a capacitance with much slower fronts. For the experimental measurements it is the second response characteristic which is of interest.

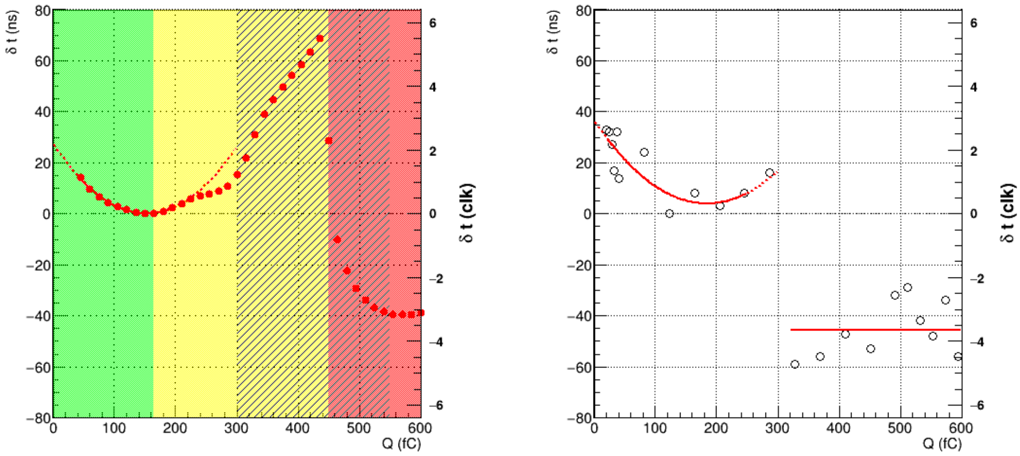

Figure 4.1.7: The time walk for generating the CS gate, in ns and 80 MHz clk, as function of the input charge relative to the fastest signal ($Q = 120$ fC); results of testing the FASP design within the CADENCE framework (left) and for the test board (right) for the same setups as in Fig. 4.1.6.

Another feature of importance is the timing of signals. In Fig. 4.1.7 we present the results of testing the FASP design within the CADENCE framework (left) and on the testing board (right). For the CADENCE test, similar to the results shown on Fig. 4.1.6, we used a 3 ns width input current, and we record the time of the CS gate wrt. the input front. Additionally, this interval is re-based to the response for signal at 165 fC, to capture only the walk effect in the ASIC. For increased readability the output is fitted with a parabola around the minimum value.

[17] The test was repeated for a nominal TRD pulse of 100 ns width with similar outcome but not shown here for simplicity.

The colored regions in Fig. 4.1.7 left correspond to those specified in Fig. 4.1.6 left. The delay induced by ASIC is $\approx$ 10% of that induced by the electrons drift in the ROC and is systematic wrt. input charge. Thus, a proper calibration of each RO channel can reduce such uncertainty. A calibration procedure is sketched in Fig. 4.1.7 right. The procedure is based on producing a similar time response vs charge correlation plot as the one used for the design. If we compare the representations from the two panels of Fig. 4.1.7 we can see similar trends as those observed in Fig. 4.1.6 namely that for charge up to $\approx 300\ fC$ the design and bonded chip coincide. It is also the case for values of input charge above 550 fC. The discrepancy appears in the missing plateau region for the bonded chip (see hatched area) which can be here also attributed to a similar differences in the inputs for the two results.

4.2 Generic Event Time-stamping Streamer

The Generic Event Time-stamping Streamer (GETS) *core* is the digital companion of the FASP ASIC used to interface the TRD-2D analog FEE layer to a free running DAQ. Its primary task is to provide the primary timestamping of the hits and the first level FIFO. As the current implementation is on FPGA, GETS is a parametrized HDL module, currently written in System Verilog, coded such that implementation into an ASIC would be as easy as possible. The current firmware implemented on the GETS board contain the GETS cores for six FASPs (three for each FPGA), the interface to the transport layer implemented using GBTx technology and some minimal auxilliary circuitry required for servicing FASPRO board, such as the control of DACs providing the threshold voltage for FASPs.

The GETS core receive the ADC data and the time signal (a pulse) of it from the FEE (the FASP ASIC) and attach to it a primary time label, the *slice* . As it is not practical to use at this primary level the full time label of the experiment, the length of the slice label is small. In the current GETS core implementation, the length of the slice label is a parameter, the currently used value is 7 bits. Also, a channel number, *ch_id* (4 bit) is attached, identifiyng the FASP channel (one FASP has 16 channels) providing the hit. In the case of TRD and FASP-generated flat-top, it is not possible to generate a hit on one channel more often than one in 16 clock periods. The GETS core exploit this particularity by avoiding the use of channel FIFOs and use 2 registers, one active on write (when a hit is sent by FASP) and one active on read by the rest of the core, the 2 registers being interchanged every 16 clocks. One may see this as a simple 2-word deep channel FIFO. The read registers are sequentially (by the channel number) multiplexed on the output bus, to be written into the output FIFO. In order to make room for other streaming functions, the read from the registers and writting on the queue is performed at a clock of double the frequency of the main clock. In this circumstance, there are actually 32 channels multiplexed into the FIFO writting bus, 16 *primary* channels containing the data from the FASP channels and 16 *auxilliary* channels. The distinction between primary and auxilliary channels is provided by a flag, *isaux*. Two of the auxilliary channels (0 and 1) are used for streaming purposes, the rest are available for other uses.

The auxilliary channel 0 (the *epoch channel*) is used for sending each time the slice label reach its maximum value a word containing another time-related information, the *epoch* label. The length of epoch label is also a parameter in GETS core. The current implementation on GETS board use a length of 21 bits for epoch label. Thus, the stream of data produced by the GETS core consist of words containing data for GETS channels (primary and auxilliary, except epoch channel) periodically including words for epoch channel, *epoch words*. We refer the (variable length) sequence of non-auxilliary channel 0 words followed by one epoch word as a *nanoslice*. In the current implementation, a nanoslice contain the data for 1 FASP for a time interval of 128 80 MHz clock periods, corresponding to 64 40 MHz (CBM main) clock periods, i.e. $1.6\mu s$

The auxilliary channel 1 (the *error channel*) is used for managing the backpressure from upper layers by self-throttling. The FIFO has 2 thresholds, a *suspend threshold* and a *resume threshold*. Both are live configurable (i.e. may be set by a configuration register). When the space available in the FIFO become than suspend threshold the auxilliary channel 1 (acting right before the epoch channel) insert a word for itself (*errbegin* word) marking the beginning of the throttling and decide to interrupt the stream, permitting only the next epoch word to be written into the queue. When the space available in the FIFO goes over the resume threshold, the error channel insert a word (*errend*) marking the end of throttling and containing a counter (*errct*) for the number of times the epoch label passed trough the maximum value during the throttling. The length of errct is a parameter and currently it is 20 bits. Between the epoch word right after the errbegin and errend (immediately followed by an epoch word) no word is written into the queue. Thus the stream produced by GETS consist of *complete* nanoslices or the empty nanoslice at the resume from throttling. No partial nanoslice is possible.

Using epoch and slice, a reader of the stream produced by GETS may reconstruct a total time label of 28 bits, which, at the currently used 80 MHz clock, amount for ~ 3.35 s. To this, a stream reader may add another time label (the *superepoch*) producing a timelabel of desired size. Taking into account the length of errct, an accurate (resilient in the case of throttling) 48-bit (~ 81 days) full timelabel may be implemented.

In the current implementation on the GETS board, the words from the FIFO are read into a serializer and sent on a 320 Mbit/s e-link, one e-link for 1 FASP. On the receiving board (CRI or like), the e-link data is de-serialized and feed into a *stream queue*. A merger module was implemented for reading from a (parameteric) number of stream queues and perform the *time-based* merging. For this purpose, the full 48-bit timelabel is reconstructed. During the merging, an identifier for the merger's input channel is added (*fasp_id*). The output from the merger is feeded into a queue from where it is read by a module producing the data into the format required by CBM's FLIM interface ([49]). The error messages generated by the GETS core are processed in the merger during stream recostruction and removed from the stream. The output of the merger does not require playing the stream, so the CBM's microslices generated to FLIM are self-consistent. For now, the data is not time-sorted within a nanoslice, so the time length of a microslice must be a multiple of nanoslices.

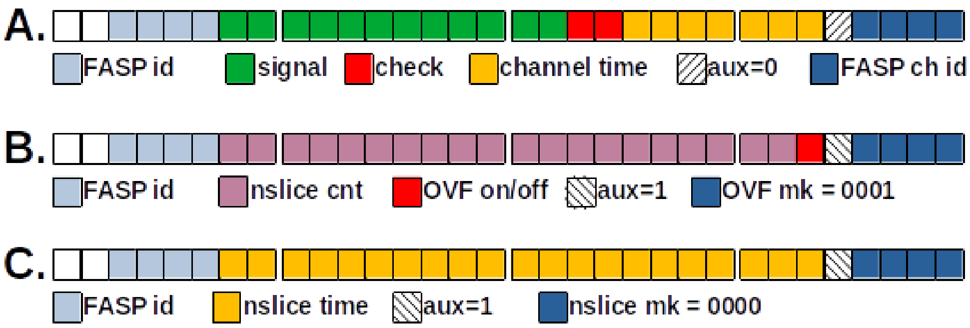

Figure 4.2.1: Descriptors for the basic word used in the TRD-2D; **A.** data, **B.** FIFO overflow and **C.** nano-slice terminator respectively.

In Fig. 4.2.1 the three types of messages generated by GETS are listed. The message A is of the *data* type. For a 4 byte word the bit significance is as follow:

- 2 bits reserved for encryption (not used for production);
- 4 bits to encrypt FASP id between 0 and 12;
- 12 bits signal amplitude as given by a 12 bit ADC;
- 2 bits to check transmission line integrity. Should be set to constant values selected by configuration;
- 7 bits for the signal time label counting within epoch (128 clks);

- 1 bit message type marker $aux = 0$ for data;
- 4 bits for FASP channel id within the current FASP chip *FASP id*.

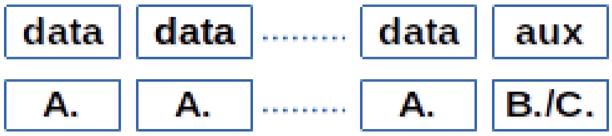

Figure 4.2.2: Dynamic structure of a nano-slice produced per FASP (see Fig. 4.2.3) for which the word structure is shown in Fig. 4.2.1.

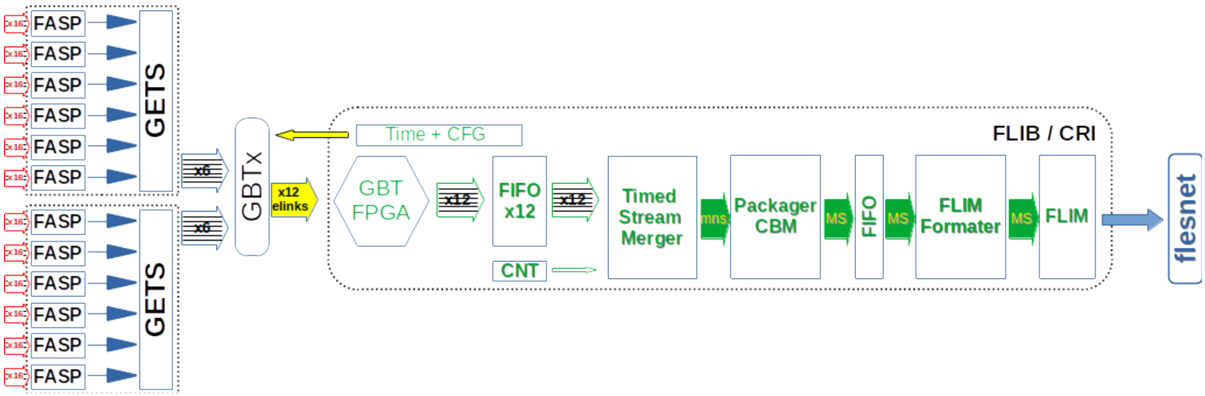

Figure 4.2.3: Schematic view of data aggregation over the TRD-2D DAQ chain for 1 GBTx transport line.

4.2.1 Radiation hardness

The current version of FASPRO board was not designed taking into account the behaviour in radiation. We intend for the final version to use different ADCs and have radiation tests for FASP.

The GETS board was designed by choosing commercially available components for which we found tests regarding behaviour in radiation environment. The DAC chip (currently used for generating threshold voltage for FASPs) is the most sensitive component, according to the tests it may be used up to approx 20 kRad. It might be removed in the final solution and be replaced with CERN's GBT-SCA. The rest of components used on GETS board are expected to work to 80 $\sim$ 100 kRad. The PolarFire was tested by Microsemi ([44] [45] [46]). The tests were performed for basic elements (configuration, logic elements, I/O buffers, overall behaviour, etc.), but did not include the high speed serdes.

For CBM we aim for 1 board which include:

- a more compact solution for FASP bonding (e.g. flip chip), radiation hardness test for FASP (use AMS C35 technology)

- PolarFire should stay

- a solution for ADC should be identified. For now, the most promising is ADS52J90 ([50]) for which a radiation tolerance test was published ([51])

- transport to CRI may include GBtx/lpGBTx or use directly the PolarFire serdes (if further informations regarding their radiation tolerance show up). One GBTx probably has to be used anyway, because a clock source synchronized with the CBM clock is required and we are not aware of any non-radhard jitter atenuator with good behaviour in radiation

- for optics, we are not aware of convincing positive tests for commercial (non-radhard) transceivers, therefore the ones provided by the Versatile Link project will probably be used

Experimental tests for FASP, which might be relevant:
- TID - may be done in house at gamma irradiators
- SEU - E pr. $>$ 200 MeV. Running chip, monitor, experimental setup should be developed and deploy. Couple of years to complete.

4.2.2 Power consumption and cooling

The recent (ongoing) tests indicate that the power consumption for 1 GETS board and 1 FASPRO board, fully populated with 6 FASPs is less than 10 W, i.e. $\sim$ 105 mW/channel. This figure does not include the power requred by the C-ROB board. Most of the consumption come from the ADCs, where we expect a substantial decrease by using different ADCs.

5 Simulation and Reconstruction

In this chapter we will discuss the modeling of each experimental element included in the TRD-2D system design such that one can realistically reproduce the experimental information. Here we will discuss charge sharing between triangular pads, realistic implementation of FASP analog and digital response. The topic of realistic description of the material budget, for the detectors themselves but also infrastructure, is also of interest here but it was covered in section 3.2 and 3.4.

The second topic addressed here would be to reconstruct physics observables like particle position, arrival time and energy. Such data filter algorithms are applied equally on measured and simulation data. they can also be used as QA tools based on the comparison of the outputs for the two types of data.

5.1 System Modeling - from ROC to FEE

We will present in the following the list of models used in replicating the physics and electronics of the TRD-2D detection system, as they are designed for the CBM implementation, starting from ionization of the gas to the timing of the output signal entering the ADC.

5.1.1 Active volume pixels

The anode wires are attractors for the electron cloud (see Fig. 3.1.2 left in section 3.1) and thus they define the granularity of signal formation mechanism. We model the active volume as composed of independent Amplification Cells (AC), which are sections in the gas volume, parallel and centered on each anode wire (containing 2 cathode wires), of size $540 \times 3 \times 12\ mm^3$. The particle trace in the active volume is considered straight between the entry and the exit point and thus, for each particle a set of segments are defined through the intersection of the straight line with AC.

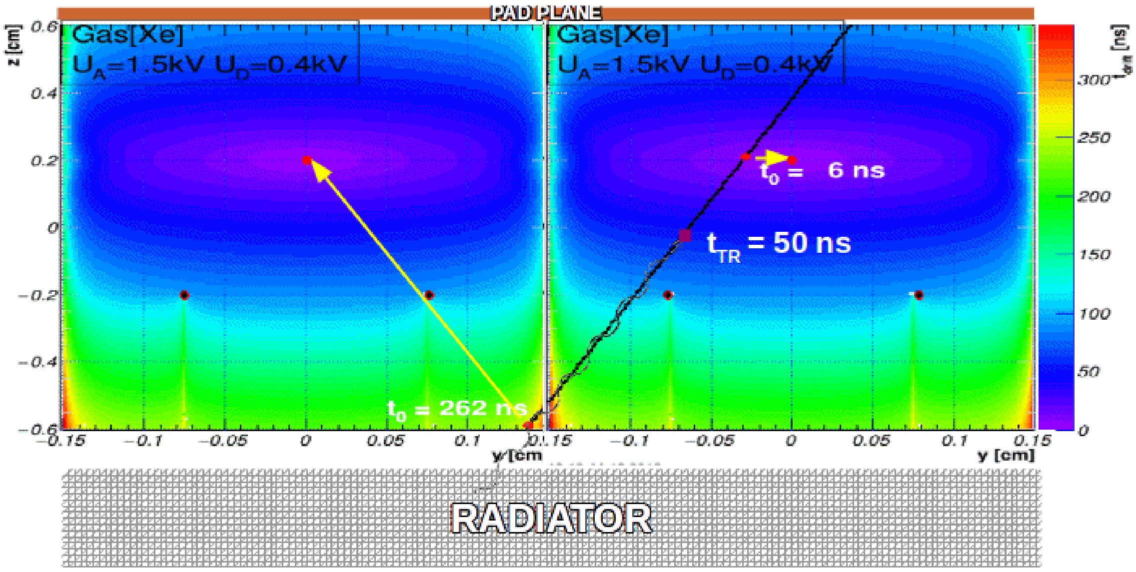

Figure 5.1.1: The straight line model of the particle trajectory inside the active volume of TRD-2D is decomposed in two segments in the adjacent *independent amplification cells* crossed.

Particle trace (black line) decomposition using the *independent amplification cell* model is presented in Fig 5.1.1 for the case of two adjacent cells. The color code represent the electron drift time from each point of the cell to anode (red at $(y, z) = (0, 0.2)$). In this model for each track segment the y position is given by the closest anode wire (see yellow arrows) and the time by the shortest drift time of all points from the particle trace (see red dot on the trace in the figure). For the example in Fig. 5.1.1 two signals are generated with drift delays of $t_0 = 6$ ns and 262 ns respectively.

For TR interaction we assume the emission parallel with the electron trace and the position given by absorption depth in the gas (see red square in figure). For the example in Fig. 5.1.1 the TR is the third signal at $t_{TR} = 50$ ns. In all cases the drift maps for amplification cells have to be loaded for the actual values of Gas, U_A and U_D at which the system is operated.

5.1.2 Energy deposit

The energy deposit value simulated by the transport engine (e.g. Geant 3/4) for charged particles E_p is divided proportional with segment lengths l_i. For TR, the full energy E_{TR} is released in the point of absorption (if it is in the gas) and for there the atomic processes of PE and EC are simulated ($\mathcal{P}_{PE/EC}$) according to atomic data of the working gas.

$$E_{dep}\ (keV) \;=\; E_p\ \times\ l/L \tag{21}$$

$$E_{dep}\ (keV) \;=\; E_{TR}\ \times\ \mathcal{P}_{PE/EC} \tag{22}$$

with L the length of particle trace inside the active gas.

5.1.3 Pad Response Function for triangular pads

The Pad Response Function (PRF) for the triangular shaped pads depends on a 2D model for the inductive effect of the amplification charge cloud. For simplicity we assume a Gauss shape $\mathcal{G}$ for each spatial component of the form:

$$w = q^{\nabla/\Delta} \;=\; \int_{-pw/2}^{pw/2} dx \int_{-k_x}^{k_x} dy\ \ \mathcal{G}(x|x_p, \sigma_x)\ \mathcal{G}(y|y_p, \sigma_y) \tag{23}$$

$$\approx\ \sum_i \sum_j \mathcal{G}(x_i|x_p, \sigma_x)\ \mathcal{G}(y_j|y_p, \sigma_y)\ d\mathcal{A}(i,\ j) \tag{24}$$

where k_x is the slope of the boundary between upper and lower triangular pads, $(x_p,\ y_p)$ is

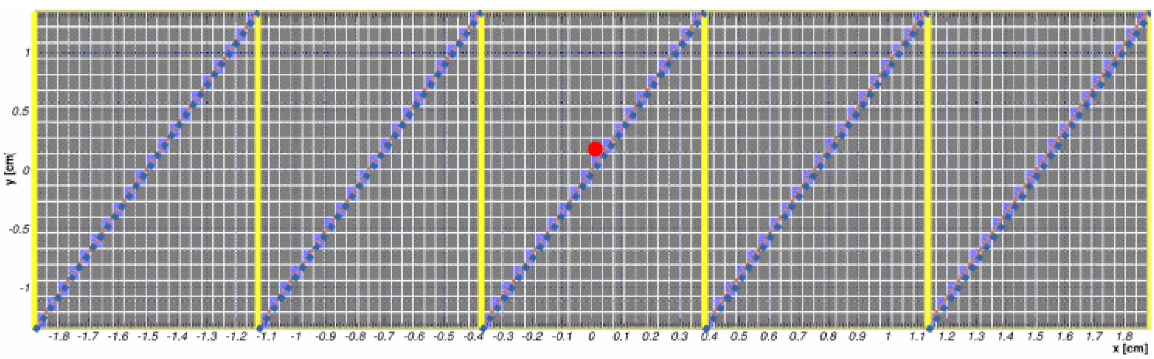

Figure 5.1.2: The 5-pad-column $x - y$ discretization of the pad-plane around one MC point (red dot at $(x_p,\ y_p)$) used to calculate the PRF as described in Eq. 24; the pads area are emphasized by continuous yellow and tilted dotted blue delimiters.

the position of the center of the charge cloud at the z of the anode wire (central red dot in Fig. 5.1.2), $(x_i,\ y_j)$ is the center position of bin indexed $(i,\ j)$ (gray rectangles in Fig. 5.1.2) and $d\mathcal{A}$

its effective area i.e.

$$
\begin{aligned}
d\mathcal{A} &= dxdy \quad if\ (x_i,\ y_j) \in\ pad\ (gray\ in\ figure) & (25)\\
&= dxdy/2 \quad if\ (x_i,\ y_j) \in\ boundary\ (violet\ in\ figure) & (26)\\
&= 0 \quad rest & (27)
\end{aligned}
$$

with σ_x being the width of the $1D$ PRF across pads (normally $0.5 \times pw$) and $\sigma_y = \sigma_x$ the width perpendicular to the anode wires.

For each track segment and TR photon, the sums in Eq. 24 are performed for 3 $rows\ \times$ 5 $cols$ of pads which result in the weight of each triangular pad in the energy decomposition. The input signal for electronics channel c connected at pad defined by weight w is than given by :

$$
(S^{\nabla/\Delta},\ t^{\nabla/\Delta})_c = (E_{dep}\ \times\ w,\ t_0)_c \tag{28}
$$

with E_{dep} from Eq. 21,22 and t_0 from Fig. 5.1.1.

5.1.4 FASP pairing

It was discussed in section 4.1 that the FASP ASIC is summing consecutive entries in order to avoid S/N effects along the pads. Therefore the following transformation is performed before feeding the output to the FASP modeler:

$$
\begin{aligned}
(S_T, t_T) &= (S^{\Delta}_{c-1} + S^{\nabla}_c,\ 0.5 * (t^{\Delta}_{c-1} + t^{\nabla}_c)) & (29)\\
(S_R, t_R) &= (S^{\Delta}_c + S^{\nabla}_c,\ 0.5 * (t^{\Delta}_c + t^{\nabla}_c)) & (30)
\end{aligned}
$$

with "T" indexing tilt pairing and "R" rectangular pairing as shown in Fig. 3.3.1 in section 3.3 while "c" being the column index (Eq. 28).

5.1.5 Detector gain

The conversion of energy into electrical charge is controlled in the TRD-2D from the anode potential U_{anode} wrt. the cathode potential (signal ground). The exponential dependence of gain on U_{anode} can be determined from electrostatic calculation (e.g. GARFIELD) or measured. In

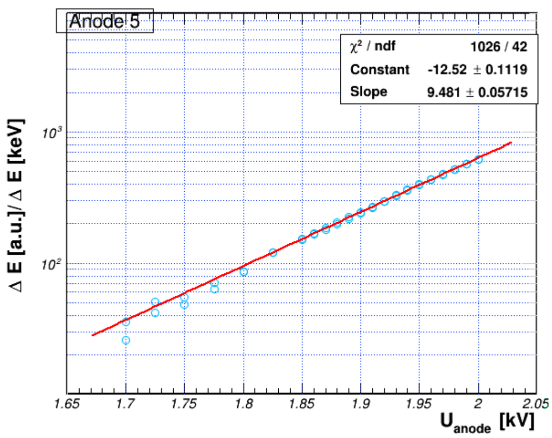

Figure 5.1.3: The gain calibration of the TRD-2D module using the ^{55}Fe energy spectrum deconvolution as presented in section 5.3.2.

Fig. 5.1.3 the results of fitting the gain to U_{anode} are presented for the de-convolution of the ^{55}Fe spectrum measured with full DAQ and standard reconstruction. Details are provided in next sections, especially see 5.2. The condition "$Anode$ 5" mentioned in figure is related to the reconstruction procedure and is meant to select events fully contained in one row of pads. Using the parametric expression from Fig. 5.1.3 one can construct the correlation $E[keV] \longrightarrow E[ADU]$.

5.1.6 Modeling the FASP input

In order to access the FASP ASIC model as it is designed in CADENCE, a transformation from signal in ADU (ADC Units) to charge is needed. In Fig. 4.1.7 in section 4.1.2 the transfer characteristic of the FASP was presented for the CADENCE model (left) and one particular physical realized channel. It is obvious that for each FEE channel one can construct the following convolution:

$$E[ADU]\{\longrightarrow \mathbf{FASP^{-1}} \longrightarrow E_{in}[mV]\} \longrightarrow E_{out}(E_{in})[mV] \longrightarrow \mathbf{CADENCE^{-1}} \longrightarrow Q[fC] \tag{31}$$

where $\mathbf{FASP^{-1}}$ and $\mathbf{CADENCE^{-1}}$ are the inverse of the dependencies presented in Fig. 4.1.7. The convolution sub-chain which is inserted between curly brackets can be skipped if measuring FASP channel is considered ideal.

5.1.7 Modeling the FASP channel

The building modules of a FASP channel were presented in the beginning of section 4.1. Each component has a transfer function which can be represented as $\mathcal{T}_i(S_{in}(t)) = S_{out}(t)$. The modeling of a channel is implemented as the convolution of all $\mathcal{T}_i$, and a filter process $\mathcal{F}$ applied on this result which represent the control gates on the physical ADC. Without going into details, a parametric expression modeling the pre-amplifier is define to convert the $(Q[fC], t_0)$ pair in the function shown in Fig. 5.1.4 left. Once the physical signal is expanded in time one can apply

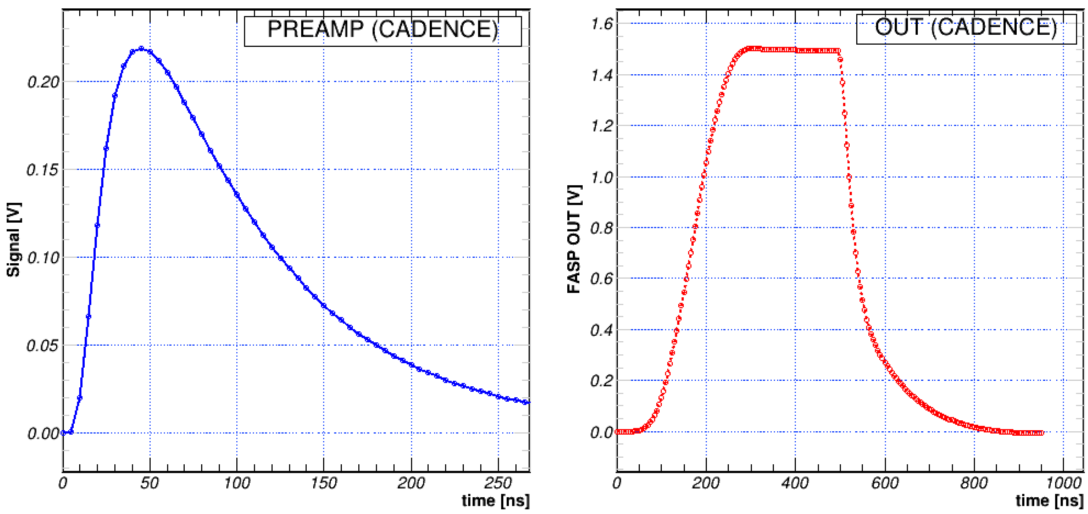

Figure 5.1.4: The model of the FASP channel is based on the convolution of several transformations starting with the preamp signal (left) and ending with the flat-top signal (right).

FEE specific mechanisms like threshold, discriminators and gate generation. All these process render a realistic description of the FEE response ready to be matched with measurements in both amplitude and timing.

In Fig. 5.1.5 an example is offered for one FASP channel of the full $energy - time$ conversion from physics observables (black vertical lines) to analog FEE outputs (red curve). The digital gates are self-understood. One can see that the physical signals appear always in groups of three consecutive signals according to details offered before (see section 5.1.2 with forced TR production). A nice example of signals being closer in time than the discrimination power of FASP is emphasized in green in the figure and labeled as "signal pile-up".

The full details of FASP channel simulations are in the end converted to a data structure called *Digit*, common to all detectors in the CBM experiment, which contains the signal and the

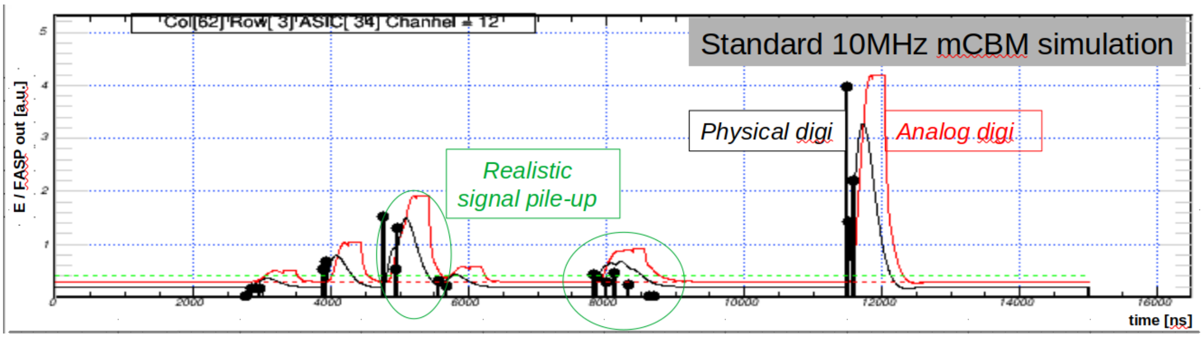

Figure 5.1.5: The full conversion from physical $energy - time$ representation (black lines) to FASP analog output (red) for a 10 MHz interaction rate, central $Au - Au$ interaction (SIS100 electron setup).

time of its generation (CS signal), which is identical with the information coming from the DAQ (see section 4.2).

5.2 System Observables - 4D correlations

In this section the algorithms to reconstruct the properties of particle crossing the active areas of the TRD-2D will be described. The algorithms are applied equally to measured and simulated data and they account for: x-y position , time and energy deposit reconstruction. Since all these estimators are based on the same data set, namely the FEE signals and their timing, a certain degree of correlation is expected. We will show that the 2D position capabilities of our prototype can yield more accurate estimators, not only for position, by using such relations.

5.2.1 Clusters of signals; time and space

Since each ROU of the CBM DAQ is independent from the rest, the only time ordering sequence that is guarantied by the DAQ is channel wise (section 4.2). Therefore, from the serial stream of digits produced by the machine or simulating package, the first level of action is de-serialize into module-row wise. A buffer is allocated to hold time ordered clusters[18]; a *cluster* is group of spatially adjacent digits which are temporary correlated; the time of the cluster is the prompt time of the digits composing it. For each digit in the list there are three outcomes wrt. the buffer content:

- **digit insert** : if the digit is adjacent to the boundaries of the cluster and the time interval between digit and cluster is less than 5 *clk*.

- **create cluster insert** : the digit can not be attached to a preexisting cluster and therefore a new cluster is seeded in the buffer from the current digit such that the time ordered buffer is maintained.

- **create cluster push back** : same as before but the digit is later than all clusters in the buffer; the new cluster is last in the buffer.

A second iteration is performed on the clusters buffer until all neighbor clusters which fulfill the time window condition are merged. The set of digits which compose a cluster is used throughout the reconstruction to estimate the observables of the system.

[18]Historically the simulation/reconstruction software was build in the event-by-event mode. The TRD-2D was developed later, directly for time-based mode, but it is also compatible with the event mode

5.2.2 x-y position reconstruction

As emphasized already several times, the TRD-2D is optimized for position measurements. The measured data and simulations are prepared in the format of digits after which, the reconstruction algorithms are applied. In Fig. 5.2.1, the type of information made available by the TRD-2D system, is shown for different projections.

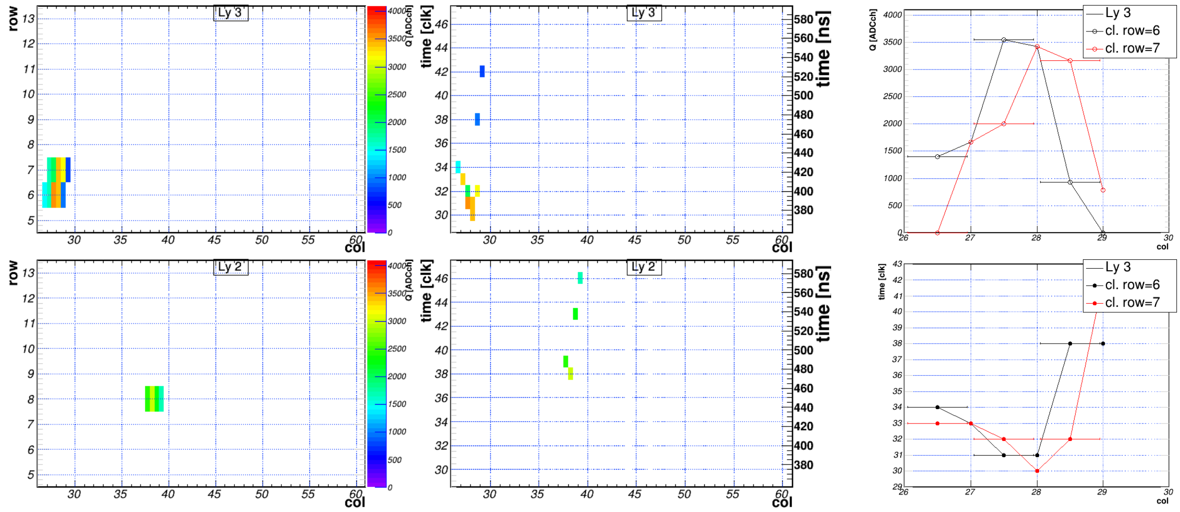

Figure 5.2.1: TRD-2D detectors digit representation of a track crossing the last two layers; column wise, from left to right, the spatial distribution (left), the time distribution (middle), and 1D projections of the complex pad-row-cross cluster from the 4^{th} layer (right).

The CbmRoot contains models which describe the spatial and time distributions of signals measured by the TRD-2D. The representation of a charged particle interacting in the detection volume is given as the set of one pad-row signals contiguous in a limited time interval, called *cluster*. On the left column of Fig. 5.2.1 the spacial representation, as pad column and row indices, is given for clusters in the 3^{rd} and 4^{th} TRD layers. The color code represents the value of the signal in ADU. For the last layer, there are two clusters on rows indices 6 and 7 centered on approximately the same column which represent a double cluster *i.e. pad-row cross cluster* obtained when the particle interacts close to the boundary of pad-rows. A 1D representation of this cluster is shown in the top-right column as signal versus pad-column. The integer values of pad-column represent the "R" pairings while those intermediate are the "T" pairings (see section 5.1.4). The charge center of gravity for "R" pair wrt. pad-column is on its center while for the "T" pairings, depending on the position across wires, it varies between the middle of two adjacent pad-columns. The position across wires has a discreet character as it is correlated with the anode wire position, therefore, the values of the center of gravity for the "T" pairing can take 10 values (see Fig. 3.3.1 in section 3.3) between pad-column index i and $i + 1$. Identifying the shift of the "T" pairing wrt. to pad-column boundary is equivalent to finding the anode wire where the charge amplification took place.

In the middle column of Fig. 5.2.1 the track is represented as function of pad column and time. For the time coordinate both the DAQ representation in 80 MHz $clks$ and the absolute time from the particle incidence are given. The charge of each digit is color coded as in the left column. By comparing the prompt signals in the two layers one can notice a time inversion; although layer 3 signal is faster wrt. particle incidence, it is nevertheless 100 ns delayed if digits are compared. The digit time is a convolution of the drift time and the time response of FASP which have standard values in the 100 ns and respectively 10 ns ranges. Additionally there is phasing uncertainty wrt. the 80 MHz clocking of the DAQ which might introduce an extra 12.5 ns for signals which are almost synchronous. The correlation of time versus pad-column is presented in the bottom-right column of Fig. 5.2.1. The column indices have integer and half-integer values according to the pairing type (see above). The time difference between spatially adjacent signals is of $1 - 2$ $clks$ according to data from Fig. 4.1.7 in section 4.1.2 and clock phasing. For the first and the last signals in a cluster, such differences can be larger (10 clk i.e. 125 ns for cluster in row 7 - red symbols) due to neighbor trigger mechanism implemented in FASP.

In order to calculate the 2D position of incidence the continuous coordinate x - across pads and the discreet coordinate y - on the perpendicular direction have to be estimated. Numerically it is useful to re-scale the pad-plane to the pad-height ($ph = 27.0$ mm) and pad-width ($pw = 7.5$ mm) such rectangular pad is of 1 cm^2 size. In this situation the following COG sums are calculated:

$$s_R = \sum_c^{n_R}(c - c_0) \times S(c)/\sum_c^{n_R} S(c) \tag{32}$$

$$s_T = \sum_c^{n_T}(c - c_0) \times S(c)/\sum_c^{n_T} S(c) \tag{33}$$

where the sums in Eq. 32 are done over "R" paired signals and respectively "T" in Eq. 33. The pad-column index is c and the pad-column with max signal is c_0. In a first approximation, the $x - y$ position offset wrt to position of the pad-column with the maximum signal is given by $dx = s_R$ and $dy = (dx - s_T)$. Such formula would be unbiased for large n_R and n_T but in practice they are each around 3. Additionally, for small clusters, the signal(s) in the extremities which are under threshold may be relatively large wrt. total charge in the cluster. To address such limitations which arise from the limited range of our apparatus we devised a set of look-up-tables (LUT) with effective corrections. Such corrections depend in principle on:

- $\boldsymbol{n = n_R + n_T}$: the total cluster size as sum of partial sizes for "R" and "T" pairings;
- **asymm** : cluster asymmetry wrt to maximum signal for both pairings;
- $\boldsymbol{type(S_{max})}$: whether the maximum signal is of type "R" or "T";
- **ovf** : if FASP over-flow is detected in the cluster.

The corrections are calculated wrt. MC simulations and tested on real data as discussed in section 5.3.1. The expression for position reconstruction become:

$$x_{chmb} = x_c + (dx - \delta x(dx, \mathcal{T}_{cl})) \times pw \tag{34}$$

$$y_{chmb} = y_c + (dy - \delta x + \delta y(dy)) \times ph \tag{35}$$

where x_c, y_c are the chamber coordinates of the pad-column with the maximum signal, dx, dy are uncorrected offsets from pad center in the scaled system (see above) and the δx δy are the MC corrections. The cluster type index, according to the list above, is denoted by $\mathcal{T}_{cl}$ in Eq. 34.

It is seen from above, that the design novelty of the TRD-2D is given by the possibility to measure the clusters' charge sharing, using a tilted pad geometry , in parallel with the rectangular one. Therefore, the results obtained on the y coordinate, directly depending on this feature, is the most notable. In Fig. 5.2.2 the distribution of residuals in the y direction wrt. MC particle position is displayed as function of the reconstructed position wrt pad-row center. The distribution features a alternating pattern of regions with large and small residuals. If compared with the geometrical distribution of wires (vertical red dotted lines in the figure) wrt to pad-rows (see also e.g. Fig. 3.3.1 section 3.3) we can identify the residual maxima with the anode wire positions and minima with the boundaries of amplification cells (Fig. 3.1.2 section 3.1). Correlated with the projection on the pad-row direction shown in the top panel in the figure one can indeed see that most of the particles are being amplified in only one amplification cell. For these particles, since the anode wire is an attractor, the true y position information is lost, and hence the large errors. There are still cases where there are two amplification cells being activated. These configurations result in smaller uncertainties - the areas between the anode wire positions - but also lesser yields.

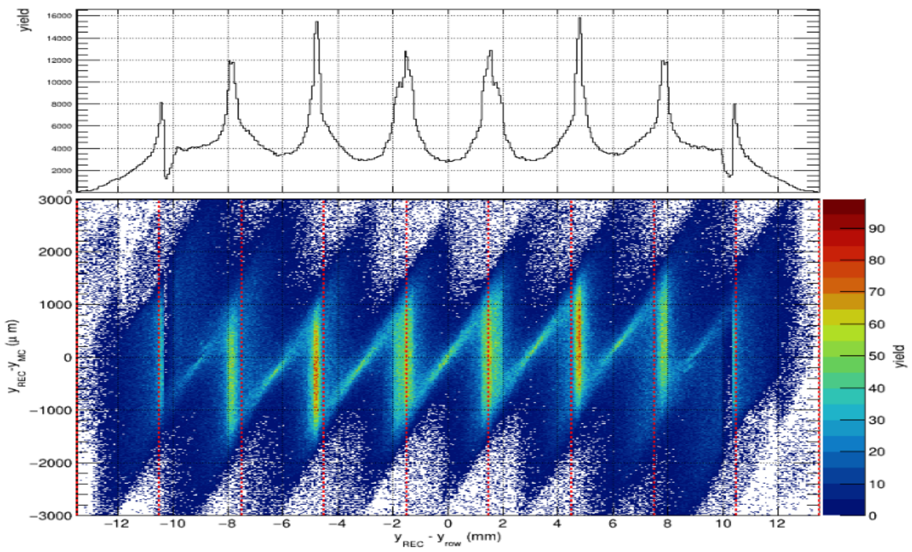

Figure 5.2.2: The distribution of residuals in the y direction wrt. MC position as function of the position inside the pad-column for clusters of $size > 4$; 8 out of 10 anode wires are clearly seen in the figure (red dotted lines) correlated with maxima in the yields (top panel).

For clarity, in Fig. 5.2.2 a selection of large clusters was made resulting in a fraction of $\approx$ 75 % of all single row hits being considered. Nevertheless, even adding the last 25 %, the reconstructed yield distribution is not uniform along pad length, dropping towards pad boundaries. The difference is recovered by merging incomplete single-row clusters which have similar x position and time. Such measured configuration are designated as *pad-row-cross* clusters and are a hot topic for the TRD detector as the position is concerned but also the data volume. In Fig. 5.2.3 the uniformity of the yield distribution along pad-row is analyzed in terms of these criteria based on the MC position information. The particles hitting close to the middle pad-row, i.e. the most center six anode wires respectively, are registered as *single row* clusters. On the 2×2 anode wires close to the boundary, $pad - row\ cross$ clusters are registered if both clusters are sufficiently well measured. Additionally, in $\approx$ 22 % of the cases such clusters are incomplete (black in figure) and thus the anode information is lost.

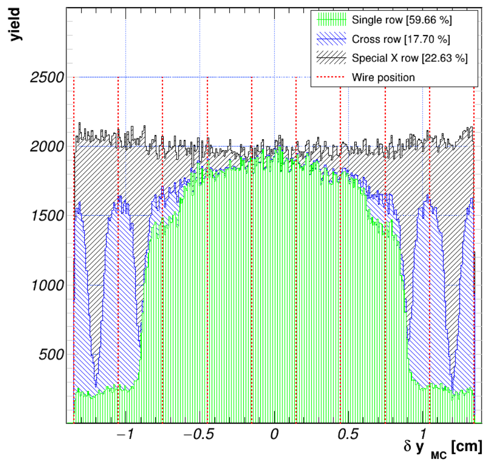

Figure 5.2.3: The distribution of cluster types yields along the pad-row correlated with anode wire positions; complete clusters are produced by particles hitting close to the middle of the row (green), split clusters are produced by particles hitting towards pad-row borders (blue) where *incomplete* split clusters with a partially-missing leg are also produced (black).

The advantages of having a detailed position information, available for the TRD-2D system, is clearly illustrated by the details of the reconstruction procedure; i.e. besides providing an enhanced tracking device, the 2D position sensitivity is operational in disentangling edge effects. While such effects (like charge sharing between pad-rows and the FEE effects thereafter) are self-understood, their identification in the reconstruction is not. The classification shown in Fig. 5.2.3 can be used to flag reconstruction observable (not only position) with larger uncertainties thus producing more relevant results in the context of the experiment.

5.2.3 Energy reconstruction

In a standard approach of reading a MWPC signals with rectangular pads the method for energy reconstruction would be independent on position. For the TRD-2D it is no more the case since "T" paired signals can also contribute to energy determination considering the proper position.

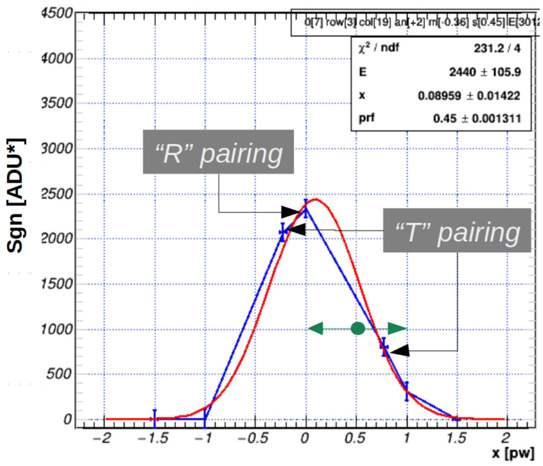

Figure 5.2.4: The method for energy reconstruction after signal calibration and correction of x offset for "T" paired signals with anode index information.

In Fig. 5.2.4 the method for energy reconstruction is presented. The energy is given as the integral of a Gauss fit to the $signal - x$ correlation. For the "R" paired signals, the x coordinate is taken as the integer number of pads from pad-column with the maximum signal, while for the "T" pairings, x is shifted from the nearest half-integer proportional with the index of the anode wire identified during position reconstruction. FEE channel-to-channel variations are calibrated out using the procedure from section 5.3.1 and departures from linearity are accounted for using the channel characteristic shown in Fig. 4.1.6. In order to properly condition the cluster distribution, boundary signals are added with 0 charge. Error parameterization is very important and is considered for both the signal (vertical errors, see also section 5.3.1) and the x position (only for the case of "T" pairings). The "mean" parameter of the fit is fixed to the value of $dx - \delta x$ obtained before (Eq. 34).

In Fig. 5.2.5 we show the dependence of the energy residuals wrt. MC as function of MC position along the pad-row. The absolute normalization of E_{rec} was done wrt. the integral spectrum. As already emphasized the quality of reconstruction can be well described by the anode index, as for the center four anode wires the mean value of $\Delta E = E_{rec} - E_{MC}$ is well defined, independent of the anode wire index and without spurious structures. For boundary wires, due to missing parts of the signal, there is a clear deprecation of the reconstructed energy. In order to quantify the information content of the cluster signal size, the plot is done separately for 4 (left) and respectively 5 (right) signals. One can see that fully contained 5 signal clusters are in average with 0.2 keV larger wrt MC than those of size 4. For clusters which suffer *pad-row edge effects* the difference is of the order of 1 keV. Once acknowledged based on the extra

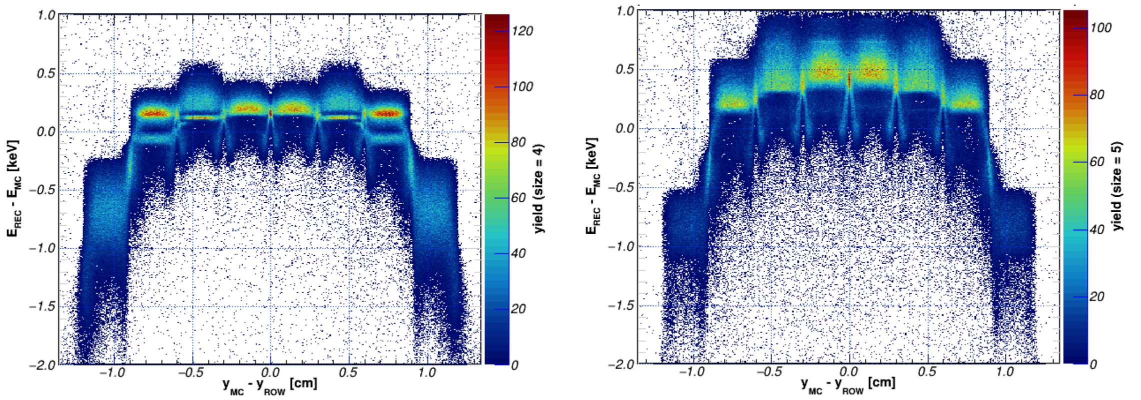

Figure 5.2.5: Systematic effects in the energy reconstruction by investigating the energy residuals wrt. to MC as function of position along the pad for clusters of size 4 (left) and 5 (right).

position information delivered by TRD-2D such effects can be corrected with potential better PID capabilities. Although such studies are beyond the topic of the current document, their possibility emphasize the improvements of the TRD-2D also wrt. other observables than position.

5.2.4 Time reconstruction

Time reconstruction is as important for tracking in the CBM free-running environment as the position determination. Unfortunately the TRD is by construction a detector with bad timing characteristics due to relatively large spread of drift times for different regions of the amplification cell (see Fig. 5.1.1 on section 5.1.1).

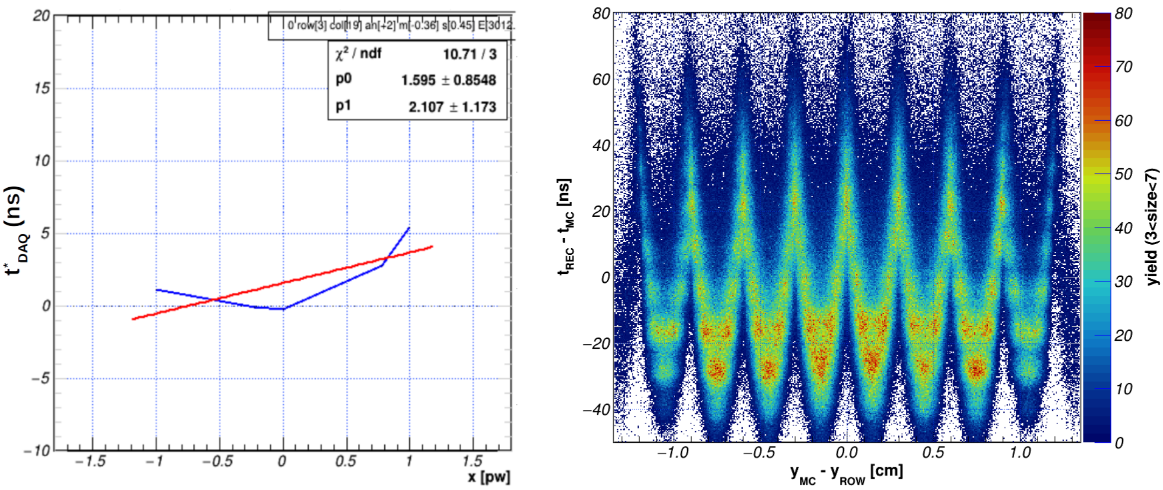

Figure 5.2.6: The method for time reconstruction (left) and systematic effects in the time reconstruction (right) by investigating the time residuals wrt. to MC as function of position along the pad-row for clusters of size $4 - 6$.

In Fig. 5.2.6 left the time profile of a cluster is shown as function of the position x. Same dependence on anode wire index for the "T" paired channels applies as for energy. Here a simple average is performed (simulated by the linear fit) and the parameter p_0 is considered as cluster time. The FEE response time and time walk with charge are corrected using calibration data as shown in Fig. 4.1.7. A global normalization is performed wrt MC time spectrum to account for an average global drift time. In Fig. 5.2.6 right the systematic effects of the system are visible if the time residuals wrt. MC are correlated with the position along the pad-row. The asynchronicity of the TRD over the amplification cell is visible in the periodic profile from the figure. The positions of the anode wires are correlated with shorter drift times and thus the global normalization tend to overestimate the reconstructed time while for the amplification cell boundaries the effect is the opposite. Again, the information content brought by the anode identification technique, can be operational *also* in improving the time resolution of the detector.

5.3 System Performances - PID and Tracking

In order to asses the quality of the reconstructed observables and to match them with the CBM tracking, an *unbiased* estimation of performances need to be done. Traditionally, there are several levels of assessments:

a. **With respect to MC truth for realistic simulations** : such approach is unbiased but might be heavily distorted by the quality of models employ which describe the experimental observables.

b. **With respect to a different, independent system during data taking** : such approach is realistic since it captures all details of experimental observables but is biased by the reference system.

c. **With respect to an "absolute" reference** : the method is based on constructing a calibration setup, as closed to the real working conditions as possible or even running in parallel, and comparing the reconstructed observables with generally known reference values.

Several examples of type a. are provided in previous section and also in sections 1.3 and 1.4. The second approach is mainly used in large scale experiments where the main tracking device (in our case STS) is the reference relative to which, the other subdetectors are calibrated. The third approach is the most interesting, as it allow realistic calibration with un-biased references, but such procedure has to be built-in the system design. The TRD-2D has several built-in calibration procedures which we will shortly describe below.

5.3.1 Calibration

Here, we will discuss the calibration procedure which are specific to the TRD-2D system, due to built in design considerations. They are done with respect to physical references of much greater precision wrt. reconstructed observables as will be seen.

FEE channel calibration for gain and synchronization

The uniformity of signal amplification and time response in the system and its maintenance during irradiation is of paramount importance in a free-running high-multiplicity environment. To asses such run-time calibration/maintenance routine we designed the injection device for the anode HV with the possibility of inserting a step signal of precise amplitude and timing. The specific circuitry is presented in Fig. 5.3.1 with the two active elements The High Voltage (HV) source for the anode voltage and the signal generator (GEN).

From an electric point of view the TRD-2D detector is depicted in Fig. 5.3.1. The detector itself is described by the capacitance A-K and the dielectric in-between. In order to avoid signal alterations due to induced signals on the grounding lines, we have split it in two: *the signal grounding* to which all electrical circuitry refer to (continuous in figure) and *the ground itself* (blue shield in figure) which absorbs the environmental noise. The two grounds are no-where in contact. The signal generator GEN injects step pulses with good fronts (*e.g.* 5 *ns*) on the whole anode electrode. Such signals, while propagating, induce the same signal, synchronously, in all pads. The response of all FEE channels is registered and amplitude and time alignments are thus possible.

In Fig. 5.3.2 two instances of FEE synchronization procedure, using the method of injecting pulses on the anode electrode, are shown. On the left plot the messages send from two FASP

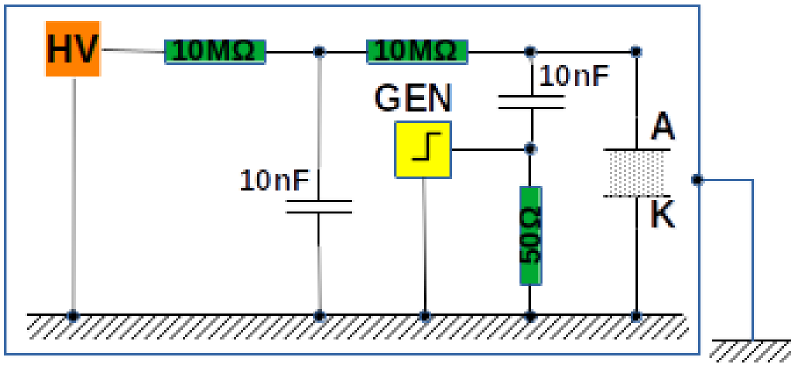

Figure 5.3.1: The equivalent electric circuitry of the TRD-2D detector; the injection HV on the anode electrode (A) and the generator (GEN) to produce calibrating amplitude/timing signal for the system; the grounding scheme is also suggested in the picture.

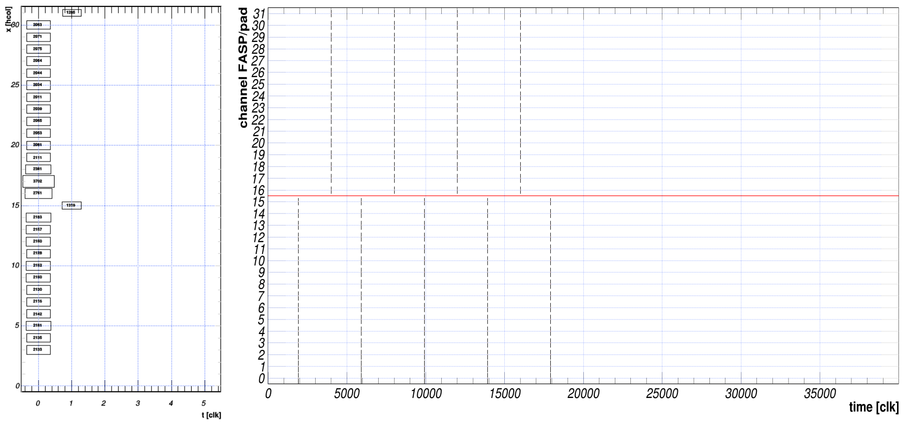

Figure 5.3.2: Calibrating synchronicity by injecting charge pulses through the anode electrode; two FASP chips response to a calibration pulse seen in free-running acquisition (left), same chips seen in a asynchronous data taking spanning 40 $kClk \times 25\ ns = 1\ ms$ when tested at 10 kHz pulse repetition rate (right).

chips, channels $0-15$ of $FASP_0$ and $16-31$ of $FASP_1$ respectively, are registered as function of DAQ clocking, for an interval of 6 $clk \times 25\ ns$. Several particularities can be seen here as *e.g.* first three channel of $FASP_0$ are not connected, there is no pairing between chips as channels 15 and 31 show only half the amplitude ($\approx$ 1300 ADU) wrt the rest ($\approx$ 2100 ADU) and that one can measure the FASP walk if both pulse injection time and CS signal are compared. In the right figure an interval of 1 ms is shown, time being expressed in 25 ns clocks. The horizontal red line mark the boundary, in the FEE channel space, between the two chips. The vertical lines represent the channel-wise signals. One can see that all FEE channels in one FASP are synchronous on this time scale but the two chips are off by a phase of $\approx 50\ \mu s$. It is also seen that after some repetitions the pulses are no longer registered in the acquisition, for both chips, which might indicate *e.g.* data back-pressure in the DAQ (see section 4.2). Of course this is an example of some real chips on a test board. On the CBM DAQ such calibration procedure should be performed automatically by the FEE to provide a fast overview of the status of more than $100k$ channels. The FEE-DCS should also run actions like either re-starting a broken FEE unit or, if the error persists, reporting it via DCS for being properly considered during reconstruction.

If the synchronicity of FEE channels is the mandatory condition for free-running acquisition, the uniformity of characteristic response for all FEE channels is instrumental for the quality of reconstructed observable. In Fig. 5.3.3, once the synchronicity is established, a 10 min run

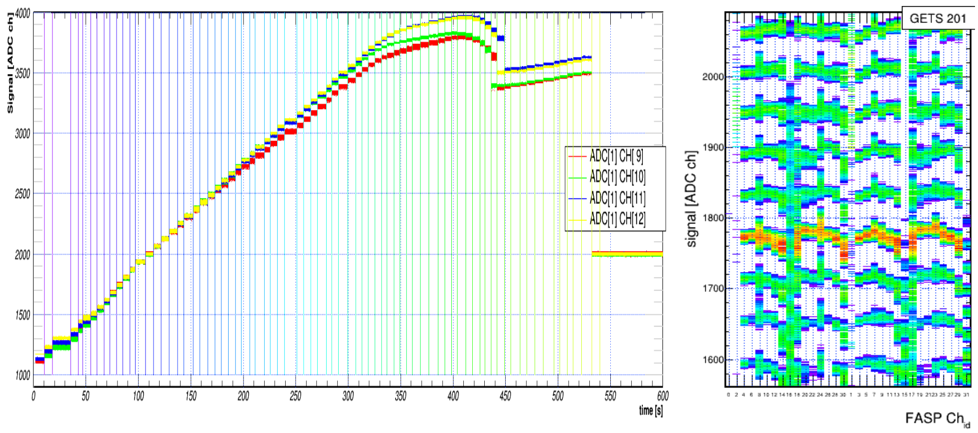

Figure 5.3.3: Calibrating signal amplitude by injecting charge pulses through the anode electrode; time dependence of signals from four FASP channels for a set of equally spaced calibration pulses (left) and the time integrated response of two FASP chips response to a set of equally spaced calibration pulses (right).

is shown on which, having the detectors in operating condition (HV, gas, etc.) and for a fixed pulse repetition frequency, a scan of the FEE dynamic range is performed. For each channel, a response characteristic, as in the left figure, is registered by running the pulse amplitude through a set of equally spaced values. The data can be used to derive channel gains (see Fig. 4.1.6 right in section 4.1.2) or, by integrating over time, a representation as shown in the right panel. From such representation one can derive gain corrections to equalize channels responses to same inputs. A supplementary information obtained from such procedure is the *intrinsic noise per FEE channel* which is the width of a Gauss fit to the signal distribution for each input and channel. Such uncertainty estimator is further used in situation like energy reconstruction (see Fig. 5.2.4, section 5.2.3).

x-y position calibration using 2D masks

The reconstructed position of the TRD suffers systematic effects as discussed in section 5.2.2. The method used there was to estimate and parametrize them wrt MC. Here we will present a complementary method based on full data taking with absolute reference.

In Fig. 5.3.4 a qualitative description of an experimental setup for the mask-calibration method is shown. The detector, for which the read-out structure - triangular pads (black) and anode wires (red), shown in the background, is irradiated with a X-rays source[19]. On the entrance window, a Cu foil with precise drilled holes is positioned such that the active area is partially illuminated through the openings. The particles yield is registered over the whole detection are with respect to the detection elements and the reconstructed transition lines between shaded and opened areas are compared with their geometrical counterparts. From the width of the transition between open and shadow the position resolution can be derived and from the distortions, the systematic effects.

The example shown in Fig. 5.3.4 is meant only as suggestion. In a production ready implementation the mask should contain rectangular openings precisely positioned wrt. the read-out elements, covering the whole detection area and the irradiation has to be done uniformly over the entire surface. In a complex tracking environment, position alignment between different detection systems can be done by observing deviations in places where one system is prone to a systematic effect while the other not, *e.g.* sensor boundary in STS propagated to the middle of a TRD chamber (with proper selections). For such an application, the advantage of the

[19] Here a collimated $55^{F}e$ source. We have also tested uncollimated X-rays from tubes.

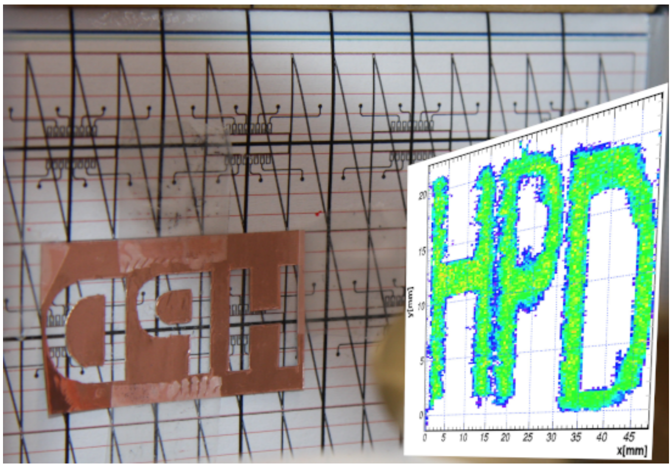

Figure 5.3.4: Qualitative description of the mask-calibration method for position reconstruction; the detection elements (triangular pads and anode wires - background), the Cu mask with "H", "P" and "D" shaped holes positioned on the detector and finally the result of position reconstruction algorithm (front).

mask-calibration method consists in assuring large ($57 \times 57\ cm^2$) areas free of internal position systematic effects.

For the following performance reports all calibrations implied in this sections were applied.

5.3.2 Energy Resolution

The study of the energy resolution is traditionally performed for TRD using the ^{55}Fe X-ray source with the $Ar + CO_2$ gas mixture. The advantages of this procedure consists in the fact that it provides two energy lines situated close to two important operation points of the TRD, the $E_{MIP} = (0.8 \cdot 2.53\ keV/cm + 0.2 \cdot 3.35\ keV/cm) \times 1.2\ cm = 3.23\ keV$ and the TR energy deposits ($\epsilon_{TR} > 5\ keV$). The ^{55}Fe emits two X-ray fluorescence lines, $K_\alpha = 5.895\ keV$ (89 %) and $K_\beta = 6.492\ keV$ (11 %) by electron capture. These two values are sampling nicely the low energy region of the TR absorption spectrum (see Fig. 5.3.5 and 5.3.7). If not absorbed by the entrance window, the X-ray photon can potentially produce a photo-electric (PE) effect on the Ar atom releasing a free electron of energy $E^{PE} = (E_\gamma - E_K)$ where $E_K = 3.2\ keV$, the binding energy of the K-shell. Thus, $E_\alpha^{PE} = 2.695\ keV$ and $E_\beta^{PE} = 3.292\ keV$ can be amplified and finally reconstructed by the TRD. The peak generated by this prompt photon is referred as the *"Escape Peak"*. The Ar atom, left with a hole on the K-shell can de-excite by fluorescence emission (12 %) or Auger electron (88 %). The energy of the second electron freed in the gas is $E_A = E_K - 2E_L$ where $E_L = 0.25\ keV$ the binding energy of the L-shell. Thus $E_A = 2.7\ keV$ is added the the prompt $E_{p/e}$ generating a second peak, the *"Main Peak"*, which for the two lines of ^{55}Fe have the values $E_\alpha^{PE+A} = 5.395\ keV$ and $E_\beta^{PE+A} = 5.992\ keV$ respectively. In order to estimate the energy resolution the energy spectrum is measured and calibrated, the four peaks are identified and their shape is Gauss parameterized.

In Fig. 5.3.5 left the method described above was applied for the measured spectrum obtained with the TRD-2D system, operated by the GETS steered DAQ. The FEE was implemented using FASP-v02 which had to be operated with some higher threshold which also asked for higher U_{anode} on the detector wrt default values. In order to assure full containment of induced charge in one pad row a full position reconstruction was performed before and only clusters amplified by the central anode wires (indices 4 an 5) where selected. The measured spectrum was deconvoluted using a sum of four Gauss models anchored to the values of E_{dep} discussed

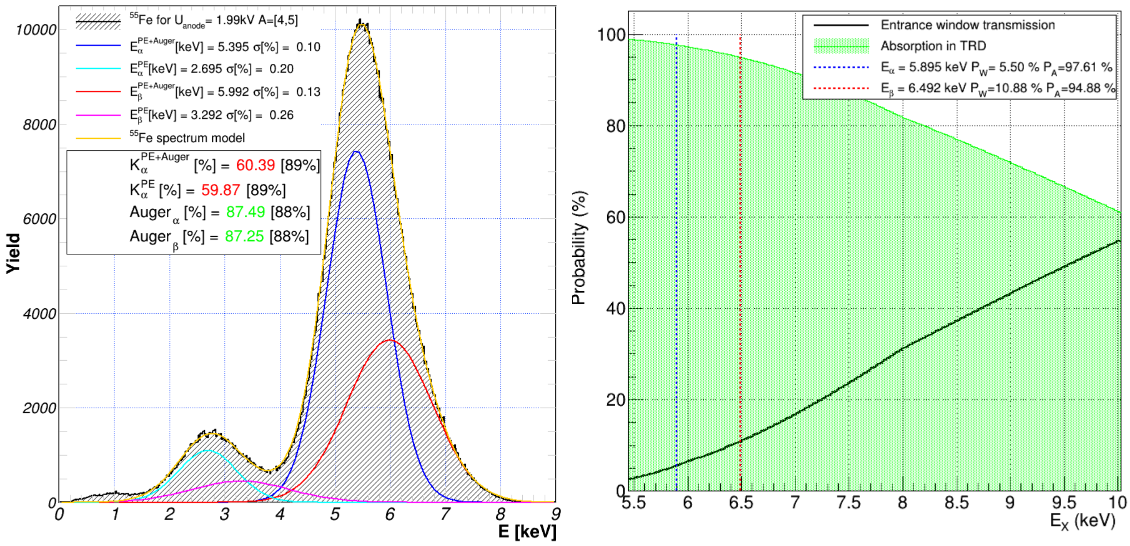

Figure 5.3.5: Detailed analysis of measured ^{55}Fe spectrum against atomic data together with various yield ratios which were derived from it (left) and the transmission/absorption probabilities of the TRD detector used to estimate the spectrum wrt the K_α and K_β lines of ^{55}Fe (right).

above (see also figure legend). The sum of all spectral contributions is referred as the "^{55}Fe *spectrum model*" (yellow in figure) and it describes well the measurement. The output of the model are the yields and width of each spectral component. From the yield components we can compute two relative components: the relative yield of α (or β) lines (theoretical value 89 %) and the probability of Auger electron emission (theoretical value 88 %). For the last yield, we have calculated for both α and β lines, the ration of Main to Escape peaks and the result reproduce the theoretical value. On the other hand, when calculating the K_α probability, for both type of atomic processes, PE only and $PE + Auger$, the value ≈ 60 % (red text in figure) is obtained for both, which shows a major deficit wrt the theoretical value. In order to explain the difference, the entrance window transmission and the gas absorption has to be considered. In Fig. 5.3.5 right the probability of the two phenomena are calculated based on the material budget of the TRD detector used for this measurements. The K_α and K_β lines of ^{55}Fe are also marked on the figure. Combining the initial probability with detector effects the effective yield of the K_α is reduced to 80 %, still not matching the data but indicating the trend. The difference might come from manufacturing effects on the window not captured by the model. Such correlation show that precise measurements of the reference spectrum with TRD-2D can be used as tools on the window absorption for production QA.

The actual energy resolution is captured in the second Gauss model parameter (see the *sigma* values in Fig. 5.3.5 left). It is shown that the resolution improves from values of $\approx$ 20 % around 3 keV to values of 10 % at 6 keV. Testing at higher values (10 and 12 keV) with the X-rays tube (see section 5.4) are also possible.

The energy resolution depends on both the detector operation conditions and FEE settings. Additionally, for the TRD-2D, it is also possible to show a dependence on the anode wire (see Fig. 5.2.5). All these conditions play a role on the cluster size and its symmetry and, hence, on energy reconstruction quality. In Fig. 5.3.6 we show, for a scan of anode voltage, the modifications in the energy resolution and overall shape of the ^{55}Fe spectrum. For each U_A in the figure the spectral decomposition is given in terms of cluster size and symmetry. The U_A varies from 1.7 kV to 2.0 kV, in non-equidistant steps, while the cluster type is represented as "Xn" with X the pairing type for the maximum signal being T - tilt or R - rectangle and n the total number of signals in the cluster. For all cases, only anode indices 4 and 5 were selected to assure full containment

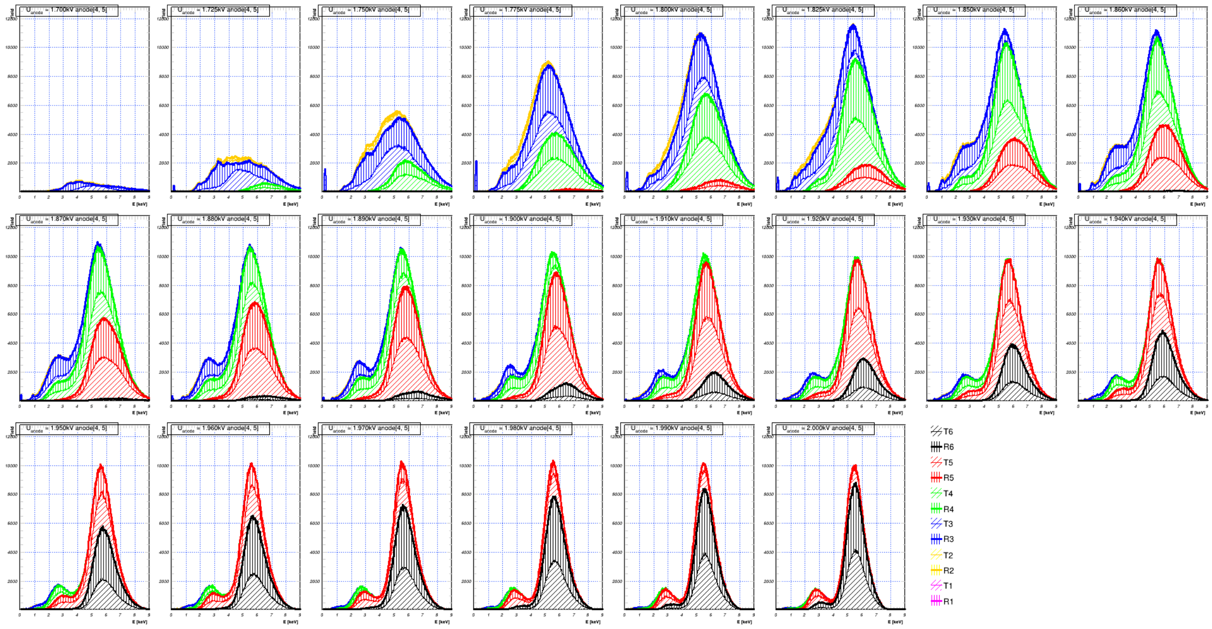

Figure 5.3.6: Reconstructed ^{55}Fe energy deposits for varying U_{anode} emphasizing the cluster size distribution for each case (see legend); in all cases only fully single row clusters are considered by selecting only anode wires index 4 and 5.

of charge in a single-row cluster. The morphing of the spectrum obtained at high U_A until all features are lost at low U_A can be directly correlated to the cluster size content and thus with the information content/cluster. It is thus demonstrated that, the higher the cluster-size, the better the energy resolution and efficiency is obtained. Such goal can be achieved by a combination of increasing U_A and lowering FEE signal thresholds. Additionally, wrt. the rate capabilities, a larger cluster size implies higher cluster overlaps (see section 5.4.1) and higher data loads on the DAQ (see section 4.2). Thus, the system tuning depends on the measurement requirements, the best system performances will never be reached simultaneously in the experiment. The TRD-2D can be tuned to accommodate different physics programs.

Transition radiation spectrum

On top of the general implications for the quality of the measurements discussed above, the energy resolution is directly linked to the physics of electron enhancement by TR generation and detection. The TR yield, interacting in the active zone, depends on radiator, entrance window and active zone depth. In the TRD-2D design we follow the same parameters as in the TDR with the exception of the entrance window (see section 3.2.1) which is supported by a robust *honeycomb* structure. The implications on the TR yield has been studied using the same modeling tools as used for the TDR version.

In Fig. 5.3.7 a comparison is performed between the TR yield of the TDR solution and the proposed TRD-2D. Four spectra are being shown in each case: the spectrum generated at the wall of the radiator (same in both cases), the spectrum passing the entrance window and the TR photons which are absorbed/escape detection. The main difference between the two chamber designs is in the entrance window where almost one low energy photon is lost in the case of TRD-2D. Since more than two photons are crossing the gas without interaction only 0.8 *photons* are absorbed in average per electron which represent a loss of 34 % wrt the TDR design. The mean energy of these photons is $< \epsilon_{TR} > \approx 14\ keV$ with a most probable value $Mpv(\epsilon_{TR}) \approx 10\ keV$. Nevertheless, in order to be actually useful for PID, the TR signal has

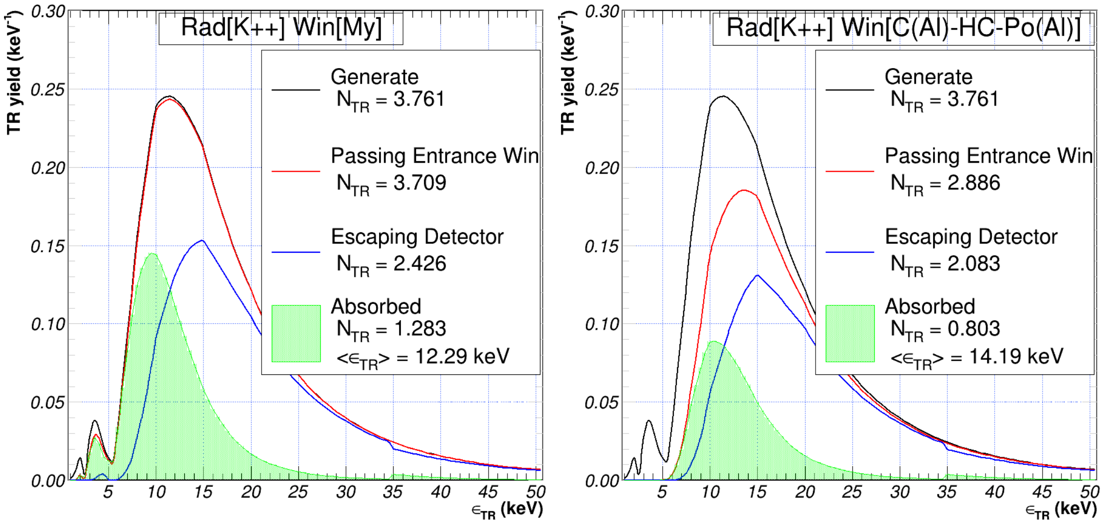

Figure 5.3.7: The simulated TR spectrum in the case of the TDR chamber structure (left) and for the TRD-2D prototype (right); various components are emphasized while the spectrum absorbed in the chamber ($XeCO_2$ gas mixture) is displayed in green.

to be processed by FEE. In these respect there are two issues considered in the FASP design for *actually measuring all photons which are detected*: the shaping time and dynamic range. Firstly, as the TR signals comes later than the ionization (see Fig. 5.1.1) it is important that the two signals should be integrated. For this particular reason the shaping time of FASP was enlarged to 100 ns with the draw-back of making the FEE response slower. Secondly, we showed that the energy range in $ArCO_2$ starts at $E_{MIP} \approx 3\ keV$ up to $E_{FP}^{e^\pm} + \Delta\epsilon_{TR} \approx 25\ keV$ with $E_{FP}^{e^\pm} \approx 1.5 \cdot E_{MIP}$ is the energy deposited by electrons on the Fermi Plateau and $\Delta\epsilon_{TR} \approx 20\ keV$ a minimum range for the TR detection. Similarly for $XeCO_2$ mixtures the energy range should cover the interval $7.40\ - 31\ keV$. Correlating this energy range information with the energy resolution deprecation for low E_{dep} shown in Fig. 5.3.5 left result in a series of constrains on the gas gain such that E_{dep}^{π} is not too much cut and enlarged by low efficiency and resolution and $e^{\pm} + TR$ spectrum does not exceed the FEE dynamic range. Such considerations are mandatory when analyzing the FEE performance as they are presented in Fig. 4.1.6 right.

5.3.3 Position Resolution

In section 5.2.2, the method for x-y TRD-2D position reconstruction was first introduced. We have shown in Fig. 5.2.2 that it is possible to identify the anode wire where the charge is amplified. If the residuals are represented as function of the MC distance to the closest anode wire, the representation from Fig. 5.3.8 is produced.

In Fig. 5.3.8 left the residuals of the reconstructed y position wrt MC are represented as function of the closest anode wire on the span of 3 mm *i.e.* one amplification cell. Values for the mean and width of the Δy distribution are added with red closed/open symbols. The image is symmetric wrt the anode wire position and presents a three distinct regions. The central region of $\approx 1\ mm$ with residual distributions of high width is populated by tracks which are amplified by single-wires. The y position resolution in this case is $\approx 900\ \mu m$ close to the theoretical limit of $3\ mm/\sqrt{12}$ given by the anode wire pitch. On the sides there are regions where, due to track inclination, two amplifications cells are activated. The residual width is here of $\approx 200\ \mu m$ but systematic effects are large as there is no reconstructed information to distinguish the distance from cell boundary. At the cell boundary, a 1D profile is presented in Fig. 5.3.8 right, which is

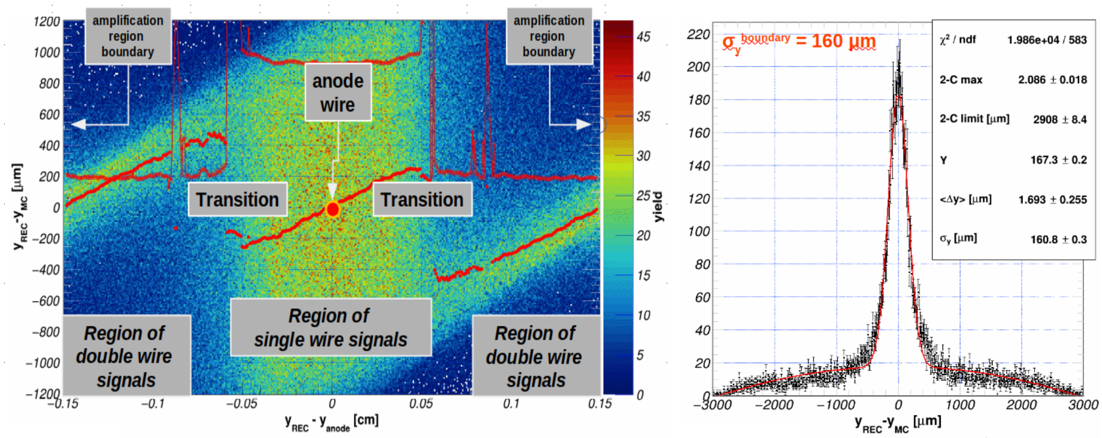

Figure 5.3.8: Y position reconstruction residual distribution wrt. MC as function of the geometrical distance to the anode wire (left) and the 1D projection of y residuals for the region of amplification cell boundary emphasizing the position resolution for this case.

fitted with the sum of two Gauss models. The 160 μm width Gauss models the tracks which have a proportional contribution of charge in two adjacent amplification cells. A second contribution of 3 mm width describe a global background (2-C limit) of miss-identified anode indexes. Similar results or better are obtained for the coordinate x.

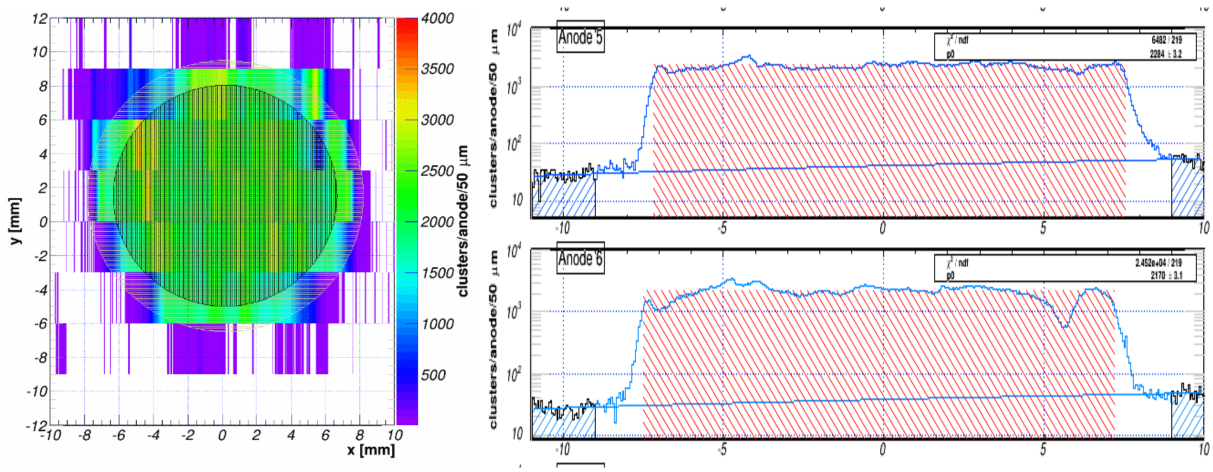

Figure 5.3.9: Experimental estimation of x position resolution using the mask-calibration method (see Fig. 5.3.4) for a circular mask of 13 mm diameter (left) and two 1D projection for the most central anodes indices 5 and 6 (right).

More reliable than residuals wrt. MC is the method of mask-calibration (see section 5.3.1). This time we have used during irradiation a Cu screen with a 13 mm diameter circular opening (see black hashed circle in Fig. 5.3.9 left). From the geometrical setup we noticed that the image of the circular opening at the level of the anode wire plane was actually enlarged, corresponding to the light colored larger circle in the same figure. For a binning of 50 μm in the x direction we derive the yield distributions for each anode wire (corresponding to the 3 mm binning in the y direction from the figure). In Fig. 5.3.9 right we show the 1D projection for central anodes indices 5 and 6. In such projections we can distinguish three zones: the central one, hatched in red which correspond to no screening and the two on the sides which correspond to full screening. For all these three regions a flat distribution is expected. The regions of transition can in this case be used as x position resolution estimator by computing the $\partial Y/\partial x$, with Y the measured yield and x the reconstructed position. Deviations from the theoretical expectations measured at this level are accounting for systematic effects which adds to those produced by incomplete charge collection (see section 5.2.2) and are produced by, still to be accounted, differences between FEE channels. Thus, the mask-calibration method is complementary to the MC method and it uses the unique 2D position measurement capabilities of the TRD-2D to produced unbiased position reconstruction information for the CBM tracking.

5.4 High Particle Rate Capabilities

The most challenging feature of the CBM experiment and, hence, of all sub-systems participating to it is the high particle rate which has to be measured. For the inner modules of the TRD wall, for which the TRD-2D is proposed as alternative, the average particle rate in conditions of top interaction rates on target is $\approx 100\ kHz/cm^2$. Given a mean cluster size of ≈ 5 for single-row and 6 for cross-row clusters and a ratio between them of 6 : 3 (see Fig. 5.2.3) the signal rate per channel, if all particle would be detected independently would be above $\approx 0.5\ MHz$, *i.e* an average spacing of less than 2 μs between consecutive signal per FASP channel. In reality, particle fluctuations wrt time and space create large discrepancies against this theoretical limit. In order to accommodate such variations the FASP was designed and successfully tested with regular pulses up to 1.2 MHz which should allow for random variations in instant rate and particle multiplicities per unit area.

There are three main questions that we want to answer wrt the response of the system to high incident rates namely :

- the *actual signal rate per channel and how this is transferred to the analysis cluster*,
- the *reconstruct-able particle rate* and,
- the *true incident rate*.

Particle rates needed to test the system, were accessed at CERN SPS with partial success (see section 2.3.1). Therefore, more controllable sources were searched for reference. We have selected X-rays tubes with acceleration voltages of up to $U_X = 50\ kV$ which produce an energy spectrum spanning from $2-50\ keV$. Using the Au targets, several outstanding peaks are available at: 8.5 keV; 9.7 keV (L_α); 11.5 keV (L_β); 13.4 keV (L_γ). Larger values for the energy deposit scanning the targeted dynamic range (see section 5.3.2) for the TRD-2D application can be obtained using an Ag target cathode on the tube. The photon flux is modulated by the current intensity I_X, and is limited by the maximum power of 4 W supported by the tube.

We have tested the free-running system in various configurations from Pb-Pb beam interactions at CERN-SPS to X-rays tube irradiation in the laboratory. In top row of Fig. 5.4.1 two examples of instant rates measured per FEE channel are presented. We have defined the *instant rate* as $r(t) = 1/(t - t_0)$ where t is the time of the current signal and the t_0 is the time of the previous signal measured on the same FEE channel. In the left figure we present the spectrum of $r(t)$ for the CERN-SPS run. Different ranges of data frequencies were identified wrt machine working cycle to show the consistency of data taking over large time spans of our DAQ[20]. This measurement demonstrated that, in a real experiment, we can populate the frequency domain of FASP up to 1.5 MHz without entering into limitations. A different view on system capabilities was done by sustained X-rays irradiation at constant intensity/rate and observing the response of the system under such stress. In Fig. 5.4.1 (top/right) the time dependence of instant rate for several channels affected differently by the irradiation is shown. One can see in the figure the situation where the blue and red FEE channels enter in data back-pressure while magenta continue sending data. It can be seen that the system recovers after the data is transferred to storage and the periods of black-out are correctly accounted for in the DAQ (shaded regions).

[20]The DAQ used in this measurement campaign was a proof-of-principle version which although contained all principles described in section 4.2 was limited in the number of FEE channels and CBM integration.

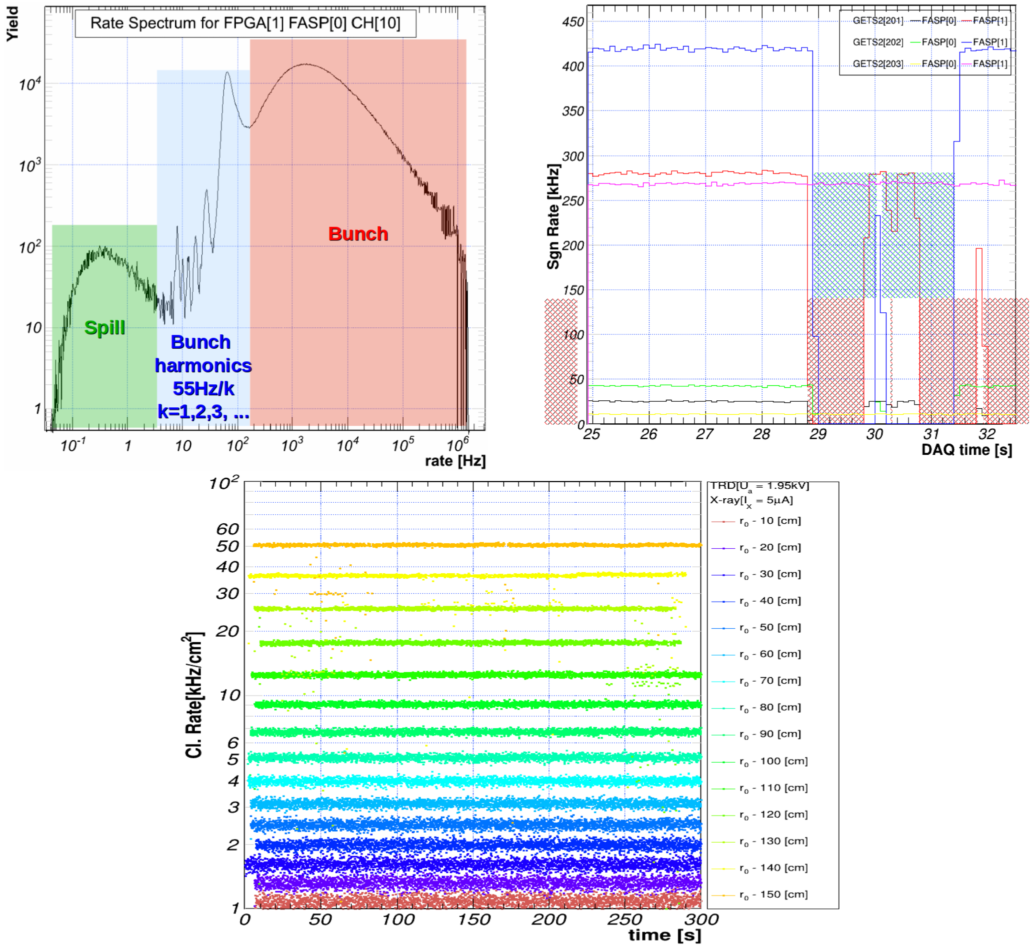

Figure 5.4.1: Estimations of the *signal rate/FEE channel* (upper row), measured in a 150 $AGeV/c$ PB-beam on Pb target (left) and using X-rays tube respectively (right) and reconstructed *single-row cluster rate/*cm^2/s (bottom) for X-rays tube irradiation of the TRD-2D system.

The next level of integration is the reconstruction of single-row cluster counting. In Fig. 5.4.1 (bottom) results on instant cluster rate for X-rays illumination are shown for various setups (see next section) for continuous 5 min runs. We have demonstrated that from the DAQ perspective high rates of reconstructed data and rates of at least half the target rate (50 kHz/cm^2). Of course data back-pressure may stop the measurement (see runs above 20 kHz/cm^2) but the system recovers (see section 4.2).

5.4.1 Rate estimation and consequences

As is the case with any reconstructed observable, the counting of incident particles detected by the TRD-2D system, is and estimator of the actual rate. To asses the quality of such estimator one would need the knowledge of the incident rate. An un-biased method to estimate such true rate is for the X-rays irradiation scenario. Unfortunately there is no direct relation between I_X and $dN/d\Omega$ of emitted photons but there is a relative calibration available by observing the scaling of the photon intensity with r, the distance from the tube to the detector for fixed setup on the tube/detector. The set of measurements at various distances are shown in Fig. 5.4.1 (bottom) from the stability point of view and as function of distance to the detector in Fig. 5.4.2.

In a first approximation the variation of intensity with distance is described by the simple

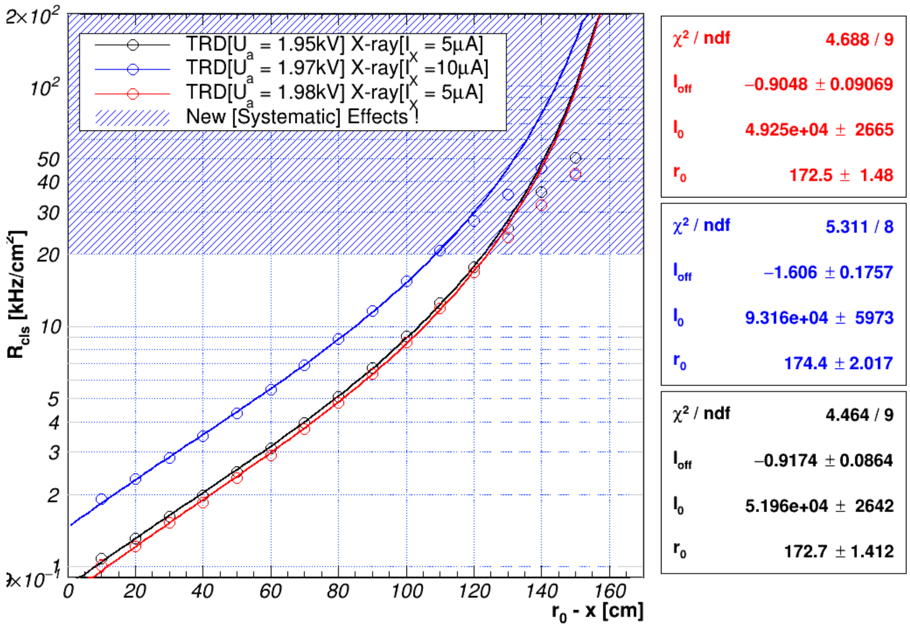

Figure 5.4.2: Controlling the reconstructed cluster rate for an X-ray tube irradiation against the geometry of the setup; symbols represent measured estimators and continuous lines the model.

relation:

$$R(r) = I_A(r) = I_{off} + I_0 * A_0/r^2 \tag{36}$$

where I_{off}, I_0 and A_0 are constants which describe the effective intensity and detection area of the setup, and are parameters to be determined from the fit. In Fig. 5.4.2 three different setups were tested and the measurements were reconstructed up to the level of position reconstruction of single-row clusters. For these setups we have selected various anode voltage U_A and tube intensity I_X as can be seen in figure for different color codes. An area of several cm^2 was selected corresponding to the central channels of a FASP chip. In order to control systematic effects, the following was performed $r \to r_0 - x$ where r_0 is a reference distance far from the detector and x is the difference from it. The change accounts for the uncertainty of the effective radial distance between the cathode Au foil and the cluster inside the 1.2 cm active gas. In such a way, the distance is determined as a fit parameter from all measurements in a data set and confirms the quality of the data. In the figure, the parameters of the fit for each setup are shown in the corresponding color code. The r_0 parameter is obtained for all three setups around 173 cm which confirm the experimental fact of starting all three measurements from the same reference (not accounting the mechanical positioning errors). Having this confirmation established we further divide the measured space in two regions : the region below 20 kHz/cm^2 of large distances where the model describe the data and the region above it where the two diverge. For the blue shaded area we need to find the hypothesis implied in the model which does not hold anymore.

In Fig. 5.4.3 we have tried to disentangle possible hypothesis which might explain the departure of the reconstructed rate from the model. In the top figure we assume that the dependence from Eq. 36 is no longer valid at small radial distances (due to aperture and finite size of detection area). We have shown that the r scaling can not explain the data trend as in this representation the departure from model happens at different r for each setup although they are similar from the geometrical point of view.

In Fig. 5.4.3 bottom we show the residual rate scaling with model rate. The trends observed for all tree setups under test seem to match suggesting that the rate itself is the factor which makes the measurement diverge. Above a rate of 25 kHz/cm^2 incident X-rays photons, independently

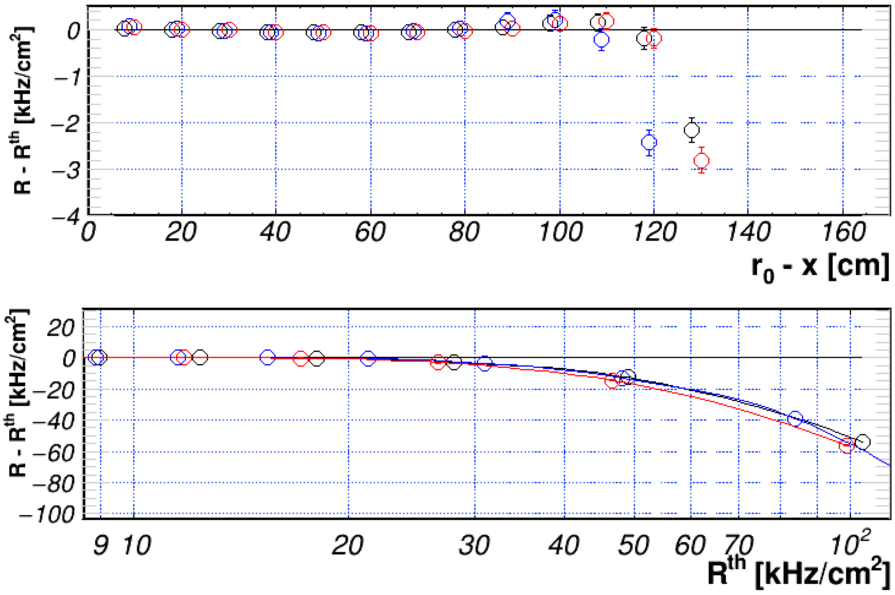

Figure 5.4.3: Correlation of the measurement to model cluster rate residuals as a function of the model systematic (top) and rate respectively (bottom).

of the U_A and I_X, the trend is the same for all setups. Such independence suggest that neither the detector (U_A) nor the X-rays tube (I_X) have systematic effects related to this limit. On the other hand, the intrinsic hypothesis of the *single-row clusters count* as estimator for the incident rate may not hold anymore. There are two implication to this observation:

- if we correlate with the results from Fig. 5.4.1 bottom we see that clusters start missing above rates of 20 kHz/cm^2 due to data back-pressure.

- if we correlate with the clusters topology (size, charge-time profile, etc.), one would identify less incident photons producing well space-time separated signal clusters. The observation point to the need of more refined reconstruction techniques for particles out of signal clusters such as de-convolutions[21].

Thus, the operation of the TRD system at high rates is a challenging measurement. The interpretation of the results (see Fig. 5.4.2) shows already the many-faced implications on the full system - from detection unit to the data reconstruction - of operating within the CBM environment. We have nevertheless demonstrated that, the TRD-2D system as described here, can be controlled and finely tuned to achieve the physics goals put forward in section 1. Finally the sum of detector, FEE, DAQ and reconstruction/calibration algorithms contributions is inseparable at high rates.

[21] Such improvements were tested already and the implementation on data is in progress.

6 Chamber Production

(*Mariana Petris*)

The inner zone of the CBM-TRD consists of 40 individual readout chambers which should be assembled, tested and integrated in the TRD subdetector of the CBM experimental setup. In addition, a number of 4 spare chambers will be considered. For the construction of these detectors, the Detector Laboratory of the Hadron Physics Department of "Horia Hulubei" National Institute of Physics and Nuclear Engineering (HPD/IFIN-HH) will be used. This infrastructure is divided in a clean room area for chamber assembling and a testing area for the chamber commissioning.

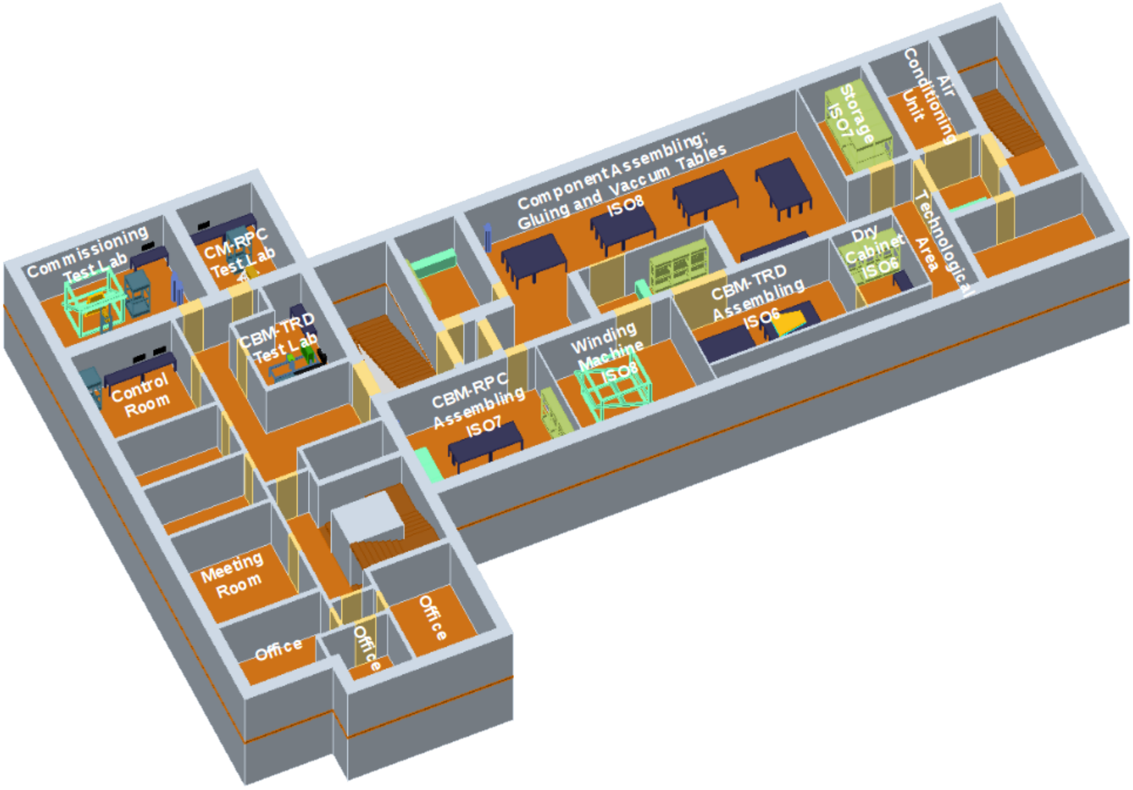

Figure 6.0.1: A sketch of the HPD detector production area.

A 3D sketch of the 6 clean rooms (2 x ISO6, 2 x ISO7 and 2 x ISO8), 3 testing laboratories (1 x CBM TRD tests, 1 x CBM RPC tests and 1 chamber/module commissioning tests) and 1 data acquisition control room is shown in Fig. 6.0.1. Besides these, 2 electronics laboratories (located at the next floor) are dedicated to the assembling and testing of the front-end chips and detector specific integrated electronic boards.

From the construction point of view, each assembled chamber can be divided in four major sub-assembled components: chamber body, entrance window, multiwire electrodes and readout pad plane. The most part of the needed mechanical (i.e. ledges, Al profiles, etc.) and electronics (readout pad-plane, ASIC production, readout boards, etc.) components will be produced by cooperation with industrial companies in order to cope with the scheduled timelines.

6.1 ROC - Experience, Infrastructure and Manpower

The HPD/IFIN-HH Detector Laboratory was initially set up for the assembling and testing of 130 ROCs (Readout Chambers) for the ALICE-TRD subsystem and provides all the necessary equipment and tools. Later on, this infrastructure was extended and upgraded, being used for the assembling and testing of 20 OROCs (Outer ROCs) in the GEM technology for the upgrade of the ALICE-TPC subdetector. An intense prototyping activity for the CBM TOF and TRD subsystems has been developed in parallel, using the same infrastructure.

For the construction and tests of the CBM-TRD readout chambers of the inner zone of the four TRD layers, the following infrastructure and main equipments are available:

1. **Clean rooms for assembling and intermediate testing**
2. **Winding machine**
3. **Wire tension and position measurement device**
4. **Gluing, vaccuum and optical tables**
5. **Carrier for transport of the wire frames**
6. **2 X-ray tubes and ^{55}Fe X-ray source**
7. **Test gas system**
8. **Final testing laboratories**
9. **Storage room**

A ISO8 clean room of 110 m^2 equipped with 2 gluing tables, 2 vacuum tables (mechanical precision better than few tens microns) and an optical table will be used for the chamber body, entrance window and readout pad plane assembling. The winding machine is located in a second ISO8 clean room of 26 m^2 together with the carrier for the transport of the wired frames. In a 28 m^2 ISO6 clean room, the wire planes will be mounted and glued on the chamber body, the mechanical wire tension and position after gluing will be measured and the chamber will be finally closed with the pad plane electrode. A third ISO8 clean room of 22 m^2 can be used for the temporary storage of the finally assembled and tested TRD chambers. A dedicated TRD laboratory (with a specific test stand) and a commissioning laboratory (where a 2D scan of the gain uniformity and a long-term exposure to high X-ray flux tests can be performed) are available for the final chamber testing.

The estimated available human resources in HPD/IFIN-HH (2021 year) for the chamber construction, electronics integration and module assembling are presented in table 6.1.1 in equivalent FTEs:

Table 6.1.1: Manpower.

HPD/IFIN-HH	Phys.	Electr. Eng.	Mech. Eng.	Technicians	Msc/PhD
FTEs	2	1.4	1	1.6	0.5/1.5

6.2 ROC - Timeline and Costs

Taking into consideration the estimation of the available man power and the most time consuming steps in the chamber assembling among which those involving the hardening of the glue are an important issue, a realistic estimation of 15 working days per 2 chambers is considered in the timeline for the assembling and full testing. The schedule presented in table 6.2.1 takes into consideration the current planning of the readiness of the CBM cave for detector installation and the correlation with the detector installation plan of the CBM experiment.

Table 6.2.1: List of milestones for TRD-2D.

Milestone	Date
Inner modules EDR	15.09.2021
Inner modules PRR	20.02.2022
Start module production	01.07.2022
All chambers built	30.06.2024

For 250 working days per year, one year and three months is an estimated time for the production of the 40 chambers of the inner zone. However, taking into consideration the time needed for the procurement of the detector components and materials, the preparation for the series production and the necessary contingency, a two years chamber production timeline is a realistic estimation. According with the presented schedule, in middle of 2024 all chambers should be assembled and tested. According to the installation plan, all chambers will be integrated in the CBM-TRD subdetector by the end of 2024. The cost estimates presented in table 6.2.2

Table 6.2.2: Single readout chamber component costs.

Item	Costs (Euro)
Honeycomb 23 mm thickness	841
Honeycomb 10 mm thickness	300
Pad plane	415
Screening PCB plate	45
FR4 ledges	675
Al frame	460
Gas inlet/outlet	60
Anode wire	30
Cathode wire	30
Signal cables 16-pin	200
Araldite	136
Al Kapton foil	30
Holding device	95
Clamp	95
Consumables	58
Total	3470
Sum 40 chambers	138800

including detector materials, components and their manufacture in industrial companies. They do not include the costs for the manpower and infrastructure maintenance which will be used for the chamber assembling in HPD/IFIN-HH. They are based on the latest prices of the components and materials used in the prototyping phase.

6.3 FEE - Timeline and Costs

The design and production of the FASP ASIC and FEB is conducted by the HPD/IFIN-HH and their intermediate and final testing will be carried out in the two electronics laboratories of HPD/IFN-HH.

The timeline for the detector specific readout electronics is detailed in table 6.3.1, in close connection with the same considerations as for the chamber schedule, mentioned in section 6.2.

Table 6.3.1: List of milestones for TRD-2D FEE.

Milestone	Date
FEB PRR	30.06.2021
Start FEB production	01.01.2023
End FEB production	30.06.2024

Each chamber will be equipped with a number of 15 front-end boards (FEB = FASPRO+GETS+ADC) including 180 FASP ASICs which will process the signals delivered by the readout pads. A total number of 600 FEBs includes 7,200 ASICs for processing the signals of the 115,200 readout channels of the inner zone. A 10% spares of ASICs and FEBs have to be considered in the final costs, as it is further detailed in section 6.4. The costs of the 25 CRI bords used in the data transfer as well as the associated optical connections have to be included. The costs estimation for the detector specific readout electronics presented in table 6.3.2 considers the prices from the prototyping phase:

Table 6.3.2: Readout electronics costs.

Item	Costs (Euro)
FASP ASICs	100,000
FEBs (FASPRO+GETS+ADC)	615,000
Optical connections	10,000
CRI	275,000
Total (without spares)	1,000,000

The on-going R&D activity for the front-end electronics is continuing with the integration of the ADC in the FASP ASIC. Further higher integration of the ADCs in the FASP chip boards could lead to a important costs reduction as it is shown in table 6.3.3.

Table 6.3.3: Readout electronics costs.

Item	Costs (Euro)
FASP ASICs +ADCs	100,000
FEB (FASPRO+GETS)	396,000
Optical connections	10,000
CRI	275,000
Total (without spares)	781,000

Considering the cost estimations from table 6.3.3 and the total number of readout channels, a 6.78 Euro/channel is obtained.

6.4 Financial Details

Based on the cost estimations presented in section 6.2 and section 6.3, the core costs for the inner zone of the CBM-TRD are detailed further. In table 6.4.1 and table 6.4.2 there were considered the core costs for the two scenarios of the costs for the readout electronics. However, we should stress here that there are additional costs, i.e. manpower for assembling of the chambers in HPD/IFIN-HH and infrastructure maintanance, transport equipment (i.e.boxes) and chamber transport to FAIR, installation manpower which are not included in these estimations.

Table 6.4.1: CBM-TRD inner zone core costs.

Item	Costs (Euro)
40 Readout Chambers	138,800
Spare 4 Readout Chambers	13,880
Readout Electronics	1,000,000
Spare 10% Readout Electronics	71,500
Total	1,224,180

Table 6.4.2: CBM-TRD inner zone core costs.

Item	Costs (Euro)
40 Readout Chambers	138,800
Spare 4 Readout Chambers	13,880
Readout Electronics	781,000
Spare 10% Readout Electronics	49,600
Total	983,280

The funding of the production of the TRD-2D chambers and associated readout electronics for the TRD inner zone is currently spilt in two parts, according with the 8^{th} CBM Collaboration Resources Review Board (RRB) from November 2018:

- an in-kind contract between FAIR, IFIN-HH and Romania funding agency/ministry of 752 kEuro at the level of 2005 year or of 1,080 kEURO at the level of 2018 year,
- "other resources" of 482 kEuro (2005)/693 kEuro (2018).

While the founding through the in-kind contract is secured as soon as this contract will be signed, for the "other resources" funding, additional resources need to be identified in the near future in close collaboration with the Romanian authorities and FAIR management.

A The CBM Collaboration

A. Adler[1], A. Agarwal[2], K. Agarwal[3], Z. Ahammed[2], A. Ahmad[4], N. Ahmad[5], A. Akindinov[6], P. Akishin[7], V. Akishina[8,9], M. Al-Turany[9], I. Alekseev[6], E. Alexandrov[7], I. Alexandrov[7], A. Andronic[10], H. Appelshäuser[8], D. Argintaru[11], B. Arnoldi-Meadows[8], E. Atkin[12], M.D. Azmi[5], V. Baban[11], S. Bähr[13], M. Bajdel[9], G. Balassa[14], M. Balzer[13], N. Baranova[15], M. Baszczyk[16], E. Bechtel[8], J. Becker[13], K.-H. Becker[17], M. Becker[18], S. Belogurov[7,12], A. Belousov[19], A. Bercuci[20], R. Berendes[10], D. Bertini[9], O. Bertini[9], M. Beyer[18], O. Bezshyyko[21], P.P. Bhaduri[2], A. Bhasin[22], S.A. Bhat[4], W.A. Bhat[4], B. Bhattacharjee[23], A. Bhattacharyya[24], S. Biswas[25], T. Blank[13], D. Blau[26,12], C. Blume[8,9], D. Bonaventura[10], J. Brzychczyk[27], T. Bus[8], A. Bychkov[28], M. Cãlin[11], M. Caselle[13], A. Chakrabarti[24], P. Chaloupka[29], S. Chatterjee[25], S. Chattopadhyay[2,25], H. Cherif[8,9], P. Chudoba[30], E. Clerkin[31], M. Csanád[32], P. Dahm[9], Supriya Das[25], Susovan Das[3], J. de Cuveland[19], A. Demanov[12], D. Dementiev[28], Zhi Deng[33], H. Deppe[9], I. Deppner[34],

O. Derenovskaya[7], M. Deveaux[9,8], Sheng Dong[35,34], E. Dorenskaya[6], P. Dorosz[16], A.K. Dubey[2], A. Dubla[9], M. Dürr[18], V.V. Elsha[28], D. Emschermann[9], T. Eşanu[11], J. Eschke[31,9], M. Esen[8], Xingming Fan[36,57], O. Fateev[28], C. Feier-Riesen[18], Sheng-Qin Feng[37], F. Fidorra[10], D. Finogeev[38], P. Fischer[39], H. Flemming[9], J. Förtsch[17], P. Foka[9], U. Frankenfeld[9], V. Friese[9], I. Fröhlich[8,9], J. Frühauf[9], T. Galatyuk[40,9], R. Ganai[24], G. Gangopadhyay[24], Xin Gao[9], P. Gasik[31,9], T. Geßler[18], C. Ghosh[2], S.K. Ghosh[25], D. Giang[8], S. Gläßel[8], L. Golinka-Bezshyyko[21], O. Golosov[12], S. Golovnya[41], M. Golubeva[38], D. Golubkov[6], S. Gope[23], S. Gorbunov[9], S. Gorokhov[41],

D. Gottschalk[34], F. Guber[38], M. Gumiński[42], A. Gupta[22], Yu. Gusakov[28], R. Haas[18], Dong Han[33], H. Hartmann[19], Shu He[35], J. Hehner[9], N. Heine[10], N. Herrmann[34,9], J.M. Heuser[9], C. Höhne[18], R. Holzmann[9], Dongdong Hu[43,34], D. Hutter[19], D. Ivanishchev[44], Victor Ivanov[7,12], Vladimir Ivanov[44,12], A. Ivashkin[38], A. Izvestnyy[38], T. Janson[1], A. Jipa[11], I. Kadenko[21], P. Kähler[10], B. Kämpfer[36,57], K.-H. Kampert[17], R. Kapell[9], R. Karabowicz[9], N. Kargin[12], D. Karmanov[15], N. Karpushkin[38], E. Kashirin[12], V.K.S. Kashyap[45], K. Kasiński[16], A. Kazantsev[26], U. Kebschull[1], G. Kekelidze[28], M.M. Khan[5], S. Khan[3], A. Khanzadeev[44,12], F. Khasanov[6], A. Kiryakov[41], M. Kiš[9], I. Kisel[19], S. Kiselev[6], P. Klaus[8], R. Kłeczek[16], Ch. Klein-Bösing[10], V. Klochkov[3], K. Koch[9], L. Koch[18], L. Kochenda[44,12], P. Koczoń[9], M. Kohn[10], R. Kolb[34], A. Kolozhvari[28], B. Komkov[44], M. Korolev[15], I. Korolko[6], M. Koziel[8], G. Kozlov[19,7], V. Kozlov[44], P. Kravtsov[44,12], I. Kres[17], D. Kresan[9], M. Kruszewski[42], A.V. Kryanev[7,12], E. Kryshen[44], W. Kucewicz[16], L. Kudin[44], I. Kudryashov[15], A. Kugler[30], P. Kuhl[9], Ajay Kumar[46], Ajit Kumar[2], L. Kumar[47], S.K. Kundu[48], V. Kyva[49], V. Ladygin[28], E. Lavrik[31], I. Lazanu[11], A. Lebedev[9,7], S. Lebedev[18,7], E. Lebedeva[18], J. Lehnert[9], Chao Li[43], Yuanjing Li[33], V. Lindenstruth[19,9], Feng Liu[35], I. Lobanov[41], E. Lobanova[41], S. Löchner[9], P.-A. Loizeau[31], K. Łojek[27], O. Lubynets[9,8], Xiaofeng Luo[35], A. Lymanets[9], N. Lyublev[6], Jian-Hao Ma[37], S. Mahajan[22], Z. Majka[27], A. Malakhov[28],

D. Malkevich[6], B. Mallick[50], M. Mandal[2], V. Manko[26], O. Maragoto Rodriguez[9,8],A.M. Marin Garcia[9], J. Markert[9], T. Matulewicz[51], S. Mehta[3], M. Merkin[15], A. Meyer-Ahrens[10], J. Michel[8], P. Miedzik[42], K. Mikhailov[6], V. Mikhaylov[30], V. Militsija[49], M.F. Mir[4], D. Miskowiec[9],

B. Mohanty[45], H. Morgenweck[10], T. Morhardt[9], S. Morozov[38], W.F.J. Müller[31], C. Müntz[8], S. Mukherjee[25], P. Munkes[10], Yu. Murin[28], E. Nandy[2], L. Naumann[36], F. Nickels[9], V. Nikulin[44], P. Otfinowski[16], J.H. Otto[18], Liang-ming Pan[52], I. Panasenko[3,49], S. Pandey[46], P. Parfenov[12], S. Parzhitskiy[28], V. Patel[17], C. Pauly[17], V. Petráček[29], M. Petriş[20], M. Petrovici[20], O. Petukhov[38], D. Pfeifer[17], P. Pfistner[13], K. Piasecki[51], J. Pietraszko[9], R. Płaneta[27], V. Plotnikov[6], V. Plujko[21], J. Pluta[53], K. Poźniak[42,51], S.K. Prasad[25], M. Prokudin[6], A. Prozorov[30], M. Pugach[49], V. Pugatch[49], A. Puntke[10], L. Radulescu[20], S. Raha[25], P. Raisig[8], R. Ray[25], A. Redelbach[19], T. Rehman[4], A. Reinefeld[54], A. Reshetin[38], C. Ristea[11], O. Ristea[11], A. Rodriguez Rodriguez[8,9],F. Roether[8], R. Romaniuk[42], A. Rost[31,40], E. Rostchin[44,12], A. Roy[48], S. Roy[25], E. Rubio[34], A. Rustamov[9], Yu. Ryabov[44], R. Sahoo[48], P.K. Sahu[50], S.K. Sahu[50], J. Saini[2], F. Salem[54], S.S. Sambyal[22], C. Schiaua[20], F. Schintke[54], D. Schledt[1], C.J. Schmidt[9], H.R. Schmidt[3,9], P.M. Schneider[10],

F. Seck[40], I. Segal[12], I. Selyuzhenkov[9,12], A. Semennikov[6], A. Sen[25], A. Senger[31], P. Senger[31,8], A.R. Serazetdinov[12], A. Shabanov[38], A. Shabunov[28], N. Sharma[47], A.D. Sheremetiev[28], Shusu Shi[35], S. Shirinkin[6], M. Shiroya[9,8], M. Shitenkow[28], I. Sibiryak[26], V. Sidorenko[13], C. Simon[34], C. Simons[9], A.K. Singh[55], B.K. Singh[46], C.P. Singh[46], O. Singh[5], R. Singh[45], V. Singhal[2], L. Škoda[29], D. Smith[31], Y. Söhngen[34], D. Spicker[8], D. Stach[36], P. Staszel[27], D. Storozhyk[49], J. Stroth[8,9], C. Sturm[9], Yuan Su[43], P. Subramani[17], N. Sukhov[28], R. Sultanov[6], Yongjie Sun[43], Zhengyang Sun[43], D. Svirida[6], R. Szczygieł[16], A. Taranenko[12], O. Tarassenkova[44], M. Teklishyn[9,49], A. Toia[9,8], M. Träger[9], M. Traxler[9], E. Trifonova[13], Yu. Tsyupa[41], N.G. Tuturas[11], F. Uhlig[9], K.L. Unger[13], I. Vassiliev[9], O. Vasylyev[9], R. Visinka[9], E. Volkova[3], A. Vorobiev[41], A. Voronin[15], L. Wahmes[10], Botan Wang[33], Kaiyang Wang[43], Tianxing Wang[43], Xinjian Wang[43], Yi Wang[33], A.A. Weber[18], M. Weber[13], P. Weidenkaff[34], F. Weiglhofer[19], J.P. Wessels[10], D. Wielanek[53], A. Wieloch[27], A. Wilms[9], Gy. Wolf[14], Ke-Jun Wu[37], Qiqi Wu[52], Junfeng Yang[43], Zhongbao Yin[35], In-Kwon Yoo[56], Jianhui Yuan[43], I. Yushmanov[26], W. Zabołotny[42,51], Yu. Zaitsev[6], N.I. Zamiatin[28], H. Zbroszczyk[53], M. Zhalov[44], Qiunan Zhang[34,33], Xiaoming Zhang[35], Yu Zhang[35], Sheng Zheng[37], Daicui Zhou[35], Jian Zhou[43], Wenxiong Zhou[52], Xianglei Zhu[33], A. Zinchenko[28], I. Zivko[6], F. Zorn[18], W. Zubrzycka[16], P. Zumbruch[9]

[1]Institute for Computer Science, Goethe-Universität Frankfurt, Frankfurt, Germany
[2]Variable Energy Cyclotron Centre (VECC), Kolkata, India
[3]Physikalisches Institut, Eberhard Karls Universität Tübingen, Tübingen, Germany
[4]Department of Physics, University of Kashmir, Srinagar, India
[5]Department of Physics, Aligarh Muslim University, Aligarh, India
[6]Institute for Theoretical and Experimental Physics named by A.I. Alikhanov of National Research Centre "Kurchatov Institute" (ITEP) in Moscow, Russia (ITEP), Moscow, Russia
[7]Laboratory of Information Technologies, Joint Institute for Nuclear Research (JINR-LIT), Dubna, Russia
[8]Institut für Kernphysik, Goethe-Universität Frankfurt, Frankfurt, Germany
[9]GSI Helmholtzzentrum für Schwerionenforschung GmbH (GSI), Darmstadt, Germany
[10]Institut für Kernphysik, Westfälische Wilhelms-Universität Münster, Münster, Germany
[11]Atomic and Nuclear Physics Department, University of Bucharest, Bucharest, Romania
[12]National Research Nuclear University MEPhI (Moscow Engineering Physics Institute), Moscow, Russia
[13]Karlsruhe Institute of Technology (KIT), Karlsruhe, Germany
[14]Institute for Particle and Nuclear Physics, Wigner Research Centre for Physics, Hungarian Academy of Sciences, Budapest, Hungary
[15]Skobeltsyn Institute of Nuclear Phyiscs, Lomonosov Moscow State University (SINP-MSU), Moscow, Russia
[16]AGH University of Science and Technology (AGH), Kraków, Poland
[17]Fakultät für Mathematik und Naturwissenschaften, Bergische Universität Wuppertal, Wuppertal, Germany
[18]Justus-Liebig-Universität Gießen, Gießen, Germany
[19]Frankfurt Institute for Advanced Studies, Goethe-Universität Frankfurt (FIAS), Frankfurt, Germany
[20]Horia Hulubei National Institute of Physics and Nuclear Engineering (IFIN-HH), Bucharest, Romania
[21]Department of Nuclear Physics, Taras Shevchenko National University of Kyiv, Kyiv, Ukraine

[22]Department of Physics, University of Jammu, Jammu, India
[23]Nuclear and Radiation Physics Research Laboratory, Department of Physics, Gauhati University, Guwahati, India
[24]Department of Physics and Department of Electronic Science, University of Calcutta, Kolkata, India
[25]Department of Physics, Bose Institute, Kolkata, India
[26]National Research Centre "Kurchatov Institute", Moscow, Russia
[27]Marian Smoluchowski Institute of Physics, Jagiellonian University, Kraków, Poland
[28]Veksler and Baldin Laboratory of High Energy Physics, Joint Institute for Nuclear Research (JINR-VBLHEP), Dubna, Russia
[29]Czech Technical University (CTU), Prague, Czech Republic
[30]Nuclear Physics Institute of the Czech Academy of Sciences, Řež, Czech Republic
[31]Facility for Antiproton and Ion Research in Europe GmbH (FAIR), Darmstadt, Germany
[32]Eötvös Loránd University (ELTE), Budapest, Hungary
[33]Department of Engineering Physics, Tsinghua University, Beijing, China
[34]Physikalisches Institut, Universität Heidelberg, Heidelberg, Germany
[35]College of Physical Science and Technology, Central China Normal University (CCNU), Wuhan, China
[36]Institut für Strahlenphysik, Helmholtz-Zentrum Dresden-Rossendorf (HZDR), Dresden, Germany
[37]College of Science, China Three Gorges University (CTGU), Yichang, China
[38]Institute for Nuclear Research (INR), Moscow, Russia
[39]Institut für Technische Informatik, Universität Heidelberg, Heidelberg, Germany
[40]Institut für Kernphysik, Technische Universität Darmstadt, Darmstadt, Germany
[41]Institute for High Energy Physics (IHEP), Protvino, Russia
[42]Institute of Electronic Systems, Warsaw University of Technology, Warsaw, Poland
[43]Department of Modern Physics, University of Science & Technology of China (USTC), Hefei, China
[44]Petersburg Nuclear Physics Institute named by B.P.Konstantinov of National Research Centre "Kurchatov Institute" (PNPI), Gatchina, Russia
[45]National Institute of Science Education and Research (NISER), Bhubaneswar, India
[46]Department of Physics, Banaras Hindu University (BHU), Varanasi, India
[47]Department of Physics, Panjab University, Chandigarh, India
[48]Indian Institute of Technology Indore, Indore, India
[49]High Energy Physics Department, Kiev Institute for Nuclear Research (KINR), Kyiv, Ukraine
[50]Institute of Physics, Bhubaneswar, India
[51]Faculty of Physics, University of Warsaw, Warsaw, Poland
[52]Chongqing University, Chongqing, China
[53]Faculty of Physics, Warsaw University of Technology, Warsaw, Poland
[54]Konrad-Zuse-Zentrum für Informationstechnik Berlin (ZIB), Berlin, Germany
[55]Indian Institute of Technology Kharagpur, Kharagpur, India
[56]Pusan National University (PNU), Pusan, Korea
[57]also: Technische Universität Dresden, Dresden, Germany

References

[1] S.C. Jeong et al. (FOPI Collaboration). *Phys.Rev.Lett.*, 72:3468, 1994.

[2] M. Petrovici et al. (FOPI Collaboration). *Phys.Rev.Lett.*, 74:5001, 1995.

[3] M.A. Lisa et al. (EOS Collaboration). *Phys.Rev.Lett.*, 75:2662, 1995.

[4] L. Ahle et al. (E866 Collaboration). *Phys.Lett.B*, 490:53, 2000.

[5] S.V. Afanasiev et al. (NA49 Collaboration). *Phys.Rev.C*, 66:054902, 2002.

[6] B. Abelev et al. (ALICE Collaboration). *Phys.Rev.C*, 88:04910, 2013.

[7] L. Kumar et al. (STAR Collaboration). *Nucl.Phys.A*, 904:256c, 2013.

[8] C. Pinkenburg et al. (E895 Collaboration). *Phys.Rev.Lett.*, 83:1295, 1998.

[9] A. Andronic et al. (FOPI Collaboration). *Phys.Lett.B*, 612:173, 2005.

[10] J.C. Bleicher et al. *J.Phys.G*, 325:1859, 1999.

[11] Y. Nara et al. *Eur.Phys.J.*, A50:1, 2018.

[12] M. Petrovici et al. *Phys.Rev.C*, 98:024904, 2018.

[13] S.A. Adamczyk et al. (STAR-Collaaboration). *Phys.Rev.C*, 92:014904, 2015.

[14] M.A. Lisa et al. (E895 Collaboration). *Phys.Rev.Lett.*, 84:2798, 2000.

[15] R.A. Soltz et al. (E866 Collaboration). *Nucl.Phys.A*, 661:439, 1999.

[16] D. Adamova et al. (CERES Collaboration). *Nucl.Phys.A*, 714:124, 2003.

[17] I.G. Bearden et al. (NA44 Collaboration). *Phys.Rev.C*, 58:1656, 1998.

[18] C. Alt et al. (NA49 Collaboration). *Phys.Rev.C*, 77:064908, 2008.

[19] M.M. Aggarwal et al. (WA98 Collaboration). *Phys.Rev.C*, 67:014906, 2003.

[20] K. Amodt et al. (ALICE Collaboration). *Phys.Lett.B*, 696:328, 2011.

[21] M. Petriş et al. High counting rate transition radiation detector . *Nucl. Instr. Meth.*, A581:406–409, 2007.

[22] M. Ciobanu, V. Catanescu, et al. Preamplifier/shaper for ALICE TRD. *IFIN-HH Scientific Report IFIN-HH 2000*, page 64, 2001.

[23] M. Petrovici et al. A high-efficiency Transition Radiation Detector for high-counting-rate environments. *Nucl. Instrum. Meth.*, A579:961–966, 2007.

[24] H.K. Solveit et al. 16 channels ASIC preamplifier-shaper. *GSI Scientific Report 2005-1*, 2005.

[25] M. Petrovici et al. A Two-Dimension Position Sensitive High Efficiency Transition Radiation Detector for High Counting Rate Environment. *Rom. Journ. Phys*, 56:654–663, 2011.

[26] M. Petriş et al. Two-dimensional position sensitive transition radiation detector. *Nucl. Instrum. Meth.*, A714:17–23, 2013.

[27] V. Cătănescu et al. Front End Electronics for High Counting Rate TRD Using a Prototype ASIC. *CBM Progress Report 2009*, page 47, 2010.

[28] G. Caragheorgheopol et al. Front-end electronics for high counting rate TRD. *CBM Progress Report 2010*, page 46, 2011.

[29] M. Petriş et al. TRD detector development for the CBM experiment. *Nucl. Instrum. Meth.*, A732:375–379, 2013.

[30] R. Veenhof. Garfield, recent developments. *Nucl. Instr. Meth. A*, 419:726, 1998.

[31] M. L. Cherry, D. Mueller, and T. A. Prince. The efficient identification of relativistic particles by transition radiation. *Nucl. Instrum. Meth.*, 115:141–150, 1974.

[32] ALICE Collaboration. *ALICE TRD Technical Design Report - ALICE TRD 9*. CERN/LHCC 2001-021, 2001.

[33] W. Blum and L. Rolandi. *Particle Detection with Drift Chambers*. Springer-Verlag, 1994.

[34] A. Bercuci et al. . *to be summited to Nucl. Instrum. Meth. A*, 2016.

[35] A. Bercuci et al. . *to be summited to Nucl. Instrum. Meth. A*, 2016.

[36] CBM Collaboration. CBM Technical Status Report. Technical report, GSI, January 2005.

[37] V. Cătănescu. Specific requirements for analog electronics for a high counting rate TRD. 10th CBM Collaboration Meeting, September 2007.

[38] V. Cătănescu, B. Bartos, and G. Caragheorgheopol. Analog FEE for High Counting Rate Transition Radiation Detector. EuNPC+DPG Conference, Bochum, March 2009.

[39] Europractice. CADENCE. `http://www.europractice.stfc.ac.uk/software/cadence.html`.

[40] R. Veenhof. GARFIELD, recent developments. *Nucl. Instrum. Meth.*, A419:726–730, 1998.

[41] L. Wahmes. private communication, Feb 2021.

[42] L. Wahmes. Planning status of TRD support structure. TRD Retreat, Haus Mariengrund, August 2020.

[43] https://www.microsemi.com/product-directory/fpgas/3854-polarfire-fpgas.

[44] Nadia Rezzak et al. Neutron and proton characterization of microsemi 28 nm polarfire sonos-based fpga. 2018 IEEE Workshop on Radiation Effects Data, https://ieeexplore.ieee.org/stamp/stamp.jsp?tp=&arnumber=8584300, 2018.

[45] Nadia Rezzak et al. https://www.microsemi.com/document-portal/doc_download/1244460-polarfire-neutron-see-test-report, 2018.

[46] https://www.microsemi.com/document-portal/doc_download/1244721-rt-polarfire-radiation-test-report, 2020.

[47] J.Lehnert. https://indico.cern.ch/event/489996/contributions/2211058/attachments/1344419/2026266/, GBTReadout_CBM_TWEPP2016_JLehnert_Final.pdf.

[48] L. Rąduslescu. Towards the engineering design of the 2D position sensitive inner zone for the TRD-TDR addendum. 34^{th} CBM Collaboration Meeting, Bose Institute, Kolkata, India, September 2019.

[49] https://git.cbm.gsi.de/notes/technical/fles-input-interface.

[50] https://www.ti.com/product/ADS52J90.

[51] Hong-Bin Liu, Hu-Cheng Chen, Kai Chen, James Kierstead, Francesco Lanni, Helio Takai, and Ge Jin. Development of an ADC radiation tolerance characterization system for the upgrade of the ATLAS LAr calorimeter. *Chinese Physics C*, 41(2):026101, feb 2017.